Coarsening processes in thin liquid films: Analysis and numerics

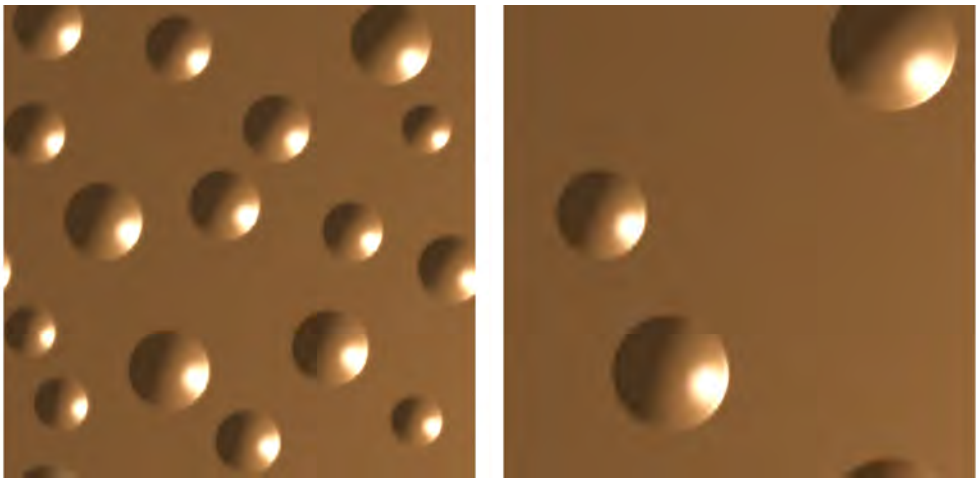

Dissertation
zur
Erlangung des Doktorgrades (Dr. rer. nat.)
der
Mathematisch-Naturwissenschaftlichen Fakultät
der
Rheinischen Friedrich–Wilhelms–Universität Bonn

vorgelegt von
Tobias Rump
aus
Melle

Bonn, Februar 2008

Angefertigt mit Genehmigung der Mathematisch-Naturwissenschaftlichen Fakultät
der Rheinischen Friedrich–Wilhelms–Universität Bonn

Diese Dissertation ist auf dem Hochschulschriftenserver der ULB Bonn
`http://hss.ulb.uni-bonn.de/diss_online` elektronisch publiziert.

Erscheinungsjahr: 2008

1. Gutachter: Prof. Dr. Felix Otto
2. Gutachter: Prof. Dr. Martin Rumpf

Tag der Promotion: 21.05.2008

Danksagung

Mein besonderer Dank gilt Prof. Dr. Felix Otto für die Betreuung und die vielen hilfreichen Tipps beim Anfertigen dieser Arbeit. Desweiteren möchte ich mich bei Prof. Dr. Dejan Slepčev für die langjährige Kooperation bedanken, die im Sommer 2004 bei seinem ersten Besuch in Bonn initiiert wurde. Prof. Dr. Martin Rumpf danke ich für die Übernahme des Zweitgutachtens.

Weiterhin danke ich allen aktuellen und ehemaligen Mitgliedern der Arbeitsgruppe von Prof. Dr. Otto für die mathematischen und nicht-mathematischen Gespräche. Besonders Patrick Penzler konnte durch unzählige Tipps und Computerhilfen zum Gelingen meiner Arbeit beitragen.

Der ehemaligen Arbeitsgruppe von Prof. Dr. Axel Voigt am Forschungsinstitut caesar danke ich für die langjährige Gastfreundschaft und die interessante Zusammenarbeit. Dr. Andreas Rätz hat die Arbeit in Teilen Korrektur gelesen und nützliche Tipps geben können.

Meinen Eltern möchte ich für die Ratschläge und Unterstützung danken. Schließlich danke ich Steffi für die liebevolle Geduld und die Kraft über all die Jahre, sowie Jonathan für sein Dasein.

Contents

1 Introduction and main results

In this thesis, we study the coarsening process and its underlying mechanisms of thin viscous liquid films on solid substrates. The time-evolution of these films is well-described by the so-called *lubrication approximation*, which relies on the assumption that the typical horizontal length scale of the liquid on the substrate is large compared to the typical vertical length scale. In this regime, the evolution of the liquid film is governed by the competition between driving energetics and limiting viscous friction, which is encoded in the *Rayleigh principle*, see Section 1.2. The underlying equation is the *thin-film equation*, a fourth-order parabolic equation for the time-dependent film height $h = h(t,x) > 0$ above the substrate, see Figure 1.1.

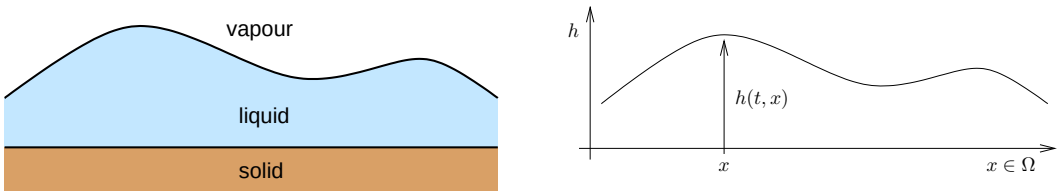

Figure 1.1: A liquid film on a solid substrate defined by the height function h.

Now let us present the mathematical framework for our studies: Let $\Omega \subset \mathbb{R}^d$ ($d = 2$ is physical) be the region of the substrate surface under consideration. In the following, we consider smooth solutions $h : (0,\infty) \times \Omega \to (0,\infty)$ of the thin-film equation in non-dimensionalized form

$$\partial_t h + \nabla \cdot J = 0, \tag{1.1a}$$

$$J = -m(h)\nabla \frac{\delta E}{\delta h}(h). \tag{1.1b}$$

We assume no-flux and equilibrium boundary conditions:

$$\nabla \frac{\delta E}{\delta h}(h) \cdot \nu = \nabla h \cdot \nu = 0 \quad \text{on } (0,\infty) \times \partial\Omega, \tag{1.1c}$$

where ν denotes the outer normal of $\partial\Omega$. Here, the energy functional is defined by

$$E(h) = \int_\Omega \tfrac{1}{2}|\nabla h|^2 + \mathcal{U}(h)\, dx, \tag{1.2}$$

see Section 1.2, and $\frac{\delta E}{\delta h}$ denotes the L^2-gradient of E with respect to h, that is

$$\frac{\delta E}{\delta h}(h) = -\Delta h + \mathcal{U}'(h). \tag{1.3}$$

The boundary conditions (1.1c) ensure that the total mass $\int_\Omega h\,dx$ is conserved and that the total energy $E(h)$ is a Lyapunov functional:

$$\frac{d}{dt}\int h\,dx = 0, \qquad \text{(mass conservation)} \tag{1.4}$$

$$\frac{d}{dt}E(h) = -\int \frac{1}{m(h)}|J|^2\,dx. \qquad \text{(energy dissipation)} \tag{1.5}$$

Note that we will skip the integral subscript Ω if it is clear from the context. In fact, E is much more than just a Lyapunov functional, the dynamics are a gradient flow w.r.t. E, which can be formulated with the help of the Rayleigh principle: At any time, the flux J minimizes

$$\frac{1}{2}\int \frac{1}{m(h)}|J|^2\,dx + \int \nabla\frac{\delta E}{\delta h}(h)\cdot J\,dx. \tag{1.6}$$

Indeed, the Euler–Lagrange equation of (1.6) is just given by (1.1b), and the change of the film height h is defined by the continuity equation (1.1a).

The model features two constitutive functions: $\mathcal{U} = \mathcal{U}(h)$ and $m = m(h)$. We first address the role of $\mathcal{U}$, the so-called *intermolecular potential*. We consider a general class of potentials of the form [4]

$$\mathcal{U}(h) := \tfrac{\sigma_1}{\sigma_2-\sigma_1}h^{-\sigma_2} - \tfrac{\sigma_2}{\sigma_2-\sigma_1}h^{-\sigma_1} + 1 \quad \text{for } 0<\sigma_1<\sigma_2, \tag{1.7}$$

see Figure 1.2 for a typical shape.

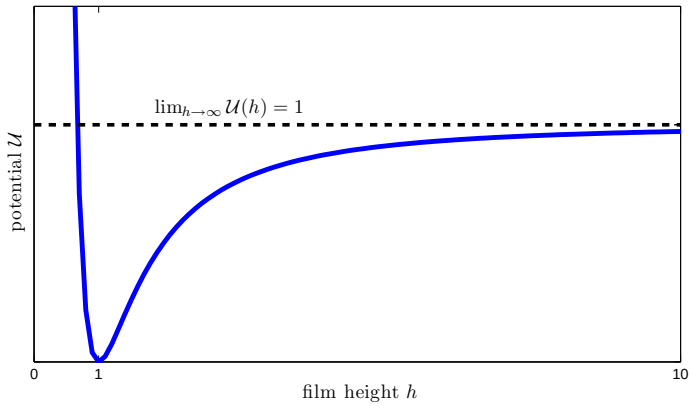

Figure 1.2: A typical shape of the intermolecular potential $\mathcal{U}$ of the form (1.7).

We normalize $\mathcal{U}$ such that

$$\arg\min_h \mathcal{U} = 1 \quad \text{and} \quad \lim_{h\to\infty}\mathcal{U} = 1. \tag{1.8}$$

Loosely speaking, $\mathcal{U}$ allows for two equilibrium heights: $h=1$ (the equilibrium height of the so-called *precursor layer*) and $h=\infty$. Up to translation, there is a unique one-dimensional minimizer of E, which connects these two states, see Figure 1.3. We observe

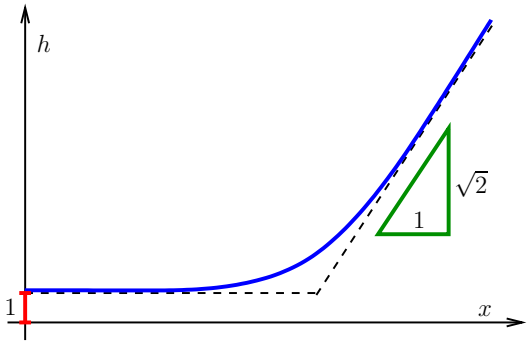

Figure 1.3: The normalization of the potential $\mathcal{U}$ (1.8) sets the asymptotic film height 1 in the precursor layer and the effective contact angle $\sqrt{2}$ of the minimizing profile (in blue).

on the one hand, that the asymptotic film height is equal to $\arg\min_h \mathcal{U} = 1$ as $x \to -\infty$, and on the other hand, that the effective contact angle is set by

$$\lim_{x\to\infty} \partial_x h(x) = \sqrt{2(\lim_{h\to\infty} \mathcal{U}(h) - \min_h \mathcal{U}(h))} = \sqrt{2}. \tag{1.9}$$

Hence, length and height in this model are non-dimensionalized in such a way that both the height of the precursor layer and the contact angle are unity.

Now we consider the other constitutive function, the so-called *mobility function* $m = m(h)$. We restrict our attention to the following parametric form

$$m(h) := h^q, \quad q \geq 0,$$

where we call the parameter q the *mobility exponent*. In particular, this means that we have chosen the time scale in such a way that the mobility is unity in the precursor layer. The appropriate exponent q depends on the underlying rheology, see Section 1.2, in particular, $q = 2$ and $q = 3$ are physical. As we shall see, the exponent q will play a crucial role with a crossover at exactly the physically relevant exponents.

To familiarize ourselves with m, we consider the following Gedankenexperiment, which investigates the energy dissipation rate in a particular scenario, see Figure 1.4: How much dissipation $\int \frac{1}{m}|J|^2\,dx$ costs the translation $\dot{X}$ of the one-dimensional minimizing profile under the constant flux boundary condition $J = J_\infty$ at $x = -\infty$? An elementary integration of the continuity equation $-\dot{X}\partial_x h + \partial_x J = 0$ yields that J is of the form

$$J = \dot{X}\ (h-1) + J_\infty.$$

Therefore, we obtain the dissipation rate on the interval $[0, R]$

$$\begin{aligned}\int_0^R \frac{1}{m}|J|^2\,dx &= (J_\infty)^2 \int_0^R \frac{1}{m}\,dx \\ &+ 2\,\dot{X}J_\infty \int_0^R \frac{1}{m}(h-1)\,dx + (\dot{X})^2 \int_0^R \frac{1}{m}(h-1)^2\,dx, \end{aligned} \tag{1.10}$$

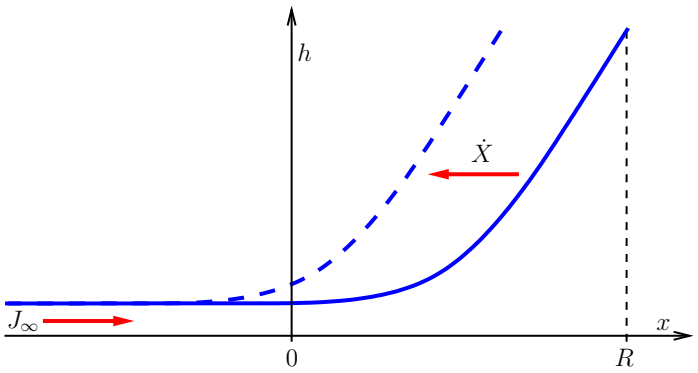

Figure 1.4: The translation $\dot{X}$ of the minimizing profile subject to the flux boundary condition J_∞.

where we think of $R \gg 1$. In the last two integrals in (1.10), we observe the following crucial crossovers in the leading order contribution to the dissipation:

- In $\int_0^R \frac{1}{m}(h-1)\,dx$, the leading order contribution comes
  - for $q \le 2$ from $x \sim R$ where $h \sim R$, and
  - for $q > 2$ from the transition region between the linear and the constant profile $h \approx 1$.
- In $\int_0^R \frac{1}{m}(h-1)^2\,dx$, the leading order contribution comes
  - for $q \le 3$ from $h \sim R$, and
  - for $q > 3$ from the transition region.

In view of mass conservation (1.4), it is relevant to investigate minimizers of the energy E given the (excess) volume. According to (1.3), these are characterized by

$$P := \frac{\delta E}{\delta h}(h) = -\Delta h + \mathcal{U}'(h) = \text{const},$$

where the pressure $P > 0$ plays the role of a Lagrange multiplier. For any excess volume $V = \int (h - h_\infty)\,dx \gg 1$, where $h_\infty \approx 1$ denotes the asymptotic height of the profile as $|x| \to \infty$, there exists a (up to translation) unique minimizer, called the *equilibrium droplet profile*, which is radially symmetric, see Figure 1.5. The profile is parabolic and the effective contact angle is $\sqrt{2}$. This implies that the excess volume V, the droplet radius R, and its energy E are related by

$$V \sim R^{d+1} \quad \text{and} \quad E \sim R^d. \tag{1.11}$$

For our further studies, we are interested in the evolution of liquid films of average height

$$\overline{H} := \fint_\Omega h\,dx > \arg\min \mathcal{U}(h) = 1.$$

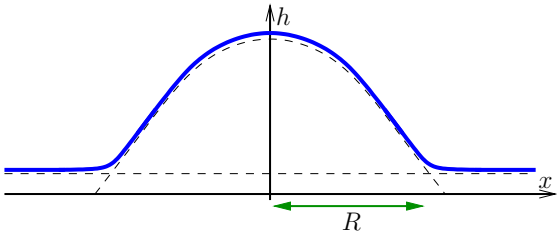

Figure 1.5: Equilibrium droplet profile (in blue), a minimizer of E given the volume.

The competition between attractive and repulsive forces encoded in the special form (1.7) of the intermolecular potential $\mathcal{U}$ stabilizes a liquid layer of height ≈ 1 according to the normalization of $\mathcal{U}$ in (1.8). The "excess" liquid accumulates on top of the precursor layer in a configuration of near-equilibrium droplets, whose typical volume is given by $V \sim L^d\overline{H}$. Here, L denotes the typical distance between the droplets. Figure 1.6 shows a configuration of such droplets sitting on a precursor layer in the two-dimensional case.

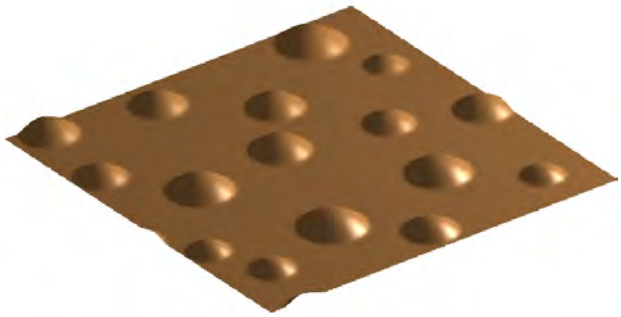

Figure 1.6: A typical configuration of well-defined equilibrium droplets connected by a uniform precursor layer on a periodic domain.

The scaling relations (1.11) suggest that the energy E of a droplet as a function of the volume V is concave:

$$E \sim V^{\frac{d}{d+1}},$$

since $\frac{d}{d+1} < 1$. Consequently, with respect to energetics, it is more favorable to distribute the excess mass into fewer droplets. Hence, driven by the reduction of the total energy, such droplet configurations change in time; the dynamics is only limited by the dissipation (1.5). We call this process *coarsening*, since the number of droplets decreases while the typical distance L increases over time. Figure 1.7 shows a coarsening sequence in the two-dimensional case.

However, it is a-priori not clear by which detailed mechanisms this energy-driven coarsening process is realized.

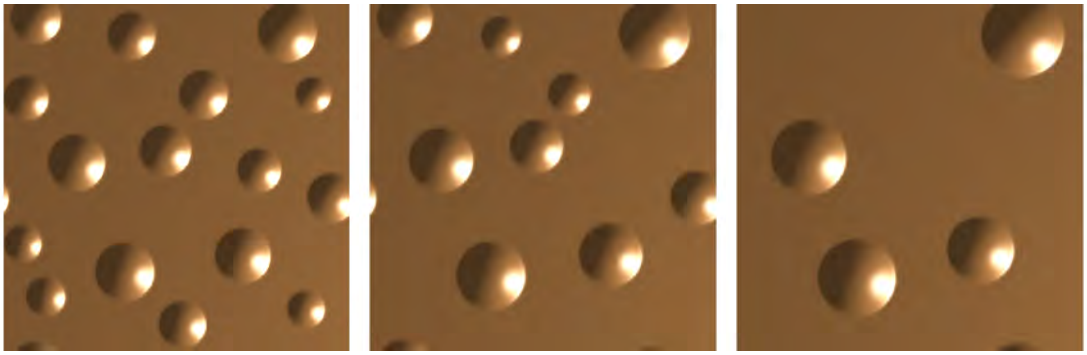

Figure 1.7: A coarsening sequence of a droplet configuration on a periodic domain.

1.1 Main results

Dynamics of droplets: Competing coarsening mechanisms

In detail, the coarsening process of a droplet configuration can be mediated by two competing mechanisms: *collapse* of small droplets, which relies on the mass exchange between droplets through the precursor layer, and *collision* of at least two migrating droplets, see Figure 1.8. However, it is not clear whether collapse or collision of inter-

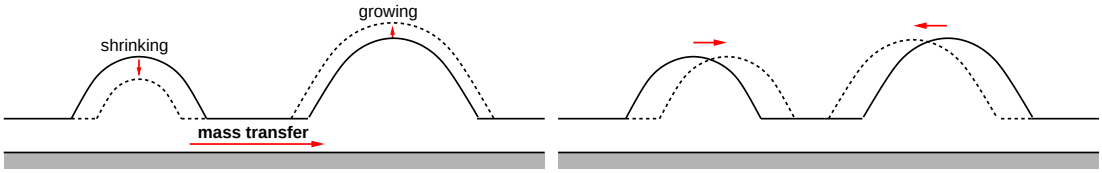

Figure 1.8: Coarsening mechanisms: Collapse (left) due to mass transfer and collision (right) of migrating droplets.

acting droplets is the dominant coarsening mechanism. We study the competition in the one- and two-dimensional case and find that the relative importance of collision depends both on the mobility exponent q and the average film height $\overline{H}$. In the following, we will present our main results and motivate them based on formal arguments.

As a first step to understand the droplet interaction, we study the two individual mechanisms separately.

Ostwald ripening: To investigate mass transfer, we consider for the sake of simplicity a mass-conserving configuration of two immobile equilibrium droplets of different sizes $V_i \sim R_i^{d+1}$ and centers of mass X_i, $i = 1, 2$. If the droplet distance $L = |X_1 - X_2|$ is large compared to the radii R_i, most of the dissipation will take place in the precursor layer, where the mobility m is unity. Given the rate of volume changes $\dot{V}_1 = -\dot{V}_2$, the flux J

adjusts itself as to minimize the dissipation rate $\int |J|^2\,dx$ subject to $\dot V_1\delta_{X_1}+\dot V_2\delta_{X_2}+\nabla\cdot J=0$. Accordingly, $J=-\nabla\psi$ with $\psi(x)=\dot V_1 G(x-X_1)+\dot V_2 G(x-X_2)$ and G as the d-dimensional fundamental solution.

Now we see that the case $d=2$ is critical: For $d=1$, the flux J is constant between the droplets, so that

$$\int |J|^2\,dx\sim L(\dot V_1^2+\dot V_2^2),$$

whereas for $d\geq 3$, most of the dissipation takes place in the neighborhood of the droplets, so that

$$\int |J|^2\,dx\ \sim\ R_1^{2-d}\dot V_1^2+R_2^{2-d}\dot V_2^2\ \sim\ V_1^{\frac{2-d}{d+1}}\dot V_1^2+V_2^{\frac{2-d}{d+1}}\dot V_2^2.$$

For $d=2$, we have a logarithmic divergence:

$$\int |J|^2\,dx\sim \log(L/V_1^{\frac13})\dot V_1^2+\log(L/V_2^{\frac13})\dot V_2^2.$$

Furthermore, the energy change scales as

$$\dot E\sim V_1^{-\frac{1}{d+1}}\dot V_1+V_2^{-\frac{1}{d+1}}\dot V_2.$$

Thus, the Rayleigh principle (1.6), or, more precisely, the minimization of (1.5) in $\dot V_1=-\dot V_2$ yields that

$$\dot V_1=-\mathfrak{rip}(L,V_i)\left(V_1^{-\frac{1}{d+1}}-V_2^{-\frac{1}{d+1}}\right),\tag{1.12}$$

where the *ripening factor* $\mathfrak{rip}(L,V_i)$ scales as

$$\mathfrak{rip}(L,V_i)\sim\begin{cases}L^{-1} & \text{for } d=1,\\ \left(\log(L/V_1^{\frac13})+\log(L/V_2^{\frac13})\right)^{-1} & \text{for } d=2,\\ \left(V_1^{\frac{2-d}{d+1}}+V_2^{\frac{2-d}{d+1}}\right)^{-1} & \text{for } d\geq 3.\end{cases}$$

In particular, the larger droplet grows at the expense of the smaller one. This effect is a particularity of Ostwald ripening.

Migration: To study migration, we consider a single equilibrium droplet in an ambient constant flux field $J_\infty\in\mathbb{R}^d$, which points from west to east, see Figure 1.9. It is intuitive that the droplet moves in the direction opposite to the flux, that is to the west: From the point of view of dissipation, it is more favorable to deposit mass at the western side of the droplet and to take it away from the eastern side than to transport it across the droplet. By this process, the droplet retains its equilibrium shape while moving westwards. Qualitatively, this effect is independent of the mobility exponent $q\geq 0$.

Again, we utilize the Rayleigh principle to show that the droplet velocity $\dot X$ is determined by

$$\dot X=-\mathfrak{mig}(R)\,J_\infty.\tag{1.13}$$

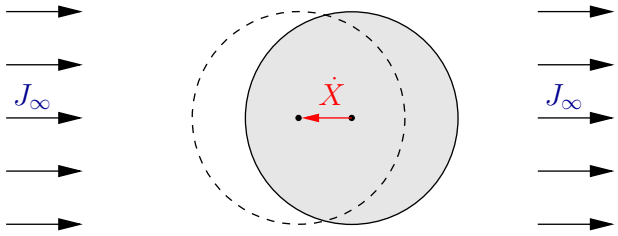

Figure 1.9: The equilibrium droplet migrates in the opposite direction to J_∞.

Our asymptotic analysis in the regime of large droplets, i.e. $R \gg 1$, reveals the scaling of the *migration factor* $\mathfrak{mig}(R)$, which depends on the mobility exponent, but is (at least in terms of scaling) independent of the dimension:

$$\mathfrak{mig}(R) \sim \begin{cases} R^{-1} & \text{for } q \in [0,2), \\ (\log R)\, R^{-1} & \text{for } q = 2, \\ R^{q-3} & \text{for } q \in (2,3), \\ (\log R)^{-1} & \text{for } q = 3, \\ 1 & \text{for } q > 3, \end{cases}$$

to leading order in R.

The scaling $\mathfrak{mig}(R) \sim R^{-1}$, which holds for $q < 2$, is easy to interpret: In a small time interval δt, the amount of mass deposited at the western foot region (which has size $\sim R^{d-1}$) scales as $\delta t\, |J_\infty|\, R^{d-1}$; the same amount is taken away from the eastern side. By this, the center of mass X of the droplet moves westwards by $\delta X \sim \delta t\, |J_\infty|\, R^{-1}$, so that it is natural that the new center of the equilibrium droplet moves westwards by the same amount. Loosely speaking, the mass deposited at the western foot moves up the droplet flank, see Figure 1.10. At the eastern flank, the same amount of mass moves

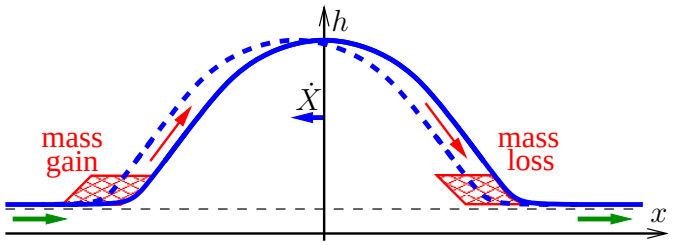

Figure 1.10: The response $\dot{X}$ of the droplet on the flux J_∞ (in green) for mobility exponent $q < 2$. The deposited mass (in red) moves up the western flank.

down to compensate the mass loss at the foot.

However, it is not immediately clear why the droplet migrates much faster for larger q. Of course, the droplets become more mobile with increasing q. It seems as if for $q > 3$, the mass deposited at the western foot does not move up the flank, but that the droplet cap

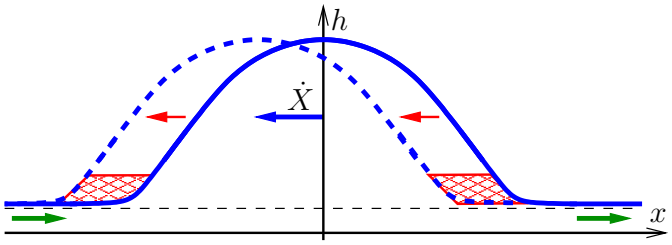

Figure 1.11: The response $\dot{X}$ on the flux J_∞ for mobility exponent $q > 3$. The droplet cap slides on the mass deposited at the western foot.

instead slides westwards to cover the deposited mass, see Figure 1.11. The real reason for this behavior becomes apparent when reconsidering our Gedankenexperiment above, see Figure 1.4. Here, R and $\dot{X}$ play the role of the droplet radius and speed, respectively, and we look at the western flank of the droplet. By the Rayleigh principle, the optimal speed $\dot{X}$ of the droplet should be determined by minimizing (1.10) for given J_∞. As we already pointed out, for $q < 2$, both integrals $\int \frac{1}{m}(h-1)\,dx$ and $\int \frac{1}{m}(h-1)^2\,dx$ are dominated by the contribution of the droplet cap, i.e. $h \sim R$, and thus, their ratio scales as R^{-1}. For $q > 3$, both integrals are dominated by the foot region, i.e. $h \approx 1$. Thus, their ratio is of order 1 in R.

In this thesis, we carry out detailed asymptotic analysis which reveals the dynamics of both mechanisms separately. In particular, we recover the volume change (1.12) and the droplet velocity (1.13) together with the leading order scaling relations of the ripening and the migration factor.

Droplet interaction: Collision vs. collapse

As we found in the paragraph about Ostwald ripening above, mass exchange between droplets gives rise to a flux field J. In the precursor, J is the gradient of a harmonic function: $J = -\nabla\psi$. In an annular region around a given droplet centered at X, it makes sense to speak of the linear part of ψ (in the sense of a Laurent expansion). This linear part, or more precisely, its constant gradient plays the role of the flux J_∞ in the discussion of migration (see above). Hence, it is this linear part, which determines the migration speed $\dot{X}$ of the droplet. In conclusion, the droplet migration is slaved to mass exchange, i.e. the Ostwald ripening.

A configuration of two droplets will not lead to collision: Consider two droplets with volumes $V_1 < V_2$ and centers of mass X_1 and X_2, respectively, see Figure 1.12 (left). Then the minimizing flux J is a gradient: $J = -\nabla\psi$, where ψ has the form of the harmonic function $\dot{V}_1 G(x - X_1) + \dot{V}_2 G(x - X_2)$, see 1.12 (right) for a cross-section. The constant part of $-\nabla\psi$ in an annular region around a droplet is parallel to $X_2 - X_1$ due to the symmetry of the problem. Furthermore, it holds for both droplets that this constant part has positive slope in the direction of $X_2 - X_1$. Since $\dot{V}_1 = -\dot{V}_2$, it even holds that the constant parts are equal. Thus, according to the considerations above, both

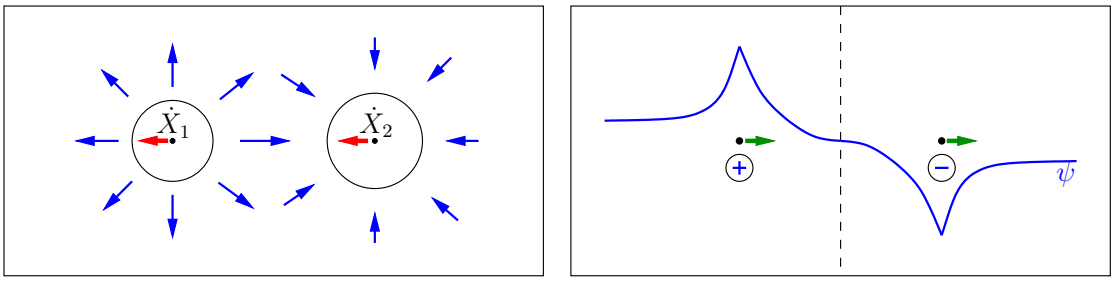

Figure 1.12: Left: Two isolated droplets of different size generate a flux field J (in blue), which transports mass from the smaller droplet to the larger one. Right: The flux J is the gradient of a harmonic function ψ (in blue). For both droplets, the constant part of $-\nabla\psi$ in an annular region of the droplet (playing the role of J_∞) points eastwards (in green), and therefore gives rise to migration to the west.

droplet move westwards in the direction of the smaller droplet. As the scaling of the migration factor reveals (see above), the smaller droplet moves faster than the larger one. Therefore, collision cannot happen in a two-droplet configuration. By this, we obtain a different result than Pismen and Pomeau in [33] in the following sense: They claim that both droplets migrate in the direction of the larger droplet, that is eastwards in our picture. Furthermore, they argue (in accordance with our findings) that the smaller droplet moves faster, so that it might catch up with the larger one leading to collision. In contrast, numerical tests confirm our findings.

However, in many-droplet configurations, there is a bias towards collision of small droplets: Consider two relatively small droplets submerged into a configuration of larger droplets. We find that both droplets loose mass to the surrounding droplets, see Figure 1.13 (left). Furthermore, the specific form of ψ, see Figure 1.13 (right), yields constant

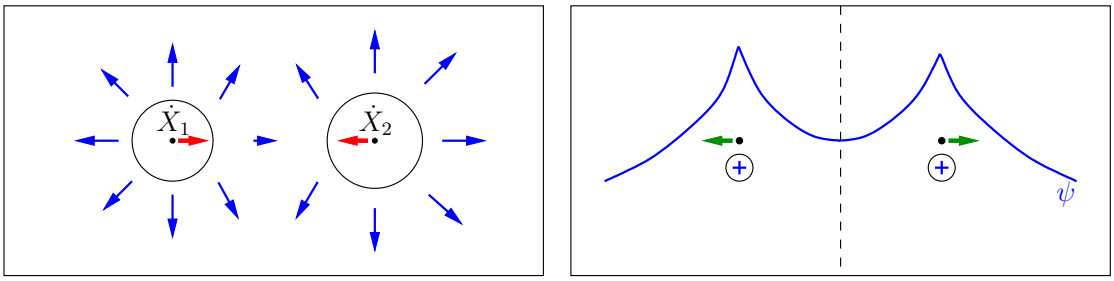

Figure 1.13: Left: Two smaller droplets submerged into a configuration of larger droplets. They both loose mass to the surrounding droplets. Right: The constant part of $-\nabla\psi$ points westwards in the neighborhood of the western droplet, and eastwards in the neighborhood of the eastern droplet. Therefore, the droplets move towards each other.

parts of $-\nabla\psi$, which on the one hand, points westwards in the neighborhood of the western droplet, and on the other hand, points eastwards in the neighborhood of the

eastern droplet. Here, we again invoke the symmetry of the problem. Accordingly, the droplets move toward each other, which eventually leads to collision, provided no droplet vanishes.

We finally address the question whether collapse or collision is the dominating coarsening mechanism. We focus on the two-dimensional case. For this purpose, we consider a (statistically homogeneous) arrangement of droplets of size of the order R, and thus of average distance $L \sim (\overline{H}^{-1}V)^{\frac{1}{2}}$. In view of (1.12), the typical time τ_{rip} it takes for a droplet to collapse is

$$\tau_{\mathrm{rip}} \sim \frac{V}{\dot{V}} \sim (\log V) V^{\frac{4}{3}}.$$

In view of (1.13), the typical time τ_{mig} it takes for a droplet to collide with another droplet is

$$\tau_{\mathrm{mig}} \sim\sim \frac{L}{\dot{L}} \sim \frac{L}{|\dot{X}|} \sim \mathfrak{mig}(R)^{-1}\overline{H}^{-1} (\log V) V^{\frac{4}{3}}.$$

Hence, we can identify the relative importance of migration in terms of scaling:

$$\frac{\tau_{\mathrm{mig}}}{\tau_{\mathrm{rip}}} \sim \overline{H}^{-1} \begin{cases} R & \text{for } q \in [0,2), \\ (\log R)^{-1} R & \text{for } q = 2, \\ R^{3-q} & \text{for } q \in (2,3), \\ \log R & \text{for } q = 3, \\ 1 & \text{for } q > 3. \end{cases}$$

For $q < 3$, we find that collapse is eventually the dominant mechanism, since the average size R of a droplet increases during coarsening. However, for $q \geq 3$, the average film height $\overline{H}$ sets the relative importance of collision for all times (up to a logarithm for $q = 3$). In particular, we expect a collision-dominated coarsening scenario for configurations with large average height.

In this thesis, we study the detailed interaction in many-droplet configurations by means of the Rayleigh principle. For this purpose, we reduce the configuration space of all possible film heights to an finite-dimensional ensemble of equilibrium droplets (defined by the set of volumes $\{V_i\}$ and centers $\{X_i\}$). It allows us to describe the droplet interaction asymptotically in the regime of large, well-separated droplets, i.e. $1 \ll R \ll L$, as a mass-conserving system of ODEs, which determines the energy descent:

$$G(\{V_i\},\{X_i\}) \begin{pmatrix} \{\dot{V}_i\} \\ \{\dot{X}_i\} \end{pmatrix} = -\nabla E(\{V_i\}).$$

Here, the matrix G encodes the limiting dissipation of both mechanisms and their coupling. In particular, we recover the detailed droplet interaction and the typical time scales of both individual mechanisms as presented above.

To convince ourselves of the validity of our asymptotic results, we conduct several numerical simulations for both the thin-film equation and the reduced system of ODEs.

Thereby, we consider a two-droplet configuration in two dimensions for the physically relevant case $q = 2$. Here, a challenge for the numerical validation of the reduced model is the restrictive underlying regime $1 \ll R \ll L$ and the bounded domain on which we solve the thin-film equation; a straightforward comparison of both results looks unsatisfactory. However, further refinements of the approximations allow us to present a conclusive numerical comparison between the full thin-film equation and a refined reduced system of ODEs. In particular, we remove the huge impact of the bounded domain on the accuracy of the reduced dynamics by adjusting the ambient fluxes that generate droplet migration. At the end, we obtain convincing results with deviations smaller than 10%.

Rigorous upper bounds on coarsening

In sufficiently large systems, the coarsening process seems to be statistically self-similar as confirmed by heuristic arguments and numerical simulations. The "coarseness" of the configuration at time t is typically measured in terms of the distance $L(t)$. Then the rate of coarsening is characterized by a power-law, e.g.

$$L(t) \sim t^{\beta},$$

where β is the *coarsening exponent*.

For a rigorous treatment, Kohn and Otto [19] proposed a method of proving a lower bound on the energy decay rate. The method relies on two inequalities, which are on the formal level the following:

- *Dissipation inequality:*
$$(\dot{L})^2 \lesssim -\dot{E}, \tag{1.14}$$
- *Interpolation inequality:*
$$E\,L^{\alpha} \;\sim\; 1. \tag{1.15}$$

By this, we heuristically obtain

$$(\dot{L})^2 \overset{(1.15)}{\sim} (\dot{E})^2\, E^{-\frac{2}{\alpha}-2},$$

and therefore, by integration of (1.14) we deduce a lower bound on the energy:

$$E(t) \gtrsim t^{-\frac{\alpha}{\alpha+2}}.$$

The abstract framework of this robust method uses the fact that the evolution (1.1) can be formally interpreted as a gradient flow on the Riemannian manifold of all possible film heights with respect to the energy (1.2).

The rigorous analysis requires the definition of the length scale L, which provides a way to express the distance between two droplet configurations h_0 and h_1. It is natural to take the distance on the manifold, which is induced by the metric of the gradient

flow structure. For mobility exponent $q = 1$, the distance is explicitly known to be the so-called *quadratic Wasserstein distance*:

$$\mathcal{W}(h_0, h_1) \;:=\; \left(\inf\left\{\iint |x-y|^2 d\pi(x,y) \;\Big|\; \int d\pi(\cdot, y) = h_0,\, \int d\pi(x,\cdot) = h_1\right\}\right)^{\frac{1}{2}},$$

which measures the quadratic costs of density-preserving transports.

Now, let us formulate our main result, which gives a rigorous bound on the decay of the energy density in a time-averaged sense for the mobility exponent $q = 1$. In particular, the proof reveals that $\alpha = \frac{d}{d+1}$, which leads to the dimension-dependent bound on the energy decay defined by the exponent $-\frac{d}{3d+2}$.

Theorem. *Let the potential $\mathcal{U}$ satisfy*

$$\begin{aligned} \mathcal{U} &\geq 0 \quad \text{on } (0,\infty), \\ \mathcal{U} &\geq 1 \quad \text{on } (2,\infty). \end{aligned}$$

Let h be a smooth solution of (1.1) for $q = 1$ on a large domain $\Omega := [0,\Lambda]^d$, $\Lambda \gg 1$, which has the same total volume as a constant layer of thickness 3:

$$\int_\Omega h\, dx \;=\; \int_\Omega h^*\, dx, \quad h^* \equiv 3.$$

Then for $\sigma \in (1, \frac{3d+2}{d})$,

$$\int_0^T \Big(\Lambda^{-d} E(h(t))\Big)^\sigma \, dt \quad \gtrsim \quad \int_0^T (t^{-\frac{d}{3d+2}})^\sigma \, dt,$$

provided $T \gg \Big(\Lambda^{-\frac{d}{2}} \mathcal{W}(h^*, h(0))\Big)^{\frac{3d+2}{d+1}}$ and $\Lambda^{-d} E(h(0)) \ll 1$.

Our main contribution is the rigorous proof of the interpolation inequality (1.15) involving the Wasserstein distance.

Finally, the lower bound on the energy heuristically yields an upper bound on the coarsening rate:

$$L(t) \overset{(1.15)}{\sim} E(t)^{-\frac{d+1}{d}} \lesssim t^{\frac{d+1}{3d+2}}.$$

We conduct numerical tests based on the thin-film equation in one and two dimensions and obtain results, which are in agreement with the rigorous bounds.

1.2 Modeling background

In this section, we will briefly review the derivation of the thin-film equation (1.1) from the Navier-Stokes equation. Basic ingredient is the Rayleigh principle, which provides an important tool for our further studies.

We consider thin films of an incompressible Newtonian liquid with viscosity μ on a solid substrate, see Figure 1.1. The substrate is defined by

$$\left\{(x,z) \in \mathbb{R}^{d+1} \;\middle|\; x \in \Omega \subset \mathbb{R}^d \text{ and } z < 0\right\}.$$

Note that we use the notation $x \in \mathbb{R}^d$ for the horizontal and $z \in \mathbb{R}$ for the vertical coordinate. The liquid-vapor interface is a free (time-evolving) boundary assumed to be given by a graph $h = h(t,x)$, $x \in \Omega$, see Figure 1.1. The mathematical description of the flow of the liquid is provided by the incompressible Navier–Stokes equation:

$$\begin{aligned} \partial_t \vec{u} + D\vec{u}\,\vec{u} &= \nabla \cdot T, \\ \nabla \cdot \vec{u} &= 0, \end{aligned}$$

for the time-dependent velocity field $\vec{u}(t,x,z) = (\vec{v}(t,x,z), w(t,x,z))$, where $\vec{v}$ denotes the horizontal and w the vertical component, together with suitable boundary conditions. Note that in this case the spatial derivatives are taken w.r.t. the variables x and z. Here,

- the incompressibility is guaranteed by $\nabla \cdot \vec{u} = 0$, and
- the stress tensor T is the sum of inner friction and the isotropic pressure p:

  $$T = \mu(D\vec{u} + D\vec{u}^T) - p\,\mathbb{I}\mathrm{d},$$

  with $\mathbb{I}\mathrm{d}$ as the identity map.

The crucial boundary condition is imposed for the horizontal component $\vec{v}$ at the solid-liquid interface ($z = 0$): A classical choice would be the so-called no-slip boundary condition

$$\vec{v}\big|_{z=0} = 0. \tag{1.16}$$

One way to relax this condition is to introduce finite-slippage models by the slip condition

$$\vec{v}\big|_{z=0} = \frac{\beta^{3-q}}{h^{2-q}}\,\partial_z \vec{v}\big|_{z=0}, \quad q \in (0,3). \tag{1.17}$$

The parameter $\beta > 0$ is the so-called slip length. Here, the choice of $q \in (0,3)$ depends on the underlying rheology. In particular, the case $q = 1$ is known as the Greenspan-slip condition [17], and the case $q = 2$ as the Navier-slip condition, see e.g. [8].

1.2.1 Lubrication approximation

The lubrication approximation, introduced by Reynolds 1886 in [36], is based on the assumption that the typical height H_0 of the liquid film is small compared to the typical horizontal length scale L_0 of the film:

$$\varepsilon := \frac{H_0}{L_0} \ll 1.$$

In this approximation, the liquid film and its evolution are described by

- the time-dependent film height $h = h(t,x)$, $(t,x) \in [0,\infty) \times \Omega$, which represents the liquid-vapor interface as explained above, and
- the vertical average $u = u(t,x)$ of the horizontal component $\vec{v}$ of the velocity field $\vec{u}$:

$$u(t,x) = \frac{1}{h} \int_0^h \vec{v}(t,x,z)\, dz.$$

The incompressibility of the liquid immediately implies the coupling between h and u via the continuity equation

$$\partial_t h + \nabla \cdot (hu) = 0. \tag{1.18}$$

Then to leading order in ε, the Navier–Stokes equation implies that the pressure is constant in the vertical direction, i.e. $p = p(t,x)$, and that its horizontal gradient balances the viscous stress:

$$\nabla p = \mu\, \partial_z^2 \vec{v}.$$

An elementary integration w.r.t. the vertical component z yields that $\vec{v}$ has the form of a Poiseuille flow:

$$\vec{v} = 3\left(1 + 3\left(\frac{\beta}{h}\right)^{3-q}\right)^{-1} \left(\left(\frac{\beta}{h}\right)^{3-q} + \frac{z}{h} - \frac{1}{2}\left(\frac{z}{h}\right)^2\right) u \tag{1.19}$$

described by the average velocity u. Here, we involve the slip condition (1.17) and the continuity of the stress tensor at the liquid-vapor interface, i.e. $\partial_z \vec{v}\big|_{z=h} = 0$, as boundary conditions for the integration.

1.2.2 Energy dissipation: The Rayleigh principle

The average velocity u is determined by the *Rayleigh principle*: For thin films, the viscous friction coming from the boundary conditions (1.16) or (1.17), respectively, has a huge impact on the evolution of the film, as it limits the energy driven dynamics. Consequently, the velocity u balances the rate of the energy loss with the rate of dissipation by friction.

In our model, the energy of the liquid film is a combination of surface energy and an intermolecular potential $\mathcal{U}$:

$$E(h) = \int \tfrac{1}{2}\gamma |\nabla h|^2 + \mathcal{U}(h)\, dx, \tag{1.20}$$

where γ denotes the surface tension of the liquid-vapor interface [9]. The first term is derived from the expansion of the surface element $\sqrt{1+|\nabla h|^2}$ for small slopes $|\nabla h| \sim \varepsilon$. The second term, i.e. the intermolecular potential of the form (1.7), models the attractive (van der Waals) and repulsive (Born-type) forces between the solid-liquid and the liquid-vapor interface [11].

An easy calculation shows that the change of energy is

$$\frac{d}{dt}E(h(t,x)) = \int \frac{\delta E}{\delta h}\,\partial_t h\,dx \overset{(1.18)}{=} \int h\nabla\frac{\delta E}{\delta h}\cdot u\,dx =: \dot{E}(h).u\,. \tag{1.21}$$

Now we turn to the dissipation rate. In the lubrication approximation, the viscous dissipation rate [22] is given by

$$D(\vec{u}) = \mu\left(\int_0^h\int_\Omega |\partial_z\vec{v}|^2\,dx\,dz + \int_\Omega \frac{h^{2-q}}{\beta^{3-q}}|\vec{v}(x,0)|^2\,dx\right), \quad q\in(0,3). \tag{1.22}$$

According to the special form of $\vec{v}$ in (1.19), the dissipation can be expressed as a quadratic form in the vertical average u:

$$D(u) := 3\mu\int\frac{1}{h}\left(1+3\left(\tfrac{\beta}{h}\right)^{3-q}\right)^{-1}|u|^2\,dx, \quad q\in(0,3). \tag{1.23}$$

Now we can formulate the Rayleigh principle, which determines u:

At any time, u minimizes the Rayleigh functional

$$\mathcal{R}(u) \;:=\; \tfrac{1}{2}D(u) + \dot{E}(h).u\,. \tag{1.24}$$

This principle is also called Onsager–Rayleigh principle, see [26] and references therein.

We see from (1.21) and (1.23) that $\dot{E}$ is a linear form and D is a quadratic form in u. It immediately follows from the variational principle that the minimizing u fulfills the Euler–Lagrange equation of (1.24), which reveals the balance between limiting viscous forces and driving energy loss:

$$3\mu\,\frac{1}{h}\left(1+3\left(\tfrac{\beta}{h}\right)^{3-q}\right)^{-1} u \;+\; h\nabla\frac{\delta E}{\delta h}(h) \;=\; 0, \qquad q\in(0,3).$$

The minimizing average velocity determined by the balance equation

$$u = -\frac{1}{3\mu}h^2\left(1+3\left(\tfrac{\beta}{h}\right)^{3-q}\right)\nabla\frac{\delta E}{\delta h}(h), \qquad q\in(0,3),$$

is coupled to the change of the film height through the continuity equation (1.18). Thus, we finally obtain

$$3\mu\,\partial_t h - \nabla\cdot\left(h^3\left(1+3\left(\tfrac{\beta}{h}\right)^{3-q}\right)\nabla\frac{\delta E}{\delta h}(h)\right) = 0, \qquad q\in(0,3).$$

In particular, the mobility function m depends on the underlying fluid model: For large slip lengths $\beta \gg h$, the mobility factor in front of the flux scales to leading order like

h^q, whereas for a small slip length $\beta \ll h$, we obtain the "standard" mobility function h^3 as derived from no-slip boundary conditions (1.16).

For the mathematical treatment, we will consider a non-dimensionalized form of this equation together with no-flux and equilibrium boundary conditions, as stated in (1.1). We will even generalize the range of mobility exponents as we allow for all $q \geq 0$. In this general case, the associated dissipation rate in non-dimensionalized form is given by

$$D(u) = \int \frac{1}{h^q}\, h^2\, |u|^2\, dx, \qquad q \geq 0, \tag{1.25}$$

and the energy as stated in (1.2), to which we will refer in the following.

1.3 Outline

In **Chapter 2**, we analyze the profile of an equilibrium droplet, which minimizes the energy under the constraint of fixed volume, by means of asymptotic analysis. Furthermore, we introduce a coarse-grained mesoscopic energy and its minimizers; it provides a needful reduction for our further studies.

A rigorous bound on the energy decay is given in **Chapter 3**. The method, which essentially relies on a dissipation inequality and an interpolation inequality, is introduced in an abstract framework based on the gradient flow structure of the problem. The main contribution is the proof of an interpolation inequality, which characterizes the geometry of the energy landscape. Finally, heuristic arguments relate the lower bound on the energy to an upper bound on the coarsening rate. The results of this chapter have been published in *SIAM Journal on Mathematical Analysis* [28].

In **Chapter 4**, we study the two coarsening mechanisms, i.e. collapse and collision, by means of two model problems, which treat Ostwald ripening and migration separately. The results allow us on the one hand to deduce basic qualitative features of these mechanisms (e.g. the sign of the droplet velocity), and on the other hand to give leading order scaling relations based on asymptotic analysis, which will finally quantify the relative importance of both mechanisms to the coarsening process.

To infer the relative importance of collision and collapse, we analyze in **Chapter 5** the detailed interaction of droplets in the framework of a reduced configuration space of mesoscopic droplets. Basic tool is the Rayleigh principle, which sets the reduced dynamics. We finally deduce heuristically typical time scales for both mechanisms, which reveal the impact of each on the coarsening process. The results of the preceding two chapters have been published in an SFB preprint, which is accepted for publication in *European Journal of Applied Mathematics* [29].

Concluding, we conduct several numerical experiments in **Chapter 6** to validate the analytical results of the previous chapters. For this purpose, we introduce discretizations of both the full thin-film equation and the reduced dynamics for many-droplet configurations. Furthermore, we refine the approximations in the reduced dynamics to obtain better results in comparison with the thin-film equation. Our symmetric discretization idea for the thin-film equation (or, more precisely, for Cahn–Hilliard-type equations) has been published in the proceeding *Multiscale Modeling in Epitaxial Growth* [27].

For the convenience of the reader, a complete list of frequently used symbols and notation is given in the Appendix.

2 Equilibrium droplets

In this chapter, we will analyze the equilibrium droplet profile in detail by means of asymptotic analysis.

An equilibrium droplet profile $\widetilde{h}$ is a stationary point of the energy (1.2) subject to the constraint of fixed volume $\int \widetilde{h}\ dx = V$, $V > 0$. Hence according to (1.3), the droplet profile has constant pressure $P > 0$:

$$P = \frac{\delta E}{\delta h}(\widetilde{h}) = -\Delta \widetilde{h} + \mathcal{U}'(\widetilde{h}). \tag{2.1}$$

In the following, we will asymptotically describe a family of radially symmetric equilibrium droplets (parametrized by P) in two dimensions on an infinite domain. The asymptotic regime of interest is $0 < P \ll 1$, which (as the analysis reveals) corresponds to the regime of large droplets. Mathematically speaking, we seek solutions of

$$-\partial_r^2 \widetilde{h} - r^{-1}\partial_r \widetilde{h} + \mathcal{U}'(\widetilde{h}) = P, \tag{2.2a}$$

$$\partial_r \widetilde{h}(0) = 0 \quad \text{and} \quad \lim_{r\uparrow\infty} \widetilde{h}(r) = h_\infty, \tag{2.2b}$$

in the asymptotic regime $0 < P \ll 1$. Note that we will use the same notation for $\widetilde{h}(x)$ and $\widetilde{h}(r)$ for convenience. The compatibility condition $\mathcal{U}'(h_\infty) = P$ necessarily holds.

First we prove a monotonicity property:

Proposition 1 (Monotonicity of an equilibrium droplet profile)**.** *An equilibrium droplet profile characterized through* (2.2) *has the following properties:*

$$\left\{ \begin{array}{ll} \widetilde{h}(r) > h_\infty, & r \in [0,\infty), \\ \partial_r \widetilde{h}(r) < 0, & r \in (0,\infty). \end{array} \right\} \tag{2.3}$$

Proof. First let us state that $h_\infty \approx 1$ in the regime of interest. Indeed, a Taylor expansion of $\mathcal{U}'(h_\infty)$ around 1 yields

$$h_\infty - 1 \approx \mathcal{U}''(1)^{-1}\ P \ll 1. \tag{2.4}$$

Thus in particular,

$$\mathcal{U}''(h_\infty) \approx \mathcal{U}''(1) > 0. \tag{2.5}$$

For further investigations, we reformulate (2.2a) as

$$\partial_r^2 \widetilde{h} + r^{-1}\partial_r \widetilde{h} + \mathcal{V}'(\widetilde{h}) = 0, \tag{2.6}$$

where $\mathcal{V}(h) := -\mathcal{U}(h) + Ph$. It is helpful to consider $\widetilde{h}$ as describing the position of a particle at time r moving in the landscape defined by the potential $\mathcal{V}$.

Due to the definition of $\mathcal{U}$ and (2.5), the potential $\mathcal{V}$ has the following properties:

- h_∞ is the only local maximum of $\mathcal{V}$.
- $\lim_{\widetilde{h}\downarrow 0} \mathcal{V} = -\infty$ and $\lim_{\widetilde{h}\uparrow\infty} \mathcal{V} = +\infty$.

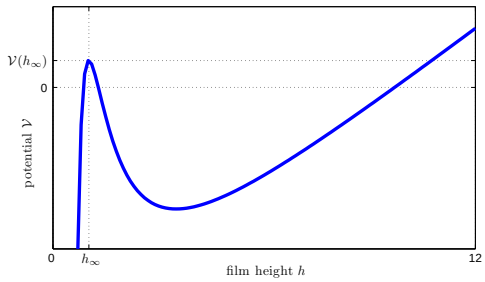

We utilize the energy $\frac{1}{2}(\partial_r\widetilde{h})^2 + \mathcal{V}(\widetilde{h})$: According to (2.6), the energy decreases:

$$\partial_r \left[\tfrac{1}{2}(\partial_r\widetilde{h})^2 + \mathcal{V}(\widetilde{h})\right] = -r^{-1}(\partial_r\widetilde{h})^2 \leq 0$$

for $r \in [0,\infty)$. Then we obtain that once the particle is at rest, i.e. $\partial_r\widetilde{h}(r_*) = 0$ for some $r_* \in [0,\infty)$, it is trapped below the value $\mathcal{V}(\widetilde{h}(r_*))$. Indeed,

$$\mathcal{V}(\widetilde{h}(r)) \leq \tfrac{1}{2}(\partial_r\widetilde{h}(r))^2 + \mathcal{V}(\widetilde{h}(r)) \leq \tfrac{1}{2}(\partial_r\widetilde{h}(r_*))^2 + \mathcal{V}(\widetilde{h}(r_*)) = \mathcal{V}(\widetilde{h}(r_*)) \tag{2.7}$$

for $r > r_*$. Note that even $\mathcal{V}(\widetilde{h}(r)) < \mathcal{V}(\widetilde{h}(r_*))$ as long as $r_* \neq 0$. In particular, the particle initially moves downhill (meaning $\partial_r\widetilde{h} < 0$ where $\mathcal{V}'(\widetilde{h}) > 0$, or $\partial_r\widetilde{h} > 0$ where $\mathcal{V}'(\widetilde{h}) < 0$, respectively) or (at least) rests.

Furthermore, the particle never stops while moving downhill: Assume that $\partial_r\widetilde{h}(r_1) < 0$ and $\mathcal{V}'(\widetilde{h}(r_1)) > 0$ for some $r_1 > 0$. Then we deduce from integrating $-\partial_r(r\partial_r\widetilde{h}) = r\,\mathcal{V}'(\widetilde{h})$ on $[r_1, r_2]$, where we choose the interval such that $\mathcal{V}'$ has the unique sign $+1$, that

$$r_1\partial_r\widetilde{h}(r_1) - r_2\partial_r\widetilde{h}(r_2) = \int_{r_1}^{r_2} r\,\mathcal{V}'(\widetilde{h}(r))\,dr > 0. \tag{2.8}$$

Hence, in particular $\partial_r\widetilde{h}(r_2) < \partial_r\widetilde{h}(r_1) < 0$. (Vice versa, the assumptions $\partial_r\widetilde{h}(r_1) > 0$ and $\mathcal{V}'(\widetilde{h}(r_1)) < 0$ analogously yield $\partial_r\widetilde{h}(r_2) > \partial_r\widetilde{h}(r_1) > 0$.)

Now it is easy to deduce the asserted monotonicity properties: Due to the form of $\mathcal{V}$, there exists $h_1 > h_\infty$ such that $\mathcal{V}(\widetilde{h}) > \mathcal{V}(h_\infty)$ for all $\widetilde{h} > h_1$. We follow from (2.7) that the initial position is necessarily larger than h_1: $\widetilde{h}(0) \geq h_1$. Otherwise, it would never reach h_∞. Furthermore, for any $r > 0$, $\widetilde{h}$ is never below h_∞, since then, it would be driven down the potential in contradiction to its asymptotic behavior $\widetilde{h} \to h_\infty$. This proves the first item.

Starting from $\widetilde{h}(0) \geq h_1$, the particle moves downhill. Assume now that it moves non-monotonically, that is, there exists $r > 0$ such that $\partial_r\widetilde{h}(r) = 0$. This can only happen uphill according to (2.8). But then, according to (2.7), it would be again trapped in contradiction to the asymptotic behavior. This concludes the proof. □

2.1 Asymptotic analysis of equilibrium droplets

The matched asymptotic description of solutions of (2.2) in the regime $P \ll 1$ consists of three regions:

1. *Cap region:* This outer region starting from $r = 0$ is characterized by $\widetilde{h} \gg 1$ and $\mathcal{U}'(\widetilde{h}) \ll P$ (as hinted by the previous inspection). Approximately, the profile in this region has parabolic shape.

2. *Foot region:* The approximation in the cap region is no longer valid as $\widetilde{h}$ reaches 1, where $\mathcal{U}'$ attains its maximum larger than P, see Figure 2.1 (bottom). In this interior region, the Laplacian $-\partial_r^2\widetilde{h} - r^{-1}\partial_r\widetilde{h}$ is relatively large in order to balance $\mathcal{U}'(\widetilde{h})$. This layer connects the two outer regions.

3. *Precursor region:* The precursor region is characterized by a profile $\widetilde{h}$, which converges to $h_\infty \approx 1$ exponentially fast with a small slope, and, consequently, by $\mathcal{U}'(\widetilde{h})$ tending to P.

Figure 2.1 (top) shows a cross-section of a typical equilibrium droplet profile with $P \approx 0.1$ on a two-dimensional substrate.

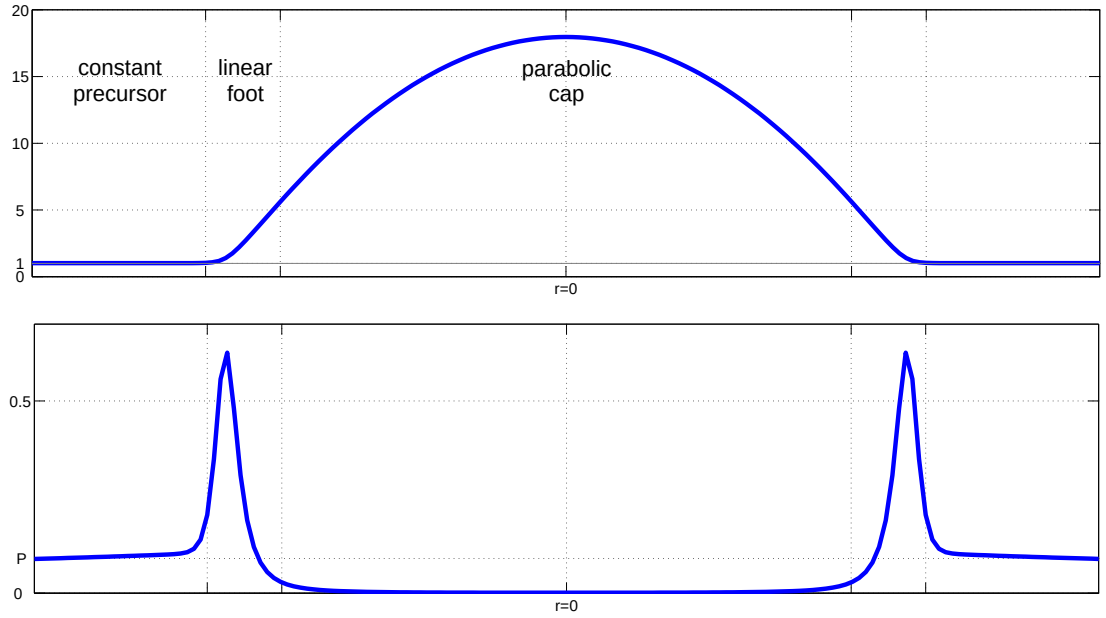

Figure 2.1: Cross-section of an equilibrium droplet profile (top) and the pressure contribution $\mathcal{U}'(\widetilde{h})$ (bottom) for $P \approx 0.1$.

Now let us present the matched asymptotics in detail. To fix ideas, we define $R > 0$ by

$$\widetilde{h}(r = R) = 2$$

as the *radius* of the equilibrium droplet. Such a radius R exists and is unique, since $\widetilde{h}$ is strictly monotone. It indicates the foot region and will be determined by matching in terms of the asymptotic parameter P.

Precursor region

The precursor region is defined by $r \geq R$. Then the profile is determined by the simplified equation

$$-\partial_r^2 \widetilde{h}(r) + \mathcal{U}'(\widetilde{h}) = P(= \mathcal{U}'(h_\infty)) \quad \text{for } r \geq R. \tag{2.9}$$

Later we will show that the omittance of the term $r^{-1}\partial_r \widetilde{h}$ is to leading order consistent.

Lemma 1 (Exponential convergence of the profile in the precursor region)**.** *It holds to leading order that*

$$\log\left(\widetilde{h}(r) - h_\infty\right) = \sqrt{\mathcal{U}''(1)}(R - r) \tag{2.10}$$

in the regime $r - R \gg 1$.

Proof. Equation (2.9) implies

$$\partial_r \left[-\tfrac{1}{2}(\partial_r \widetilde{h}(r))^2 + \mathcal{U}(\widetilde{h}) - (\mathcal{U}(h_\infty) + \mathcal{U}'(h_\infty)(\widetilde{h} - h_\infty))\right] = 0.$$

Including the boundary conditions (2.2b), we obtain by integration

$$-\tfrac{1}{2}(\partial_r \widetilde{h}(r))^2 + \widetilde{\mathcal{U}}(\widetilde{h}) = 0 \quad \text{for } r \geq R, \tag{2.11}$$

where

$$\widetilde{\mathcal{U}}(\widetilde{h}) := \mathcal{U}(\widetilde{h}) - (\mathcal{U}(h_\infty) + \mathcal{U}'(h_\infty)(\widetilde{h} - h_\infty)) \tag{2.12}$$

is to leading order the quadratic error term in $\widetilde{h} - h_\infty$ in the Taylor expansion of $\mathcal{U}$. Integration of the resulting identity

$$\partial_r \widetilde{h} = -\sqrt{2\widetilde{\mathcal{U}}(\widetilde{h})}$$

on the interval $[R, r]$ yields

$$\int_R^r \frac{\partial_r \widetilde{h}(r)}{\sqrt{2\widetilde{\mathcal{U}}(\widetilde{h})}}\, dr = R - r.$$

The monotonicity property (2.3) admits a transform of variables of the following form:

$$\int_{\widetilde{h}(R)=2}^{\widetilde{h}(r)} \frac{1}{\sqrt{2\widetilde{\mathcal{U}}(\widetilde{h})}}\, d\widetilde{h} = R - r. \tag{2.13}$$

As stated above, $\widetilde{\mathcal{U}}$ is to leading order quadratic in $\widetilde{h} - h_\infty$:

$$\widetilde{\mathcal{U}}(\widetilde{h}) \approx \tfrac{1}{2}\mathcal{U}''(1)(\widetilde{h} - h_\infty)^2. \tag{2.14}$$

Hence, the integral in (2.13) diverges logarithmically as $\widetilde{h} \to h_\infty$, that is to leading order

$$\log\left(\widetilde{h}(r) - h_\infty\right) = \sqrt{\mathcal{U}''(1)}(R-r) \qquad \text{for } r - R \gg 1.$$

This finishes the proof. □

Finally, let us argue why the term $r^{-1}\partial_r \widetilde{h}$ can be omitted in the approximation, or equivalently, why $r^{-1}\partial_r \widetilde{h}$ is small compared to $\mathcal{U}'(\widetilde{h}) - \mathcal{U}'(h_\infty)$. According to (2.11), this follows from

$$\frac{1}{r}\sqrt{2\widetilde{\mathcal{U}}(\widetilde{h})} \le \frac{1}{R}\sqrt{2\widetilde{\mathcal{U}}(\widetilde{h})} \ll \widetilde{\mathcal{U}}'(\widetilde{h}) \quad \text{for } h_\infty \le \widetilde{h} \le 2.$$

Due to (2.14) both terms scale the same for $\widetilde{h} \approx h_\infty$. Hence, $R \gg 1$ is sufficient for this inequality to hold. As we will see later, the assumption $P \ll 1$ indeed implies $R \gg 1$.

Foot region

It is convenient to choose the rescaling

$$\frac{r}{R} = \exp\left(\frac{s}{R}\right), \qquad s \in \mathbb{R}. \tag{2.15}$$

Then the regime $\left|\frac{s}{R}\right| \ll 1$ corresponds to the foot region. Equation (2.2a) simplifies to

$$-\partial_s^2 \widetilde{h}(s) + \exp\left(2\tfrac{s}{R}\right)\left(\mathcal{U}'(\widetilde{h}) - \mathcal{U}'(h_\infty)\right) = 0 \quad \text{for } s \in \mathbb{R},$$

and hence, we obtain in the regime $\left|\frac{s}{R}\right| \ll 1$

$$-\partial_s^2 \widetilde{h}(s) + \mathcal{U}'(\widetilde{h}) - \mathcal{U}'(h_\infty) = 0 \quad \text{for } s \in \mathbb{R}. \tag{2.16}$$

Lemma 2 (Linear profile in the foot region)**.** *It holds to leading order that*

$$\widetilde{h}(r) = \sqrt{2}(R-r) \tag{2.17}$$

in the regime $1 \ll R - r \ll \min\{R, P^{-1}\}$.

Proof. As before, we integrate (2.16) and obtain

$$-\tfrac{1}{2}(\partial_s \widetilde{h}(s))^2 + \widetilde{\mathcal{U}}(\widetilde{h}) = c \quad \text{for } \left|\tfrac{s}{R}\right| \ll 1$$

for some constant c, or, in original variables,

$$-\tfrac{1}{2}(\tfrac{r}{R}\partial_r \widetilde{h}(r))^2 + \widetilde{\mathcal{U}}(\widetilde{h}) = c \quad \text{for } \left|\tfrac{r}{R} - 1\right| \ll 1.$$

Finally, to leading order in $\frac{r}{R}$ it holds

$$-\tfrac{1}{2}(\partial_r \widetilde{h}(r))^2 + \widetilde{\mathcal{U}}(\widetilde{h}) = c \quad \text{for } \left|\tfrac{r}{R} - 1\right| \ll 1. \tag{2.18}$$

The constant c is determined by matching with the precursor (described by $r \geq R$) in an overlap region with the foot: This overlap region is determined by

$$0 < r - R \ll R,$$

since $\left|\frac{r}{R} - 1\right| \ll 1$ in particular implies $r - R \ll R$. By matching $\widetilde{h}$ and its derivative in (2.11) and (2.18), we conclude that $c = 0$.

In turn, we obtain

$$\int_2^{\widetilde{h}(r)} \frac{1}{\sqrt{2\widetilde{\mathcal{U}}(\widetilde{h})}}\, d\widetilde{h} = R - r \quad \text{for } \left|\tfrac{r}{R} - 1\right| \ll 1.$$

The potential $\widetilde{\mathcal{U}}$ can be to leading order approximated by 1 in a certain regime:

$$\widetilde{\mathcal{U}}(\widetilde{h}) = \mathcal{U}(\widetilde{h}) - (\mathcal{U}(h_\infty) + \mathcal{U}'(h_\infty)(\widetilde{h} - h_\infty)) \approx 1 \quad \text{for } 1 \ll \widetilde{h} \ll P^{-1}.$$

Indeed, on the one hand, $\mathcal{U}$ is normalized such that $\mathcal{U}(h) \approx 1$ as $h \gg 1$. On the other hand, $\mathcal{U}(h_\infty) \approx 0$ and $\mathcal{U}'(h_\infty) \approx 0$, respectively, since $h_\infty - 1 \ll 1$. Furthermore, the product $\mathcal{U}'(h_\infty)\widetilde{h}$ is small if and only if $\widetilde{h} \ll \mathcal{U}'(h_\infty)^{-1} = P^{-1}$. Hence, in this regime, it holds

$$\widetilde{h}(r) = \sqrt{2}(R - r)$$

to leading order in $R - r$, which proves the assertion. The regime $1 \ll \widetilde{h} \ll P^{-1}$ together with $\left|\frac{r}{R} - 1\right| \ll 1$ translates into $1 \ll R - r \ll \min\{R, P^{-1}\}$. □

Cap region

We define the cap region by

$$\widetilde{h} \gg 1 \quad \text{and} \quad \mathcal{U}'(\widetilde{h}) \ll P, \tag{2.19}$$

so that (2.2a) simplifies to

$$-\partial_r^2 \widetilde{h} - r^{-1}\partial_r \widetilde{h} = P. \tag{2.20}$$

Note that the regime (2.19) translates into

$$\widetilde{h} \gg P^{-\frac{1}{\sigma_1 + 1}}, \quad \sigma_1 > 0, \tag{2.21}$$

according to the special form of $\mathcal{U}$ in (1.7), which implies a non-trivial overlap region with the foot region.

Lemma 3 (Parabolic profile in the cap region)**.** *It holds to leading order that*

$$\widetilde{h}(r) = \frac{R}{\sqrt{2}}\left(1 - \left(\frac{r}{R}\right)^2\right) \tag{2.22}$$

in the regime $R - r \gg P^{-\frac{1}{\sigma_1 + 1}}$.

Proof. Including the left boundary condition in (2.2b), a solution of (2.20) is given by

$$\widetilde{h}(r) = -\frac{P}{4}r^2 + \widetilde{h}(r=0).$$

The constants P and $\widetilde{h}(r=0)$ are determined in terms of R by matching the function and the derivative with the foot region: According to (2.21), the overlap region is characterized through

$$P^{-\frac{1}{\sigma_1+1}} \ll \widetilde{h} \ll P^{-1},$$

which is non-trivial since $\sigma_1 > 0$. Hence, matching function and derivative with (2.17) leads to

$$-\frac{P}{2}R = -\sqrt{2} \quad \text{and} \quad \widetilde{h}(r=0) - \frac{P}{4}R^2 = 0,$$

and consequently

$$P = \frac{2\sqrt{2}}{R} \quad \text{and} \quad \widetilde{h}(r=0) = \frac{R}{\sqrt{2}}. \tag{2.23}$$

Thus, the cap profile is to leading order given by

$$\widetilde{h}(r) = \frac{R}{\sqrt{2}}\left(1 - \left(\frac{r}{R}\right)^2\right).$$

Since $\widetilde{h}$ is linear in the overlap region, the regime translates into $R - r \gg P^{-\frac{1}{\sigma_1+1}}$. □

Let us summarize the results from the matched asymptotic analysis to leading order:

- The precursor profile is constant:

$$\widetilde{h}(r) = 1 \quad \text{for } r - R \gg 1. \tag{2.24a}$$

- The radius of the droplet profile (identified by the connecting interior layer) is given by

$$R = 2\sqrt{2}\, P^{-1}. \tag{2.24b}$$

  Note that this relation translates the scaling assumption $P \ll 1$ into $R \gg 1$.

- The cap profile is parabolic:

$$\widetilde{h}(r) = \frac{R}{\sqrt{2}}\left(1 - \left(\frac{r}{R}\right)^2\right) \quad \text{for } R - r \gg 1. \tag{2.24c}$$

These results are in accordance with the results of minimizing a coarsened, so-called *mesoscopic* energy, which is presented in the subsequent section.

2.2 Mesoscopic droplets

A *mesoscopic droplet profile* on a precursor of constant height $+1$ is a minimizer of the mesoscopic energy

$$\overline{E}(h) := \int \tfrac{1}{2}|\nabla h|^2 + \chi_{\{h>1\}}\, dx, \tag{2.25}$$

subject to the constraint of fixed volume. The mesoscopic energy $\overline{E}$ supplies a "coarse-grained" view on the intermolecular potential, which suppresses the details of the transition from $\min \mathcal{U} = 0$ to $\lim_{h\to\infty} \mathcal{U} = 1$, see Figure 2.2.

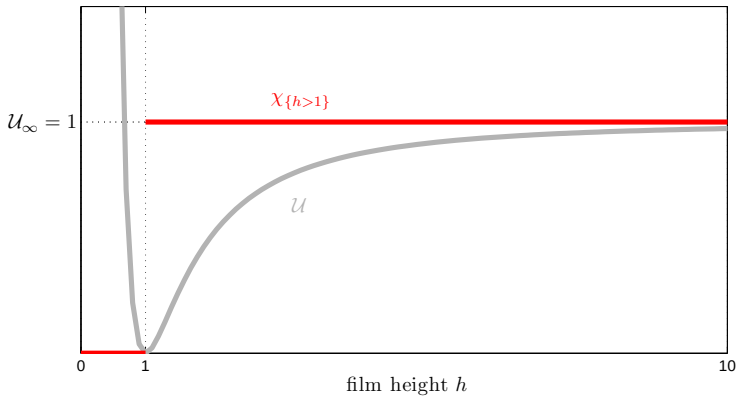

Figure 2.2: Mesoscopic intermolecular potential $\chi_{\{h>1\}}$ (in red).

Since the uniform precursor does not contribute to the energy, we shift h by -1 and consider the following minimization problem: We seek minimizers of

$$\int \tfrac{1}{2}|\nabla h|^2\, dx + \operatorname{vol}(\{h > 0\}) \tag{2.26}$$

under all $h > 0$ with fixed volume $V > 0$, that is $\int h(x)\, dx = V$. We denote the shifted minimizer by $\underline{h}$.

Proposition 2 (Mesoscopic droplet profile)**.** *There exists $H > 0$ such that*

$$\underline{h}(x) = -\frac{1}{2H}|x|^2 + H \quad \text{on } B_{\sqrt{2}H}(0) \tag{2.27}$$

is the (up to translation) unique minimizer of (2.26)*, where $B_{\sqrt{2}H}(0)$ denotes the ball with center 0 and radius $\sqrt{2}H$. The height H depends on the volume V and the dimension d:*

$$H = \left(\frac{d+2}{2\sqrt{2}\,\omega_d}\right)^{\frac{1}{d+1}} V^{\frac{1}{d+1}}, \tag{2.28}$$

where ω_d denotes the volume of the d-dimensional unit sphere. The mesoscopic contact angle at $\partial B_{\sqrt{2}H}(0)$ is independent of the droplet size:

$$|\nabla \underline{h}(x)| = \sqrt{2} \quad \text{for } x \in \partial B_{\sqrt{2}H}(0). \tag{2.29}$$

We will not present the proof in full detail and instead refer to the Appendix in [28], but let us give a brief review. Basically, the proof is done in three steps, in which we prove the following statements:

1. A minimizer of (2.26) is radially symmetric (w.l.o.g. with respect to the origin), that is $\underline{h}(x) = \underline{h}(|x|)$, and monotone decreasing in $|x|$.

   The proof of this statement relies on the symmetric rearrangement of functions, see e.g. [23].

2. A minimizer $\underline{h}$ satisfies
$$-\Delta \underline{h} = 0 \quad \text{on } \{\underline{h} > 0\}. \tag{2.30}$$

3. There exists a (up to translations) unique minimizer $\underline{h}$ with
$$\tfrac{1}{2}|\nabla \underline{h}(x)|^2 = 1 \quad \text{on } \partial\{\underline{h} > 0\}. \tag{2.31}$$

   This assertion is proven by volume-preserving homothetic variations.

Equation (2.28) follows from elementary integration.

By shifting $\underline{h}$ back and using the relation $R = \sqrt{2}H$, we obtain the so-called *mesoscopic droplet profile* parametrized by its center X and its volume V (or, equivalently, its radius R):
$$h(x) = 1 + h_{V,X}(x),$$
where we define
$$\begin{aligned} h_{V,X}(x) &= \max\left\{0, -\tfrac{1}{\sqrt{2}\omega} V^{-\frac{1}{d+1}} |x-X|^2 + \tfrac{\omega}{\sqrt{2}} V^{\frac{1}{d+1}}\right\} && \text{(2.32a)} \\ &= \max\left\{0, -\tfrac{1}{\sqrt{2}} R^{-1} |x-X|^2 + \tfrac{1}{\sqrt{2}} R\right\}. && \text{(2.32b)} \end{aligned}$$
Here, we set
$$\omega := \begin{cases} \left(\frac{3}{2\sqrt{2}}\right)^{\frac{1}{2}} & \text{for } d = 1, \\ \sqrt{2}\pi^{-\frac{1}{3}} & \text{for } d = 2, \end{cases} \tag{2.33}$$
such that $R = \omega V^{\frac{1}{d+1}}$. It immediately implies that the constant pressure of a mesoscopic droplet is related to R and V by
$$P = \frac{2d}{\sqrt{2}} R^{-1} = \frac{2d}{\sqrt{2}\,\omega} V^{-\frac{1}{d+1}}. \tag{2.34}$$
The form of $h_{V,X}$ and P are in accordance with the asymptotic results of the preceeding section.

Corollary 1 (Energy of a mesoscopic droplet)**.** *In terms of the radius R and the volume V, the mesoscopic energy* (2.25) *of a single mesoscopic droplet is given by*
$$\begin{aligned} \overline{E} &= \tfrac{\sqrt{2}(d+1)}{\omega^{d+1}} R^d && \text{(2.35a)} \\ &= \tfrac{\sqrt{2}(d+1)}{\omega} V^{\frac{d}{d+1}}. && \text{(2.35b)} \end{aligned}$$

3 Rigorous upper bounds on coarsening rates in a droplet model

In this chapter, we will study the coarsening behavior of liquid films consisting of well-defined droplets, whose evolution is given by the thin-film equation (1.1). We will restrict to the case of mobility exponent $q = 1$. Based on an abstract framework established by Kohn and Otto in [19], we will rigorously prove a lower bound on the energy decay rate in a time-averaged sense. The rigorous lower bound on the energy can be heuristically related to an upper bound on the coarsening rate.

The results presented in this chapter have been published in *SIAM Journal on Mathematical Analysis* [28].

3.1 Abstract framework: The Kohn–Otto method

The framework of proving lower bounds on the energy decay was introduced by Kohn and Otto in [19] for the Cahn–Hilliard equation with constant and degenerate mobilities. It relies on the fact that the evolution can be (formally) interpreted as a gradient flow on a Riemannian manifold. Main ingredients for the proof are two estimates:

- an estimate that restricts the rate of change of the distance between a gradient flow trajectory and a reference configuration by the rate of the energy change. We call this estimate *dissipation inequality*. On the formal level, this inequality follows immediately from the gradient flow structure, provided the distance is the natural one induced by the metric.

- an estimate on the geometry of the energy landscape that bounds the energy as a function of the distance from below. We call this estimate *interpolation inequality*. The bound is characterized by a *geometric* exponent α. Our main analytical contribution is the proof of such an inequality involving the Wasserstein distance as the natural distance.

An ODE argument relates the geometric exponent α with the *dynamical* exponent γ, which bounds the energy as a function of time from below by

$$E(t) \gtrsim t^{-\gamma} \tag{3.1}$$

in a time-averaged sense, see Theorem 3. Heuristically, this lower bound on the energy yields an *upper* bound on the coarsening rate, see Section 3.6.

A universal statement for *lower* bounds on the coarsening rate cannot be true, since there are solutions of the thin-film equation that do not coarsen at all, for example the unstable periodic configuration of equilibrium droplets. Hence, a lower bound can only hold in some generic cases – a statement for all trajectories in the gradient flow cannot hold.

Further applications of the method proposed in [19] can be found in the literature. In [5], coarsening in off-critical mixtures within the Mullins-Sekerka evolution is studied. The authors of [6] and [7] investigate the coarsening behavior in mean-field models of phase transitions and of a phase-field model, which deals with both temperature and phase fields. In [20] and [21], rigorous bounds on coarsening rates are proven for an epitaxial growth model and for models of multicomponent phase separation. Recently, the coarsening in a discrete, ill-posed non-linear diffusion equation was analyzed in this framework [12].

In the physics literature, only few experimental studies of coarsening processes in thin liquid films can be found. The only long-time results we are aware of are studies of coarsening processes for polymer fluids [24, 25].

In the remainder of this section, we introduce the abstract framework of Kohn and Otto based on the formal gradient flow structure.

3.1.1 Formal gradient flow structure

On a formal level, a gradient flow with trajectory $t \mapsto x(t)$ on a manifold $\mathcal{M}$ w.r.t. a functional $E : \mathcal{M} \to \mathbb{R}$ is defined by

$$\dot{x} = -\nabla E(x). \tag{3.2}$$

To identify the tangential vector $\nabla E(x)$ with the co-tangent vector $\operatorname{diff} E_x$, one needs a metric tensor g on the tangent space $T_x\mathcal{M}$ defined in each $x \in \mathcal{M}$:

$$g_x(\nabla E(x), v) = \operatorname{diff} E_x.v \quad \forall v \in T_x\mathcal{M}.$$

The right hand side denotes the differential of E in x in the direction of v. Then the trajectory of the gradient flow (3.2) is determined by

$$g_{x(t)}(\dot{x}(t), v) + \operatorname{diff} E_{x(t)}.v = 0 \quad \forall v \in T_{x(t)}\mathcal{M}. \tag{3.3}$$

The metric tensor g induces a distance $d : \mathcal{M} \times \mathcal{M} \to \mathbb{R}_+$ between two points on the manifold: For $x_0, x_1 \in \mathcal{M}$, we define

$$d(x_0, x_1)^2 := \inf_{\gamma:[0,1]\to\mathcal{M}} \left\{ \int_0^1 g_{\gamma(s)}(\dot{\gamma}(s), \dot{\gamma}(s))\, ds \;\middle|\; \gamma(0) = x_0,\ \gamma(1) = x_1 \right\}. \tag{3.4}$$

On the formal level, one can easily establish a bound on the rate of change of the distance between a trajectory $x(t)$ of a gradient flow and an arbitrary $x^* \in \mathcal{M}$. For this purpose, we set

$$\begin{aligned} E(t) &:= E(x(t)), \\ D(t) &:= d(x(t), x^*). \end{aligned}$$

Lemma 4 (Dissipation inequality on the formal level)**.** *Let x be a solution of* (3.2) *and $x^* \in \mathcal{M}$. Then it holds*

$$\left| \frac{d}{dt} D(t) \right|^2 \leq -\frac{d}{dt} E(t). \tag{3.5}$$

Proof. Using the triangle inequality, we obtain for every $\delta \in \mathbb{R}$

$$\left| \frac{1}{\delta} (D(t+\delta) - D(t)) \right| \leq \frac{1}{\delta} d(x(t+\delta), x(t)).$$

The curve $s \mapsto x(t + s\delta)$ is admissible in the sense of the definition of d, so that

$$\frac{1}{\delta} d(x(t+\delta), x(t)) \leq \frac{1}{\delta} \int_0^1 \delta \sqrt{g_{x(t+s\delta)}(\dot{x}(t+s\delta), \dot{x}(t+s\delta))}\, ds.$$

Hence, the limit $\delta \to 0$ yields

$$\left| \frac{d}{dt} D(t) \right| \leq \int_0^1 \sqrt{g_{x(t)}(\dot{x}(t), \dot{x}(t))}\, ds = \sqrt{g_{x(t)}(\dot{x}(t), \dot{x}(t))}.$$

On the other hand, we obtain

$$\frac{d}{dt} E(t) = \operatorname{diff} E_{x(t)}.\dot{x}(t) = -g_{x(t)}(\dot{x}(t), \dot{x}(t)),$$

since x is a solution of (3.3). Therefore, the combination of the last two equations yields (3.5). □

Although the proof of this lemma relies on formal arguments, it reveals that using the *natural* distance on the manifold, i.e. the one induced by the metric tensor g, as the suitable length scale, one can expect to obtain an inequality of the form (3.5) for a gradient flow. In Section 3.5, we prove such an inequality on the rigorous level.

3.1.2 From the geometry of the energy landscape to coarsening dynamics

The geometry of the energy landscape is characterized by the rate, at which the energy E can decrease as a function of the distance between the trajectory x and a reference configuration x^*. The lower bound on the rate is determined by the geometric exponent α, see Figure 3.1. On the other hand, the information on the coarsening dynamics is encoded in the rate, at which the energy changes as a function of time characterized by the dynamical exponent γ, see (3.1). The following proposition proves (in a time-averaged sense) that γ and α are related:

$$\gamma = \frac{\alpha}{\alpha + 2}.$$

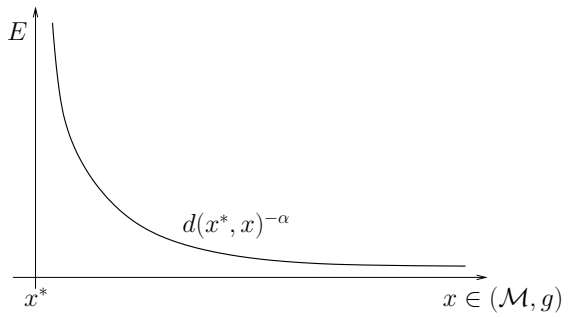

Figure 3.1: The energy $E(x)$ is bounded below by the distance between x and the reference state x^*.

Proposition 3. *Let $x : [0, \infty) \to \mathcal{M}$ be a trajectory of the gradient flow (3.2) with initial value $x(0) = x_0$. Let $x^* \in \mathcal{M}$.*
Assume that for $\alpha > 0$ the interpolation inequality

$$E(x)\, d(x, x^*)^\alpha \geq 1 \tag{3.6}$$

holds for all $x \in \mathcal{M}$ with $E(x) \leq 1$. Then for all $\sigma \in (1, 1 + \frac{2}{\alpha})$ there exists a constant $C(\alpha, \sigma)$ such that $\forall \delta > 0\ \exists C(\delta, \alpha, \sigma)$:

$$\int_0^T E(x(t))^\sigma \, dt \geq (1 - \delta) C(\alpha, \sigma) \int_0^T (t^{-\frac{\alpha}{\alpha+2}})^\sigma \, dt \tag{3.7}$$

provided $T \geq C(\delta, \alpha, \sigma)\, d(x_0, x^*)^{\alpha+2}$ and $E(x_0) \leq 1$.

The last requirement guarantees that $E(x(t)) \leq 1$, so that the trajectory x fulfills the interpolation inequality (3.6) for all $t \geq 0$.

Remark (Notation). To avoid lengthy notations, let us restate the result in the following concise form:

For all $\sigma \in (1, 1 + \frac{2}{\alpha})$ it holds that

$$\int_0^T E(x(t))^\sigma \, dt \gtrsim \int_0^T (t^{-\frac{\alpha}{\alpha+2}})^\sigma \, dt \tag{3.8}$$

provided $T \gg d(x_0, x^*)^{\alpha+2}$ and $E(x_0) \leq 1$.

The notation $\gtrsim$ and $\gg$ are then defined according to the original statement in the proposition.

Proof. Since E is a monotone function of time, $D(t)$ can be viewed as a function of $E(t)$. To distinguish the argument of this function from the actual value of the energy we write $D = D(e)$. Thus, (3.5) turns into

$$1 \ \geq \ \left(\frac{dD}{de}\right)^2 |\dot{E}|. \tag{3.9}$$

Multiplying (3.9) by $E(t)^\sigma$ and integrating in t yield

$$\int_0^T E(t)^\sigma \, dt \geq \int_0^T E(t)^\sigma \left(\frac{dD}{de}\right)^2 |\dot{E}| \, dt = \int_{E_T}^{E_0} e^\sigma \left(\frac{dD}{de}\right)^2 \, de, \tag{3.10}$$

where we have set $E_0 = E(0)$ and $E_T = E(T)$. Then we obtain from the Cauchy–Schwarz inequality

$$\left(\int_{E_T}^{E_0} e^\sigma \left(\frac{dD}{de}\right)^2 \, de \int_{E_T}^{E_0} e^{-\sigma} \, de\right)^{\frac{1}{2}} \geq \left|\int_{E_T}^{E_0} \frac{dD}{de} \, de\right| = |D_0 - D_T|,$$

with $D_0 = D(0)$ and $D_T = D(T)$. Substituting in (3.10) and integrating $\int_{E_T}^{E_0} e^{-\sigma} \, de = (\sigma-1)^{-1}\left(E_T^{1-\sigma} - E_0^{1-\sigma}\right)$ imply

$$\begin{aligned}\int_0^T E(t)^\sigma \, dt &\geq (\sigma-1)\left(E_T^{1-\sigma} - E_0^{1-\sigma}\right)^{-1}(D_0 - D_T)^2 \\ &\geq (\sigma-1)E_T^{\sigma-1}(D_0 - D_T)^2. \end{aligned} \tag{3.11}$$

Here we have used the assumption $\sigma > 1$. We rewrite the right hand side of (3.11) as

$$(\sigma-1)E_T^{\sigma-1-\frac{2}{\alpha}}(E_T D_T^\alpha)^{\frac{2}{\alpha}}\left(1 - \frac{D_0}{D_T}\right)^2$$

and apply the interpolation inequality (3.6), so that

$$\int_0^T E(t)^\sigma \, dt \geq (\sigma-1)E_T^{\sigma-1-\frac{2}{\alpha}}\left(1 - \frac{D_0}{D_T}\right)^2. \tag{3.12}$$

For abbreviation we set

$$f(T) := \int_0^T E(t)^\sigma \, dt.$$

Then (3.12) turns into the differential inequality

$$f(T) \geq (\sigma-1)f'(T)^{(\sigma-1-\frac{2}{\alpha})/\sigma}\left(1 - \frac{D_0}{D_T}\right)^2 = (\sigma-1)f'(T)^{\frac{\sigma\alpha-\alpha-2}{\sigma\alpha}}\left(1 - \frac{D_0}{D_T}\right)^2,$$

or equivalently,

$$f(T)^{\frac{\sigma\alpha}{\alpha+2-\sigma\alpha}} f'(T) \geq \left((\sigma-1)\left(1 - \frac{D_0}{D_T}\right)^2\right)^{\frac{\sigma\alpha}{\alpha+2-\sigma\alpha}}, \tag{3.13}$$

provided $\sigma < 1 + \frac{2}{\alpha}$. Note that

$$f(T)^{\frac{\sigma\alpha}{\alpha+2-\sigma\alpha}} f'(T) = \frac{d}{dt}\left(\frac{f(T)^{\frac{\sigma\alpha}{\alpha+2-\sigma\alpha}+1}}{\frac{\sigma\alpha}{\alpha+2-\sigma\alpha}+1}\right) = \frac{d}{dt}\left(\frac{f(T)^{\frac{\alpha+2}{\alpha+2-\sigma\alpha}}}{\frac{\alpha+2}{\alpha+2-\sigma\alpha}}\right).$$

Now we distinguish two cases. First, when T is such that $D_T \geq C_\delta^{-1} D_0$ with

$$C_\delta := 1 - (1-\delta)^{\frac{\alpha+2}{2\sigma\alpha}},$$

inequality (3.13) yields

$$f(T)^{\frac{\sigma\alpha}{\alpha+2-\sigma\alpha}} f'(T) \geq (\sigma-1)^{\frac{\sigma\alpha}{\alpha+2-\sigma\alpha}} (1-\delta)^{\frac{\alpha+2}{\alpha+2-\sigma\alpha}}. \tag{3.14}$$

Secondly, when T is such that $D_T < C_\delta^{-1} D_0$, we deduce from the interpolation inequality (3.6) that

$$E_T^\sigma \geq D_T^{-\sigma\alpha} \geq C_\delta^{\sigma\alpha} D_0^{-\sigma\alpha}.$$

Since $E(t) \geq E_T$ for all $t < T$, this inequality holds for all $E(t)^\sigma$. In the notation of f, we obtain

$$f'(T)\, D_0^{\sigma\alpha} \geq C_\delta^{\sigma\alpha}. \tag{3.15}$$

Hence, we conclude by combining (3.14) and (3.15)

$$\begin{aligned} \frac{d}{dT}\left(f(T) + \tilde{C}_\delta D_0^{\alpha+2-\sigma\alpha}\right)^{\frac{\sigma\alpha}{\alpha+2-\sigma\alpha}+1} &= \tfrac{\alpha+2}{\alpha+2-\sigma\alpha}\left(f(T) + \tilde{C}_\delta D_0^{\alpha+2-\sigma\alpha}\right)^{\frac{\sigma\alpha}{\alpha+2-\sigma\alpha}}\ f'(T) \\ &\geq \tfrac{\alpha+2}{\alpha+2-\sigma\alpha}(\sigma-1)^{\frac{\sigma\alpha}{\alpha+2-\sigma\alpha}}(1-\delta)^{\frac{\alpha+2}{\alpha+2-\sigma\alpha}}, \end{aligned}$$

where we choose the constant $\tilde{C}_\delta$ such that

$$\tilde{C}_\delta^{\frac{\sigma\alpha}{\alpha+2-\sigma\alpha}} C_\delta^{\sigma\alpha} = (\sigma-1)^{\frac{\sigma\alpha}{\alpha+2-\sigma\alpha}} (1-C_\delta)^{2\frac{\sigma\alpha}{\alpha+2-\sigma\alpha}}.$$

Then we get by integration in time

$$f(T) + \tilde{C}_\delta D_0^{\alpha+2-\sigma\alpha} \geq C(\alpha,\sigma)(1-\delta)\, T^{1-\frac{\sigma\alpha}{\alpha+2}}, \tag{3.16}$$

where $C(\alpha,\sigma)$ is defined by

$$C(\alpha,\sigma) := \left(\tfrac{\alpha+2}{\alpha+2-\sigma\alpha}\right)^{1-\frac{\sigma\alpha}{\alpha+2}} (\sigma-1)^{\frac{\sigma\alpha}{\alpha+2}}. \tag{3.17}$$

Finally, for T such that

$$C(\alpha,\sigma)(1-\delta)\, T^{1-\frac{\sigma\alpha}{\alpha+2}} \geq \tfrac{1}{2}\tilde{C}_\delta D_0^{\alpha+2-\sigma\alpha},$$

or equivalently,

$$T \geq (C(\alpha,\sigma)(1-\delta))^{-\frac{\alpha+2}{\alpha+2-\sigma\alpha}} \left(\tfrac{1}{2}\tilde{C}_\delta\right)^{\frac{\alpha+2}{\alpha+2-\sigma\alpha}}\ D_0^{\alpha+2}, \tag{3.18}$$

we obtain from (3.16) the desired inequality (3.7):

$$f(T) \geq C(\alpha,\sigma)(1-\delta)\, T^{1-\frac{\sigma\alpha}{\alpha+2}},$$

provided $T \geq C(\delta,\alpha,\sigma) D_0^{\alpha+2}$. The constant $C(\delta,\alpha,\sigma)$ is defined by (3.18). □

Remark. Equations (3.2) and (3.6) do not imply a *pointwise* estimate for the energy of the form

$$E(t) \gtrsim t^{-\frac{\alpha}{\alpha+2}}. \tag{3.19}$$

Indeed, let $\mathcal{M} = \mathbb{R}_+$, $x^* = 0$ and $x(0) = 1$. For a given $b \gg 1$ let E_b be equal to $x^{-\alpha}$ outside the interval $(1, b)$ and linear on $[1, b]$ such that E_b is continuous:

$$E_b(x) := \begin{cases} 1 + \frac{b^{-\alpha}-1}{b-1}(x-1) & \text{for } x \in [1,b], \\ x^{-\alpha} & \text{else.} \end{cases} \tag{3.20}$$

Then it holds

$$\dot{x} \;=\; -\frac{dE_b}{dx}(x(t)) = -\frac{b^{-\alpha}-1}{b-1}$$

as long as $x(t) \le b$. Hence,

$$x(t) = 1 - \frac{b^{-\alpha}-1}{b-1}t$$

and therefore $x(t_b) = b$ for $t_b := \frac{(b-1)^2}{1-b^{-\alpha}}$. Thus,

$$\frac{E_b(x(t_b))}{t_b^{-\frac{\alpha}{\alpha+2}}} \;=\; \frac{(b-1)^{\frac{2\alpha}{\alpha+2}}}{b^\alpha(1-b^{-\alpha})^{\frac{\alpha}{\alpha+2}}} \;\le\; 2b^{-\frac{\alpha^2}{\alpha+2}} \to 0$$

for $b \to \infty$ in contradiction to (3.19).

Remark (Optimality of $C(\alpha, \sigma)$). The coefficient $C(\alpha, \sigma)$ is optimal for $\sigma = 1 + \frac{1}{\alpha}$, see Figure 3.2. Indeed, consider in 1-d the energy $E(x) := x^{-\alpha}$. Obviously, this energy

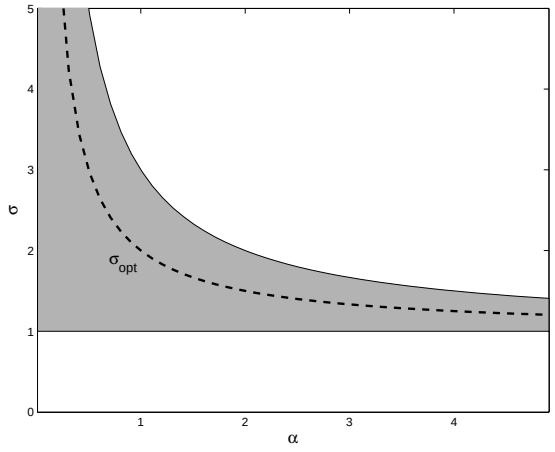

Figure 3.2: Permitted values of σ (grey region) as a function of α. The dotted line $\sigma_{\text{opt}} := 1 + \frac{1}{\alpha}$ indicates the values of σ, for which the coefficient in (3.7) is optimal.

obeys the interpolation inequality (3.6) for $x^* = 0$. The gradient flow of E with $x_0 = 0$ is given by

$$x(t) = (\alpha(\alpha+2)t)^{\frac{1}{\alpha+2}}.$$

Hence,

$$E(x(t)) = x(t)^{-\alpha} = (\alpha(\alpha+2)t)^{-\frac{\alpha}{\alpha+2}}$$

and furthermore,

$$\int_0^T E(t)^\sigma \, dt = (\alpha(\alpha+2))^{-\sigma\frac{\alpha}{\alpha+2}} \frac{\alpha+2}{\alpha+2-\sigma\alpha} \, T^{1-\sigma\frac{\alpha}{\alpha+2}}.$$

The coefficient coincides with the coefficient in (3.17) provided $\sigma = 1 + \frac{1}{\alpha}$.

3.2 Gradient flow structure of the thin-film equation

In this section, we interpret the evolution (1.1) of the film height h *formally* as a gradient flow w.r.t. the energy functional (1.20) on a Riemannian manifold $(\mathcal{M}, g)$.

For this purpose, we define the manifold $\mathcal{M}$ as the set of all film configurations with fixed mass described by the film height h:

$$\mathcal{M} := \left\{ h \;\middle|\; \int h(x)\, dx = \int h^* \, dx \right\}. \tag{3.21}$$

Here we denote by $h^* \equiv$ const the average film height.

The choice of the metric tensor g is physically motivated. We define it as the minimal energy dissipation rate by viscous friction of a transport flux generated by $\delta h \in T_h\mathcal{M}$ (see equation (1.25)):

$$g_h(\delta h, \delta h) := \min_u \left\{ \int \frac{1}{m} h^2 |u|^2 \, dx \;\middle|\; \delta h + \nabla\cdot(hu) = 0 \right\} \tag{3.22}$$

with no-flux boundary condition $u \cdot \nu = 0$. Note that the metric tensor depends on the base point h, and furthermore on the mobility m.

A variation in u reveals that $\frac{1}{m}hu$ is a gradient. Hence, the Euler–Lagrange equation of (3.22) allows us to define the metric tensor in terms of a potential φ:

$$g_h(\delta h, \delta h) = \int m|\nabla\varphi|^2 \, dx, \qquad \text{where } \; \delta h + \nabla\cdot(m\nabla\varphi) = 0$$

with no-flux boundary condition $\nabla\varphi \cdot \nu = 0$. This type of weighted H^{-1}-norm reveals the analogy of the thin-film equation to the Cahn–Hilliard equation.

By the polarization formula for bilinear forms, one gets

$$g_h(\delta h_1, \delta h_2) = \int m\nabla\varphi_1 \cdot \nabla\varphi_2 \, dx, \qquad \text{where } \; \delta h_i + \nabla\cdot(m\nabla\varphi_i) = 0, \;\; i = 1, 2. \tag{3.23}$$

Now, it is easy to derive the thin-film equation (1.1) from the gradient flow structure on the Riemannian manifold $(\mathcal{M}, g)$ (defined by (3.21) and (3.23)) w.r.t. the energy (1.20): On the one hand,

$$\begin{aligned} g_{h(t)}(\partial_t h, \delta h) &\overset{(3.23)}{=} \int m\nabla\varphi_\delta \cdot \nabla\varphi \, dx \quad \text{with} \quad \begin{array}{c} \partial_t h + \nabla\cdot(m\nabla\varphi_\delta) = 0, \\ \delta h + \nabla\cdot(m\nabla\varphi) = 0, \end{array} \\ &= \int \partial_t h \, \varphi \, dx. \end{aligned}$$

On the other hand, according to (1.21),

$$\operatorname{diff} E_{h(t)}.\delta h = \int \frac{\delta E}{\delta h} \, \delta h \, dx = \int \left(-\nabla \cdot \left(m \nabla \frac{\delta E}{\delta h} \right) \right) \, \varphi \, dx,$$

so that the combination of these two equations by (3.3) yields the thin-film equation.

Remark (Lifted metric tensor and connections to the Rayleigh principle). The gradient flow equation (3.3) can be regarded as the Euler–Lagrange equation of

$$\tfrac{1}{2} g_{h(t)}(\delta h, \delta h) + \operatorname{diff} E_{h(t)}.\delta h$$

with respect to δh, where $\partial_t h$ is the minimizer under all tangent vectors. According to definition (3.22) of the metric tensor, the tangent vector δh and the velocity u linearly depend upon each other through the continuity equation. Hence, the tensor can be lifted from the tangent space onto the space of all admissible velocities. Then we can reformulate the gradient flow evolution as follows: The film height h evolves according to

$$\partial_t h + \nabla \cdot (hu) = 0,$$

where u minimizes

$$\tfrac{1}{2} g_{h(t)}(u, u) + \operatorname{diff} E_{h(t)}.u.$$

Here, g is defined by $g_h(u,u) = \int \frac{1}{m} h^2 |u|^2 \, dx$, which is exactly the dissipation D in (1.25), and $\operatorname{diff} E_{h(t)}.u$ is derived from $\operatorname{diff} E_{h(t)}.\delta h$ via the continuity equation, see (1.21). This enlightens the connection to the Rayleigh principle (1.24), since the "lifted" gradient flow can be seen as the Euler–Lagrange equation of the Rayleigh functional $\mathcal{R}$ subject to the continuity equation.

In the case of linear mobility $m(h) = h$, the natural distance (as defined in (3.4)) with respect to the metric tensor (3.22) can be explicitly given. As was shown in [31], the induced distance is the quadratic Wasserstein distance defined by

$$\mathcal{W}(h_0, h_1)^2 \; := \; \inf \left\{ \iint |x-y|^2 d\pi(x,y) \;\middle|\; \int d\pi(\cdot, y) = h_0, \int d\pi(x, \cdot) = h_1 \right\}. \quad (3.24)$$

As an important particular case of a Monge-Kantorovich distance (as introduced in [37]) it measures the minimal costs for the transport of the "density" h_0 into "density" h_1 in terms of the squared Euclidean distance. The so-called *transportation plan* π, a

measure on the product space $\Omega\times\Omega$, is admissible if its projection on the first and second coordinates are measures with densities h_0 and h_1, respectively. For further properties of $\mathcal{W}$, we refer to Section 7.1 in [37].

Hence, for the case $q = 1$, one can expect to get a dissipation inequality for the induced distance as stated in Lemma 4. This is done rigorously in Lemma 9. Otherwise for the cases $q \neq 1$, the natural distance induced by the tensor g is not explicitly known, so that an alternative definition of a length scale for proving a type of dissipation inequality would be required.

3.3 The main result: A lower bound on the energy

Based on the abstract framework, we can prove the following lower bound on the energy density in a time-averaged sense for arbitrary dimension:

Theorem 1 (Lower bound on energy)**.** *Let the potential $\mathcal{U}$ satisfy*

$$\begin{aligned} &\mathcal{U}(h) \geq 0 \quad \text{on } (0,\infty), \\ &\mathcal{U}(h) \geq 1 \quad \text{on } (2,\infty). \end{aligned} \tag{3.25}$$

Let h be a smooth solution of (1.1) for $q = 1$ on a large domain $\Omega := [0,\Lambda]^d$, $\Lambda \gg 1$, with total mass equal to a uniform configuration of constant film height 3:

$$\int h\,dx \;=\; \int h^*\,dx, \quad h^* \equiv 3. \tag{3.26}$$

Then for $\sigma \in (1, \frac{3d+2}{d})$, the estimate

$$\int_0^T \Big(\Lambda^{-d} E(h(t))\Big)^{\sigma}\,dt \quad \gtrsim \quad \int_0^T (t^{-\frac{d}{3d+2}})^{\sigma}\,dt \tag{3.27}$$

holds, provided $T \gg \Big(\Lambda^{-\frac{d}{2}}\mathcal{W}(3,h(0))\Big)^{\frac{3d+2}{d+1}}$ and $\Lambda^{-d}E(h(0)) \ll 1$.

Remark. Let us give some explanations regarding the assumptions made in the theorem:

- The assumption $\Lambda^{-d}E(h(0)) \ll 1$ of an initially small energy density states that the initial configuration is energetically comparable to a configuration of well-separated droplets connected by a precursor of height argmin $\mathcal{U} \approx 1$.
- On the other hand, the assumption $T \gg \Big(\Lambda^{-\frac{d}{2}}\mathcal{W}(3,h(0))\Big)^{\frac{3d+2}{d+1}}$ encodes that the initial configuration $h(0)$ is not too far away from the constant film $h^* = 3$.
- The constants 1 and 2 in (3.25) and 3 in (3.26) are chosen purely for convenience. In particular, any uniform film of height larger than 2 would give the same result. Of course, the constant in (3.27) depends on h^*. A closer inspection of the scaling relations in Section 3.6 reveals that the constant scales in h^* as $(h^*)^{\frac{3d}{2(d+1)}}$.

In particular, the theorem shows that the interpolation inequality depends on the dimension

$$\alpha = \frac{d}{d+1},$$

and therefore yields a dimension-depending bound. In contrast, the geometric exponent in the context of the Cahn–Hilliard equation in [19] is equal to 1, independent of the dimension. An obvious difference lies in a "mixed dimensionality" of our coarsening problem: The mass exchange between the droplets, i.e. kinetics, is governed by a flux through the precursor film on the d-dimensional substrate. On the other hand, energetics (e.g. in form of surface tension) is $(d+1)$-dimensional.

To apply the abstract result in Proposition 3, we must provide a rigorous proof of an interpolation inequality of the form (3.6) with the geometric exponent α as above and, furthermore, of the dissipation inequality (3.5). This will be done in the following two sections. In addition, we will give heuristic scaling arguments in Section 3.6, i.a. to deduce an upper bound on coarsening rates from the lower bound on the energy, and to motivate the dependence of α on the dimension.

3.4 Interpolation inequality

As can be seen from the abstract framework, a main ingredient for proving a lower bound on the energy is an interpolation inequality, which relates the energy density and the induced distance via the geometric exponent.

Proposition 4 (Interpolation inequality)**.** *There exists a constant $C = C(d) > 0$ such that*

$$\Lambda^{-d} E(h) \, \left(\Lambda^{-\frac{d}{2}} \mathcal{W}(h,3)\right)^{\frac{d}{d+1}} \geq \frac{1}{C} \qquad \textit{provided} \quad \Lambda^{-d} E(h) \leq \frac{1}{C}, \; \Lambda \geq C.$$

For the rigorous proof of Proposition 4, let us set

$$R := (\Lambda^{-d} E(h))^{-1} \qquad \text{and} \qquad \underline{h} := (h-2)_+. \tag{3.28}$$

Note that the definition of R is motivated by dynamical scaling relations, which are heuristically derived in Section 3.6.1. Also inspired by these scaling relations, the proof is split into several lemmas:

1. Lemma 5 shows that the average droplet height H scales like the average droplet radius in accordance with (3.52). The radius is expressed in terms of the energy, see (3.28).

2. Lemma 6, applied to $\underline{h}$, shows that most of the droplet mass lies in a "small" set in the sense that the volume of the thickened set is controlled.

3. Lemmas 5 and 6 imply Lemma 7, which shows that the typical droplet distance L scales like $R^{\frac{d+1}{d}}$, as suggested by the heuristic arguments in (3.53).

4. Finally, Lemma 8 reveals that for sufficiently distant droplets, the averaged Wasserstein distance between h and the average height scales like L in accordance with (3.57).

Now let us present the detailed statements and their proofs:

Lemma 5.

1. *The typical droplet height H is at least of order R in the sense that*

$$\int_{\{\underline{h}>H\}} \underline{h}\, dx \geq \tfrac{1}{2} \int \underline{h}\, dx \qquad \text{for } H = \tfrac{R}{2}. \tag{3.29}$$

2. *The typical droplet radius is at least of the order R in the sense that*

$$R \int |\nabla \underline{h}|\, dx \leq \int \underline{h}\, dx. \tag{3.30}$$

Proof. We first notice that $h \leq \underline{h} + 2$ implies

$$\int h\, dx \leq \int \underline{h}\, dx + \tfrac{2}{3} \int 3\, dx \overset{(3.26)}{=} \int \underline{h}\, dx + \tfrac{2}{3} \int h\, dx,$$

so that

$$\int \underline{h}\, dx \geq \tfrac{1}{3} \int h\, dx. \tag{3.31}$$

Next we notice that

$$\Lambda^{-d} E(h) \overset{(3.26)}{=} \tfrac{3}{\int h\, dx} \int \tfrac{1}{2}|\nabla h|^2 + \mathcal{U}(h)\, dx \overset{(3.25)}{\geq} \tfrac{3}{\int h\, dx} \operatorname{vol}\left(\{h > 2\}\right),$$

so that by (3.28)

$$\operatorname{vol}\left(\{h > 2\}\right) \leq \tfrac{1}{3R} \int h\, dx. \tag{3.32}$$

This inequality induces

$$\begin{aligned} \int_{\{\underline{h}\leq H\}} \underline{h}\, dx &= \int_{\{2<h\leq H+2\}} (h-2)\, dx \\ &\leq H \operatorname{vol}\left(\{h > 2\}\right) \\ &\overset{(3.32)}{\leq} \tfrac{H}{3R} \int h\, dx \\ &\overset{(3.31)}{\leq} \tfrac{H}{R} \int \underline{h}\, dx. \end{aligned}$$

Hence, we obtain (3.29) the estimate

$$\int_{\{\underline{h}>H\}} \underline{h}\, dx = \int \underline{h}\, dx - \int_{\{\underline{h}\leq H\}} \underline{h}\, dx \geq \left(1 - \tfrac{H}{R}\right) \int \underline{h}\, dx,$$

which motivates the choice of H.

Now we turn to (3.30):

$$\begin{aligned}
\int |\nabla \underline{h}|\, dx &= \int_{\{h>2\}} |\nabla h|\, dx \\
&\overset{(3.25)}{\leq} \int |\nabla h| \sqrt{\mathcal{U}(h)}\, dx \\
&\leq \int \tfrac{1}{2}|\nabla h|^2 + \mathcal{U}(h)\, dx \\
&\overset{(3.26)}{=} \tfrac{\int h\, dx}{3\Lambda^d} \int \tfrac{1}{2}|\nabla h|^2 + \mathcal{U}(h)\, dx \\
&\overset{(3.31)}{\leq} \Lambda^{-d} E(h) \int \underline{h}\, dx.
\end{aligned}$$

According to (3.28), this turns into

$$R \int |\nabla \underline{h}|\, dx \leq \int \underline{h}\, dx,$$

which concludes the proof. □

The next lemma is strongly inspired by Lemma 2.1 in [5].

Lemma 6. *Let $R \leq \Lambda$. Assume that $g : (0,\Lambda)^d \to [0,\infty)$*

1. *has height H in the sense that*

$$\int_{\{g\geq H\}} g\, dx \geq \tfrac{1}{2} \int g\, dx \tag{3.33}$$

2. *and radius R in the sense that*

$$R \int |\nabla g|\, dx \leq \int g\, dx. \tag{3.34}$$

Then there exists a set $A_R \subset \{g \geq H\}$,

1. *which contains substantial mass in the sense that*

$$\int_{A_R} g\, dx \geq \tfrac{1}{4} \int g\, dx,$$

2. *and is small in the sense that the volume of the thickened sets*

$$A_R^\delta := \{x \in (0,\Lambda)^d \mid dist(x, A_R) < \delta\}$$

is controlled by

$$vol\left(A_R^\delta\right) \leq 3^d 2^{d+1} \left(1 + 4\tfrac{\delta}{R}\right)^\delta \tfrac{1}{H} \int g\, dx \qquad \text{for all } \delta > 0.$$

Proof. First, we extend $g : [0,\Lambda]^d \to \mathbb{R}$ to the domain $[-\Lambda,\Lambda]^d$ by even reflection and subsequently to $\mathbb{R}^d$ by periodic continuation, and denote the extension by $\overline{g} : \mathbb{R}^d \to \mathbb{R}$. Let us set for convenience $\overline{A} := \{\overline{g} \geq H\}$ and define

$$\overline{A}_R := \left\{ x \in \overline{A} \;\middle|\; \int_{B_{\frac{R}{8}}(x)} \overline{g}\, dy \geq \tfrac{H}{2} \operatorname{vol}\left(B_{\frac{R}{8}}(x)\right) \right\}. \tag{3.35}$$

With the help of the convolution of $\overline{g}$ defined by

$$\overline{g}_R(x) := \frac{1}{\operatorname{vol}\left(B_{\frac{R}{8}}(x)\right)} \int_{B_{\frac{R}{8}}(x)} \overline{g}\, dy,$$

$\overline{A}_R$ can be written as $\overline{A}_R = \{x \in \overline{A} \mid \overline{g}_R(x) \geq \frac{H}{2}\}$. Next we recall the standard estimate

$$\int_{(-\Lambda,\Lambda)^d} |\overline{g} - \overline{g}_R|\, dx \leq \tfrac{R}{8} \int_{(-\Lambda,\Lambda)^d} |\nabla \overline{g}|\, dx \overset{(3.34)}{\leq} \tfrac{1}{8} \int_{(-\Lambda,\Lambda)^d} \overline{g}\, dx.$$

Since the integrands are even functions, this yields

$$\int |g - \overline{g}_R|\, dx \leq \tfrac{1}{8} \int g\, dx. \tag{3.36}$$

We now define $A := \overline{A} \cap (0,\Lambda)^d$ and $A_R := \overline{A}_R \cap (0,\Lambda)^d$. Then we have

$$g \geq H \geq 2\overline{g}_R \quad \text{on } A - A_R$$

and thus,

$$g \leq 2(g - \overline{g}_R) \quad \text{on } A - A_R.$$

Therefore,

$$\int_{A-A_R} g\, dx \leq 2 \int_{A-A_R} (g - \overline{g}_R)\, dx \leq 2 \int |g - \overline{g}_R|\, dx \overset{(3.36)}{\leq} \tfrac{1}{4} \int g\, dx. \tag{3.37}$$

Notice that by assumption (3.33), $\int_A g\, dx \geq \frac{1}{2} \int g\, dx$. Hence,

$$\begin{aligned} \int g\, dx &\leq 2 \int_A g\, dx \\ &\leq 2 \left(\int_{A_R} g\, dx + \int_{A-A_R} g\, dx \right) \\ &\overset{(3.37)}{\leq} 2 \int_{A_R} g\, dx + \tfrac{1}{2} \int g\, dx, \end{aligned}$$

which yields the first assertion.

Let $\mathfrak{I} \subset A_R$ be maximal with the property

$$\left\{ B_{\frac{R}{8}}(x) \right\}_{x \in \mathfrak{I}} \text{ are disjoint.} \tag{3.38}$$

Then necessarily,

$$A_R \subset \bigcup_{x \in \mathfrak{I}} B_{\frac{R}{4}}(x). \tag{3.39}$$

Thus,

$$\begin{aligned} \#\mathfrak{I} \text{ vol} \left(B_{\frac{R}{8}}(0) \right) &= \sum_{x \in \mathfrak{I}} \text{vol} \left(B_{\frac{R}{8}}(x) \right) \\ &\overset{(3.35)}{\leq} \frac{2}{H} \sum_{x \in \mathfrak{I}} \int_{B_{\frac{R}{8}}(x)} \overline{g} \, dx \\ &\overset{(3.38)}{\leq} \frac{2}{H} \int_{(-\Lambda, 2\Lambda)^d} \overline{g} \, dx \\ &= 3^d \frac{2}{H} \int g \, dx. \end{aligned} \tag{3.40}$$

Here we used the assumption $R \leq \Lambda$.
Now (3.39) implies $A_R^\delta \subset \bigcup_{x \in \mathfrak{I}} B_{\frac{R}{4}+\delta}(x)$, so that

$$\begin{aligned} \text{vol} \left(A_R^d \right) &\leq \#\mathfrak{I} \text{ vol} \left(B_{\frac{R}{4}+\delta}(0) \right) \\ &= \frac{\text{vol} \left(B_{\frac{R}{4}+\delta}(0) \right)}{\text{vol} \left(B_{\frac{R}{8}}(0) \right)} \#\mathfrak{I} \text{ vol} \left(B_{\frac{R}{8}}(0) \right) \\ &\overset{(3.40)}{\leq} 3^d (\tfrac{8}{R}(\tfrac{R}{4} + \delta))^d \frac{2}{H} \int g \, dx \\ &= 3^d 2^{d+1} (1 + 4\tfrac{\delta}{R})^d \frac{1}{H} \int g \, dx, \end{aligned}$$

which proves the second assertion. □

Lemma 7. *Let $\Lambda \geq R \geq 3^d 2^{8d}$. Then the typical droplet distance L is at least of the order $R^{\frac{d+1}{d}}$ in the following sense: There exists a set $A_R \subset \mathbb{R}^d$ such that*

1. $$\int_{A_R} h \, dx \geq \tfrac{1}{12} \int h \, dx, \tag{3.41}$$

2. $$3 \, vol \left(A_R^L \right) \leq \tfrac{3}{4} \int_{A_R} h \, dx \quad \text{for } L = 3^{-1} 2^{-10} R^{\frac{d+1}{d}}. \tag{3.42}$$

Proof. According to Lemma 6 there exists a set A_R such that

$$\int_{A_R} \underline{h}\, dx \geq \tfrac{1}{4} \int \underline{h}\, dx, \tag{3.43}$$

which by (3.31) turns into (3.41), and

$$\mathrm{vol}\left(A_R^L\right) \leq 3^d 2^{d+1} \left(1 + 4\tfrac{L}{R}\right)^d \tfrac{1}{H} \int \underline{h}\, dx. \tag{3.44}$$

By the definition of H and R in Lemma 5, (3.44) gives rise to

$$\begin{aligned} \mathrm{vol}\left(A_R^L\right) &\leq 3^d 2^{d+2} \left(1 + 4\tfrac{L}{R}\right)^d \tfrac{1}{R} \int \underline{h}\, dx \\ &\overset{(3.43)}{\leq} 3^d 2^{d+4} \left(1 + 4\tfrac{L}{R}\right)^d \tfrac{1}{R} \int_{A_R} \underline{h}\, dx \\ &\leq 3^d 2^{d+4} \left(1 + 4\tfrac{L}{R}\right)^d \tfrac{1}{R} \int_{A_R} h\, dx. \end{aligned}$$

Now L in (3.42) is defined such that

$$3^d 2^{d+4} \left(1 + 4\tfrac{L}{R}\right)^d \tfrac{1}{R} \leq \tfrac{1}{4}$$

provided $R \geq 3^d 2^{8d}$. Hence, the inequality turns into

$$3\,\mathrm{vol}\left(A_R^L\right) \leq \tfrac{3}{4} \int_{A_R} h\, dx.$$

□

Lemma 8. *Let $h : Q \to [0, \infty)$ with $h^* := \Lambda^{-d} \int h(x)\, dx$ and $A \subset \mathbb{R}^d$ and $L > 0$ be given with*

$$h^*\, vol(\{dist(\cdot, A) < L\}) \leq \tfrac{3}{4} \int_A h(x)\, dx. \tag{3.45}$$

Then

$$\mathcal{W}(h, h^*)^2 \geq \tfrac{1}{4} L^2 \int_A h(x)\, dx.$$

Proof. Set for abbreviation $A^L := \{\mathrm{dist}(., A) < L\}$. Let π be any admissible transportation plan in the definition of $\mathcal{W}$. We conclude

$$\begin{aligned} \int_{\mathbb{R}^d \times \mathbb{R}^d} |x - y|^2\, d\pi(x, y) &\geq \int_{A \times (\mathbb{R}^d - A^L)} |x - y|^2\, d\pi(x, y) \\ &\geq L^2 \pi(A \times (\mathbb{R}^d - A^L)) \\ &\geq L^2 (\pi(A \times \mathbb{R}^d) - \pi(\mathbb{R}^d \times A^L)) \\ &= L^2 \left(\int_A h\, dx - \int_{A^L} h^*\, dx \right) \\ &= L^2 \left(\int_A h\, dx - h^* \,\mathrm{vol}\left(A^L\right) \right) \\ &\overset{(3.45)}{\geq} \tfrac{1}{4} L^2 \int_A h\, dx. \end{aligned}$$

□

Proof of Proposition 4. According to Lemma 8 (applied to $h^* = 3$ and $A = A_R$), it follows from Lemma 7 for the L defined in (3.42)

$$\mathcal{W}(h,3)^2 \geq \tfrac{1}{4}L^2 \int_{A_R} h\,dx \overset{(3.41)}{\geq} \tfrac{1}{48}L^2 \int h\,dx.$$

In view of (3.26), this turns into

$$\Lambda^{-d}\mathcal{W}(h,3)^2 \geq 2^{-4}L^2.$$

In view of the definition (3.28) of R and the definition (3.42) of L, this yields

$$\begin{aligned}\Lambda^{-d}E(h)\ \left(\Lambda^{-\frac{d}{2}}\mathcal{W}(h,3)\right)^{\frac{d}{d+1}} &\geq R^{-1}(2^{-4}L^2)^{\frac{d}{2(d+1)}} \\ &= R^{-1}(3^{-2}2^{-24}R^{2\frac{d+1}{d}})^{\frac{d}{2(d+1)}} \\ &= 3^{-\frac{d}{d+1}}2^{-\frac{12d}{d+1}}.\end{aligned}$$

Since $3^{-\frac{d}{d+1}}2^{-\frac{12d}{d+1}} > 3^{-d}2^{-8d}$, we set $C := 3^{\frac{d}{d+1}}2^{\frac{12d}{d+1}}$, which concludes the proof of the interpolation inequality. □

3.5 Dissipation inequality

The formal argument in Lemma 4 is replaced by the rigorous proof of the inequality

$$\left|\frac{d}{dt}\mathcal{W}(h(t),h^*)\right|^2 \leq \left(-\frac{d}{dt}E(t)\right). \tag{3.46}$$

Recall that

$$\frac{d}{dt}E(h(t)) = \int \frac{\delta E}{\delta h}\nabla\cdot\left(h\nabla\frac{\delta E}{\delta h}\right)\,dx = -\int h\left|\nabla\frac{\delta E}{\delta h}\right|^2\,dx.$$

Hence, we prove the following more general result:

Lemma 9 (Dissipation inequality)**.** *Let h be a solution of the continuity equation*

$$\partial_t h + \nabla\cdot(hu) = 0, \tag{3.47}$$

where the vector field u is smooth, bounded on Ω and locally bounded on $t \in [0,\infty)$. Then it holds that

$$\left|\frac{d}{dt}\mathcal{W}(h(t),h^*)\right|^2 \leq \int h(t,x)|u(t,x)|^2\,dx. \tag{3.48}$$

Proof. The proof is based on [30], but let us give the arguments for completeness. Due to the triangle inequality one has

$$|\mathcal{W}(h(t+s),h^*)-\mathcal{W}(h(t),h^*)|\le\mathcal{W}(h(t+s),h(t)),$$

so that it is sufficient to prove the inequality

$$\lim_{s\downarrow 0}\frac{1}{s}\mathcal{W}(h(t+s),h(t))\le\sqrt{\int h(t,x)|u(t,x)|^2\,dx}. \tag{3.49}$$

As a first step, we show that $h(t+s)$ is the "push-forward" of $h(t)$ under the diffeomorphic flow $\Phi:[0,\infty)\times\Omega\to\Omega$ generated by u, which is defined by

$$\partial_s\Phi(s)=u(t+s)\circ\Phi(s),\qquad \Phi(0)=\mathrm{id}. \tag{3.50}$$

A push-forward is given by

$$\int\zeta(x)\,h(t+s,x)\,dx=\int\zeta(\Phi(s,y))\,h(t,y)\,dy\qquad\text{for all }\zeta\in C_0^\infty(\Omega),$$

or, equivalently,

$$\int\zeta(\Phi^{-1}(s,y))\,h(t+s,y)\,dy=\int\zeta(x)\,h(t,x)\,dx\qquad\text{for all }\zeta\in C_0^\infty(\Omega). \tag{3.51}$$

For this purpose, we set for abbreviation $\zeta_s:=\zeta\circ\Phi^{-1}(s,.)$, so that $\zeta_s\circ\Phi=\zeta$. By the chain rule it is easy to see that ζ_s satisfies

$$\partial_s\zeta_s+u(t+s)\cdot\nabla\zeta_s=0.$$

Obviously, $h(t+s)$ fulfills the continuity equation

$$\partial_s h(t+s)+\nabla\cdot(h(t+s)u(t+s))=0.$$

Now note that (3.51) holds for $s=0$ due to the definition of the flow. Since the right hand side of (3.51) is independent of s, it is sufficient to show that the left hand side is constant in s:

$$\begin{aligned}
&\frac{d}{ds}\int\zeta_s(x)h(t+s,x)\,dx\\
&\quad=\int\partial_s\zeta_s(x)h(t+s,x)+\partial_s h(t+s,x)\zeta_s(x)\,dx\\
&\quad=\int(-u(t+s,x)\cdot\nabla\zeta_s(x)h(t+s,x)-\nabla\cdot(h(t+s,x)u(t+s,x))\zeta_s(x))\,dx\\
&\quad=\int(\nabla\cdot(h(t+s,x)u(t+s,x))-\nabla\cdot(h(t+s,x)u(t+s,x)))\,\zeta_s(x)\,dx=0.
\end{aligned}$$

Next we define an (in the sense of the definition of $\mathcal{W}$) admissible transport plan π_s on the product space $\Omega \times \Omega$, which realizes the transport of the configuration $h(t)$ by the flow $\Phi(s)$: Let $\pi_s : \Omega \times \Omega \to [0, \infty)$ be defined by

$$\int_{\Omega\times\Omega} \zeta(x,y)\, d\pi_s(x,y) = \int_\Omega \zeta(x, \Phi(s,x))h(t,x)\, dx \qquad \text{for all } \zeta \in C_0^0(\Omega \times \Omega).$$

Indeed, π_s is admissible: For arbitrary $\zeta_1, \zeta_2 \in C_0^0(\Omega)$ it holds

$$\begin{aligned}\int_{\Omega\times\Omega} (\zeta_1(x) + \zeta_2(y))\ d\pi_s(x,y) &= \int_\Omega (\zeta_1(x) + \zeta_2(\Phi(s,x)))\ h(t,x)\, dx \\ &= \int_\Omega \zeta_1(x)h(t,x)\, dx + \int_\Omega \zeta_2(x)h(t+s,x)\, dx.\end{aligned}$$

Thus, according to the definition of $\mathcal{W}$, one has

$$\frac{1}{s}\mathcal{W}(h(t), h(t+s)) \le \sqrt{\int \frac{1}{s^2}|x - \Phi(s,x)|^2 h(t,x)\, dx}.$$

The integrand converges pointwise:

$$\lim_{s\downarrow 0} \frac{1}{s^2}|x - \Phi(s,x)|^2 = |\partial_s \Phi(s,x)\big|_{s=0}|^2 = |u(t,x)|^2,$$

and is bounded by $|u(t+s,x)|^2$. Hence, we obtain by Lebesgue

$$\lim_{s\downarrow 0} \frac{1}{s}\mathcal{W}(h(t), h(t+s)) \le \sqrt{\int |u(t,x)|^2 h(t,x)\, dx},$$

which completes the proof of the lemma. □

3.6 Heuristics

The coarsening process relies on rather complex mechanisms. Nevertheless, numerical simulations suggest that the dynamics has a simple statistical behavior, meaning that a typical length scale like the averaged distance L, which measures the "coarseness" of the configuration, has – as a function of time – a power-law behavior:

$$L(t) \sim t^\beta.$$

In the following section, we will heuristically deduce from a quasi-stationary set-up why a lower bound on the energy E of the form (3.1) yields an upper bound on coarsening rate characterized by β.

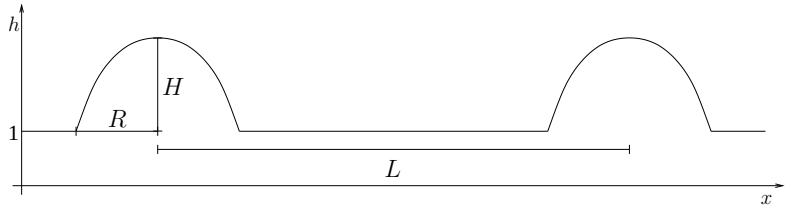

Figure 3.3: Droplet configuration on one-dimensional substrate.

3.6.1 Dynamical scaling

We consider a configuration of well-separated, large droplets. Furthermore, we assume that the average height is of order 1. Such configuration has three typical length scales: the average droplet height H, the average droplet size given by the radius R and the typical distance L between droplets, see Figure 3.3. By scaling, these averaged quantities are not independent:

- On a mesoscopic level, we obtain from (2.27) that the height H and the radius R of the mesoscopic equilibrium droplets scale the same:

$$H \sim R. \tag{3.52}$$

- We infer from mass conservation, i.e.

$$\Lambda^{-d} \int h \, dx \sim 1,$$

and from

$$\begin{aligned} \Lambda^{-d} \int h \, dx &\sim \left(\begin{array}{c} \text{number density} \\ \text{of droplets} \end{array} \right) \times \left(\begin{array}{c} \text{volume of} \\ \text{individual droplet} \end{array} \right) \\ &\sim L^{-d} \times H R^d \\ &\overset{(3.52)}{\sim} L^{-d} \times R^{d+1} \end{aligned}$$

that R and L are related by

$$L \sim R^{\frac{d+1}{d}}. \tag{3.53}$$

Therefore, combining (3.52) and (3.53) we obtain the scaling relation

$$H \sim R \sim L^{\frac{d}{d+1}}.$$

From a lower bound on the energy to an upper bound on coarsening

Now it is easy to relate the energy density and the typical distance by scaling. Using (2.35a), we get

$$\begin{aligned} \Lambda^{-d} E &\sim \begin{pmatrix} \text{number density} \\ \text{of droplets} \end{pmatrix} \times \begin{pmatrix} \text{energy of} \\ \text{individual droplet} \end{pmatrix} \\ &\sim L^{-d} \times R^d \\ &\overset{(3.53)}{\sim} L^{-\frac{d}{d+1}}. \end{aligned} \tag{3.54}$$

Hence, a lower bound on the energy

$$\Lambda^{-d} E(t) \gtrsim t^{-\frac{d}{3d+2}}$$

as implied by (3.27) would give an upper bound on L:

$$L(t) \lesssim t^{\frac{d+1}{3d+2}}. \tag{3.55}$$

In particular, in one and two dimension, the coarsening exponent is bounded by

$$\beta \leq \begin{cases} \frac{2}{5} & \text{for } d = 1, \\ \frac{3}{8} & \text{for } d = 2. \end{cases} \tag{3.56}$$

Scaling of the Wasserstein distance

In this paragraph, we will motivate the choice of the geometric exponent $\alpha = \frac{d}{d+1}$, see Theorem 4, in terms of scaling:

- From (3.54) we have
$$\Lambda^{-d} E \sim L^{-\frac{d}{d+1}}.$$
- From the definition (3.24) of the Wasserstein distance $\mathcal{W}$ we obtain the scaling
$$\begin{aligned} \Lambda^{-d} \mathcal{W}(h,3)^2 &\sim \Lambda^{-d} \iint |x-y|^2 \, d\pi(x,y) \\ &\sim \Lambda^{-d} \times L^2 \iint d\pi(x,y) \\ &\sim \Lambda^{-d} \times L^2 \times \int 3 \, dx \\ &\sim L^2, \end{aligned}$$
(see Figure 3.4), which implies
$$\Lambda^{-\frac{d}{2}} \mathcal{W}(h,3) \sim L. \tag{3.57}$$

Combining these two scaling relations leads to

$$\Lambda^{-d} E \left(\Lambda^{-\frac{d}{2}} \mathcal{W}(h,3) \right)^{\frac{d}{d+1}} \sim L^{-\frac{d}{d+1}} \times L^{\frac{d}{d+1}} \sim 1,$$

in accordance with Theorem 4.

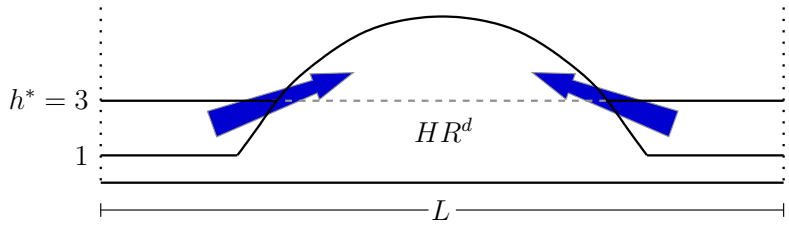

Figure 3.4: Scaling of $\mathcal{W}(h, 3)$.

Scaling of the number density

Another quantity that describes the coarseness of the configuration is the total number of droplets, denoted by N. It is related to the typical distance:

$$\Lambda^{-d} N \sim L^{-d}. \tag{3.58}$$

Hence, the scaling of L given in (3.55) translates into

$$N(t) \gtrsim t^{-\frac{d(d+1)}{3d+2}}. \tag{3.59}$$

Since N is a quantity to be easily measured in the numerics we will often refer to this scaling relation when we analyze the numerical data.

Review on Glasner and Witelski [15]

The coarsening dynamics for the thin-film equation on a one-dimensional substrate for the mobility exponent $q = 3$ was studied by Glasner and Witelski in [15].

The authors consider a configuration of equilibrium droplets as derived in Section 2.1, but their asymptotic regime differs from ours: Instead of choosing the precursor height of order 1 and droplets with large radii $R \gg 1$, they consider a precursor of height $\varepsilon \ll 1$ and droplet sizes of order 1. By means of asymptotic expansions and a Fredholm-type solvability argument, they derive a system of ODEs for the change of the droplet centers $\{X_i\}$ and pressures $\{P_i\}$ to describe the dynamics of interacting droplets. In Chapter 5, we will analogously derive a system of ODEs with a different approach.

In the regime $L \gg R$, they heuristically deduce a power-law behavior for the number of droplets as a function of time: $N(t) \sim t^{-\frac{2}{5}}$, see Equation (6.9) in [15]. This relation is confirmed by numerical simulations. As can be seen from (3.59), the result is in accordance with our bound on the coarsening rate. Indeed, their heuristics easily extend to the case of mobility exponent $q = 1$.

4 Dynamics of droplets

The dynamics of the thin-film equation relies on the competition between driving energy reduction and limiting viscous friction as formulated in the Rayleigh principle (1.24). Let us rephrase the structure in terms of the flux $J = hu$: At any time, J minimizes the Rayleigh functional

$$\mathcal{R}(J) = \tfrac{1}{2}D(J) + \dot{E}(h).J \,, \tag{4.1}$$

where $D(J) = \int \frac{1}{m}|J|^2 \, dx$ and $\dot{E}(h).J = \int \nabla \frac{\delta E}{\delta h}(h) \cdot J \, dx$. Then the film height evolves according to the continuity equation $\partial_t h + \nabla \cdot J = 0$. In the following, we utilize this concept to study model problems of the two relevant mechanisms for coarsening separately, namely Ostwald ripening by mass transfer and migration.

4.1 Ostwald ripening of droplets

Ostwald ripening relies on the mass exchange between droplets through the precursor layer. The large droplets grow at the expense of the smaller ones, see Figure 4.1, as mass is transported from high- to low-pressure regions.

4.1.1 The model problem: Two immobile droplets

We consider a mass-conservative configuration of two droplets with fixed centers X_1 and X_2, but time-dependent sizes. As a leading order approximation, we describe this configuration as a union of two mesoscopic droplets

$$h(t,x) = 1 + h_{V_1(t),X_1}(x) + h_{V_2(t),X_2}(x),$$

see (2.32a), with volumes $V_1 < V_2$. Let us denote $h_i := h_{V_i,X_i}$ for shortness. Note that we choose a parametrization in terms of the volumes (instead of radii), which is natural for the mass-conservative systems under consideration. A subsequent justification of the coarse-grained mesoscopic treatment of the configuration will be given in the following sense: The contribution of the detailed equilibrium profile of the droplets to the dissipation is to leading order negligible compared to the contribution of the precursor. In particular, the leading order scaling behavior is independent of the mobility exponent q, since $m(h) \approx 1$ in the precursor.

Now we characterize the volume change $\dot{V}_1 = -\dot{V}_2$ in this configuration by means of the Rayleigh principle: Both the flux J and $\dot{V}_1$ minimize as a couple the Rayleigh functional $\mathcal{R}$ subject to the continuity equation

$$\dot{V}_1 \left(\partial_{V_1} h_1 - \partial_{V_2} h_2\right) + \nabla \cdot J = 0$$

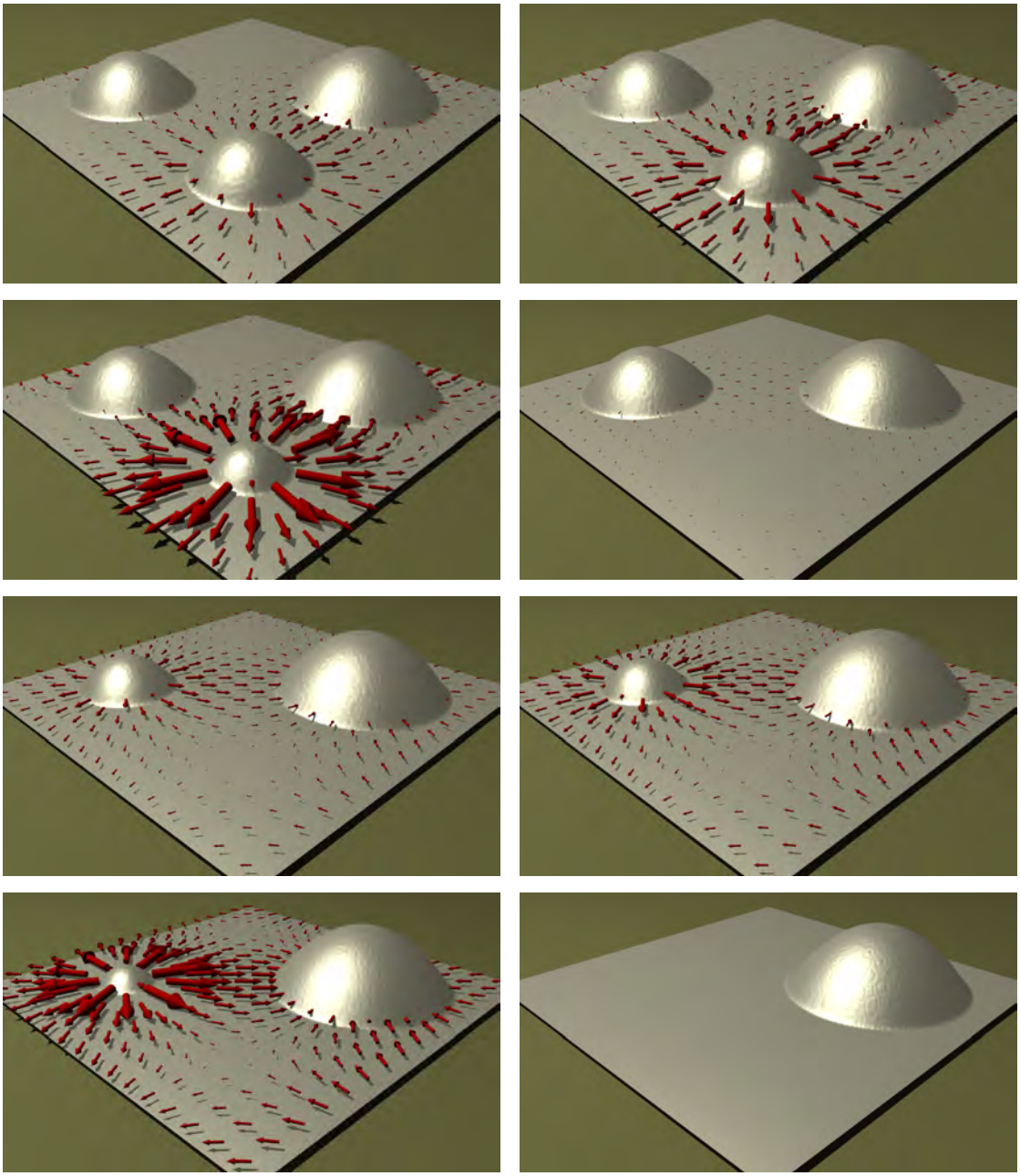

Figure 4.1: Ostwald ripening of a 3-droplet configuration on a periodic domain. The largest droplet (right) grows at the expense of the smaller ones. Here, the red arrows indicate the mass exchange through the precursor layer. Eventually, the single-droplet configuration is stable.

with boundary condition $J \cdot \nu \to 0$ as $|x| \to \infty$. A variation of (4.1) in J reveals that the flux is a gradient of a pressure: $J = -m\nabla\psi$.

To identify $\dot{V}_1$ from the Rayleigh functional, let us introduce a normalized model pressure, which generates the volume change $\dot{V}_1 = 1$: Let $\bar{\psi}$ be the solution of

$$(\partial_{V_1} h_1 - \partial_{V_2} h_2) - \nabla \cdot (m \nabla \bar{\psi}) = 0, \tag{4.2a}$$

$$J \cdot \nu \to 0 \quad \text{as} \quad |x| \to \infty, \quad \text{where} \quad J := -m\nabla\bar{\psi}. \tag{4.2b}$$

It immediately implies that $\psi = \dot{V}_1 \, \bar{\psi}$. Then the volume change is determined by

$$\dot{V}_1 = -\left(\int m |\nabla \bar{\psi}|^2 \, dx \right)^{-1} \int \frac{\delta E}{\delta h}(h) \left(\partial_{V_1} h_1 - \partial_{V_2} h_2 \right) \, dx. \tag{4.3}$$

Indeed, a minimization of the Rayleigh functional

$$\tfrac{1}{2} (\dot{V}_1)^2 \int m |\nabla \bar{\psi}|^2 \, dx + \dot{V}_1 \int \frac{\delta E}{\delta h}(h) \left(\partial_{V_1} h_1 - \partial_{V_2} h_2 \right) \, dx$$

w.r.t. the volume change $\dot{V}_1$ yields the characterization (4.3).

Corollary 2 (Sign of the volume change $\dot{V}_1$)**.** *In the case of $V_1 < V_2$, the volume V_1 decreases:*

$$\dot{V}_1 < 0.$$

Proof. The second integral in (4.3), which determines the sign of $\dot{V}_1$, can be derived explicitly with the help of (2.34):

$$\int \frac{\delta E}{\delta h}(h) \left(\partial_{V_1} h_1 - \partial_{V_2} h_2 \right) \, dx \overset{(2.1)}{=} P_1 - P_2 \overset{(2.34)}{=} \frac{2d}{\sqrt{2}\omega} \left(V_1^{-\frac{1}{d+1}} - V_2^{-\frac{1}{d+1}} \right) > 0$$

since $\int_{B_{R_i}(X_i)} \partial_{V_i} h_i \, dx = 1$ and $\partial_{V_i} h_i = 0$ in $\mathbb{R}^2 \backslash B_{R_i}(X_i)$. □

This result justifies the terminology *Ostwald ripening*.

4.1.2 Characterization of the volume change: The ripening factor

By approximating the *ripening factor* $\left(\int m |\nabla \bar{\psi}|^2 \, dx \right)^{-1}$ in (4.3) to leading order in the regime of well-separated droplets, that is $V_i \ll L$, we will characterize the volume change in terms of scaling in V_i and L. To be more precisely, we will show that

$$\dot{V}_1 = -\mathfrak{rip}(L, V_i) \left(V_1^{-\frac{1}{d+1}} - V_2^{-\frac{1}{d+1}} \right) \tag{4.4}$$

where the ripening factor is given to leading order by

$$\mathfrak{rip}(L, V_i) \approx \begin{cases} \frac{\sqrt{2}}{\omega} \, L^{-1} & \text{for } d = 1, \\ 4\pi^{\frac{4}{3}} \left(\log(L/V_1^{\frac{1}{3}}) + \log(L/V_2^{\frac{1}{3}}) \right)^{-1} & \text{for } d = 2. \end{cases} \tag{4.5}$$

One-dimensional case

In the one-dimensional case, elementary integration of the continuity equation $(\partial_{V_1} h_1 - \partial_{V_2} h_2) + \partial_x J = 0$ with no-flux boundary conditions $J(-\infty) = J(\infty) = 0$ yields

$$J(x) = \begin{cases} 0 & \text{in } (-\infty, X_1 - R_1], \\ -\frac{1}{6\sqrt{2}\omega} V_1^{-\frac{3}{2}} (x - X_1)^3 - \frac{1}{4\sqrt{2}\omega} V_1^{-\frac{1}{2}} (x - X_1) - \frac{1}{2} & \text{in } B_{R_1}(X_1), \\ -1 & \text{in } [X_1 + R_1, X_2 - R_2], \\ \frac{1}{6\sqrt{2}\omega} V_2^{-\frac{3}{2}} (x - X_2)^3 + \frac{1}{4\sqrt{2}\omega} V_2^{-\frac{1}{2}} (x - X_2) - \frac{1}{2} & \text{in } B_{R_2}(X_2), \\ 0 & \text{in } [X_2 + R_2, \infty). \end{cases}$$

Therefore, we obtain to leading order

$$\begin{aligned} \int m |\nabla \bar{\psi}|^2 \, dx &= \int \frac{1}{m} |J|^2 \, dx \\ &= \int_{B_{R_1}(X_1)} \frac{1}{m} |J|^2 \, dx + \underbrace{\int_{X_1 + R_1}^{X_2 - R_2} 1 \, dx}_{\approx L} + \int_{B_{R_2}(X_2)} \frac{1}{m} |J|^2 \, dx \\ &\approx L, \end{aligned}$$

since the two integrals over $B_{R_i}(X_i)$ scale like $V_i^{\frac{1}{2}} \ll L$. Hence, the main contribution stems from the precursor, and the volume change is to leading order characterized through

$$\dot{V}_1 \approx -L^{-1} \frac{\sqrt{2}}{\omega} \left(V_1^{-\frac{1}{2}} - V_2^{-\frac{1}{2}} \right)$$

in the regime $V_i^{\frac{1}{2}} \ll L$.

Two-dimensional case

For the treatment of the two-dimensional case, let us first introduce an auxiliary pressure relevant to the volume change of a single mesoscopic droplet $h = 1 + h_{V,0}$ centered in the origin. Let ψ_V be a radial symmetric solution of

$$-\partial_V h_{V,0} - \nabla \cdot (m \nabla \psi_V) = 0. \tag{4.6}$$

Since for $r = |x| > R$

$$1 = \int_{B_r(0)} \partial_V h_{V,0} \, dx = -\int_{\partial B_r(0)} m \nabla \psi_V \cdot \nu = -2\pi r (\partial_r \psi_V)$$

holds, we find that

$$\psi_V = -\frac{1}{2\pi} \log |x| + \text{const} \qquad \text{for } |x| > R. \tag{4.7}$$

We immediately obtain

$$\int_{B_L(0)\setminus B_R(0)} m|\nabla\psi_V|^2\,dx = \frac{1}{2\pi}\log(L/V^{\frac{1}{3}}) + \mathcal{O}(1). \tag{4.8}$$

The subsequent lemma shows that the leading order contribution of the mesoscopic droplet is of lower order, namely independent of $R \sim V^{\frac{1}{3}}$.

Lemma 10. *Let ψ_V be a solution of (4.6). Then*

$$\int_{B_R(0)} m|\nabla\psi_V|^2\,dx = \mathcal{O}(1). \tag{4.9}$$

Proof. Let $J_V := -m\nabla\psi_V$, which solves $\partial_V h_{V,0} + \nabla\cdot J_V = 0$. Now consider the rescaling $x = Ry$ and $\tilde{J}(y) := RJ_V(Ry)$. Then an easy calculation based on the mesoscopic droplet profile (2.32a) reveals that $\tilde{J}$ solves the problem $\partial_V h_{V,0}(y,V)\big|_{V=1} + \nabla\cdot\tilde{J} = 0$, which does not depend on V. This implies

$$\int_{B_R(0)} m|\nabla\psi_V|^2\,dx = \int_{B_R(0)} \frac{1}{m}|J_V|^2\,dx \le \int_{B_R(0)} |J_V|^2\,dx = \int_{B_1(0)} |\tilde{J}|^2\,dy,$$

which proves the assertion. □

Now we can determine the leading order behavior of the ripening factor in the two-dimensional case.

Proposition 5. *In the regime of well-separated droplets, that is $V^{\frac{1}{3}} \ll L$, we have the leading order behavior*

$$\int m|\nabla\bar{\psi}|^2\,dx \approx \frac{1}{2\pi}\left(\log(L/V_1^{\frac{1}{3}}) + \log(L/V_2^{\frac{1}{3}})\right). \tag{4.10}$$

In particular, the leading order behavior does not depend on the mobility exponent.

Proof. First note that there are two variational representations of $\int m|\nabla\bar{\psi}|^2\,dx$:

$$\int m|\nabla\bar{\psi}|^2\,dx = \max_{\zeta}\left\{\int \left(-m|\nabla\zeta|^2 - 2\left(\partial_{V_1}h_1 - \partial_{V_2}h_2\right)\zeta\right)\,dx\right\} \tag{4.11}$$

$$= \min_{J}\left\{\int \frac{1}{m}|J|^2\,dx \;\Big|\; (\partial_{V_1}h_1 - \partial_{V_2}h_2) + \nabla\cdot J = 0\right\}. \tag{4.12}$$

In the following, we apply this representation to provide lower and upper bounds on $\int m|\nabla\bar{\psi}|^2\,dx$ that differ only by an amount of $\mathcal{O}(1)$.

Lower bound: Let $\ell := L/3$. To construct a suitable test function we define

$$\zeta_i(x) := \begin{cases} (-1)^i\frac{1}{2\pi}\log(R_i/\ell) & \text{in } B_{R_i}(X_i),\\ (-1)^i\frac{1}{2\pi}\log(|x-X_i|/\ell) & \text{in } B_\ell(X_i)\setminus B_{R_i}(X_i),\\ 0 & \text{in } \mathbb{R}^2\setminus B_\ell(X_i),\end{cases}$$

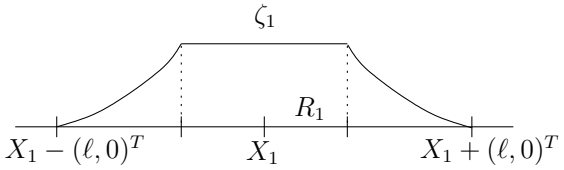

Figure 4.2: The test function ζ_1 carries mass 1 outside the droplet.

for $i = 1, 2$, see Figure 4.2. The test functions ζ_i are harmonic functions such that the mass flux $-\nabla\zeta_i$ across $\partial B_{R_i}(X_i)$ is equal to ± 1:

$$\int_{\partial B_{R_i}(X_i)} \mp \nabla\zeta_i \cdot \nu \, dx = \pm 1.$$

Now consider the test function $\zeta = \sum \lambda_i \zeta_i$, where the constants λ_1 and λ_2 need to be determined. We compute

$$\int \left(-m|\nabla\zeta|^2 + 2\left(\partial_{V_1} h_1 - \partial_{V_2} h_2\right)\zeta\right) \, dx = \frac{1}{2\pi} \sum_{i=1}^{2} \log(\ell/R_i)(-\lambda_i^2 - 2\lambda_i).$$

Maximizing in λ_i gives $\lambda_i = -1$. Therefore, we obtain the lower bound

$$\int m|\nabla\bar{\psi}|^2 \, dx \geq \frac{1}{2\pi} \sum_{i=1}^{2} \log(\ell/R_i) = \frac{1}{2\pi} \sum_{i=1}^{2} \log(L/V_i^{\frac{1}{3}}) + \mathcal{O}(1).$$

Upper bound: Let $\overline{X} = (X_1 + X_2)/2$ and $\overline{\Omega} = B_L(\overline{X}) \backslash (B_\ell(X_1) \cup B_\ell(X_2))$. We construct the test flux J with the help of the auxiliary pressure defined in (4.6):

$$J(x) = \begin{cases} +J_1(x - X_1) & \text{in } B_\ell(X_1), \\ -J_2(x - X_2) & \text{in } B_\ell(X_2), \\ J_{out} & \text{in } \overline{\Omega}, \\ 0 & \text{in } \mathbb{R}^2 \backslash B_L(\overline{X}), \end{cases} \tag{4.13}$$

where $J_i := -m\nabla\psi_{V_i}$, $i = 1, 2$, is defined by (4.6), and $J_{out} := -\nabla\psi_{out}$ with

$$\begin{aligned} -\Delta\psi_{out} &= 0 && \text{in } \overline{\Omega}, \\ \nabla\psi_{out} \cdot \nu &= \begin{cases} -\frac{1}{2\pi\ell} & \text{on } \partial B_\ell(X_i),\ i = 1, 2, \\ 0 & \text{on } \partial B_L(\overline{X}). \end{cases} \end{aligned}$$

Here, the boundary conditions are chosen such that $J_i \cdot \nu = J_{out} \cdot \nu$ at $\partial B_\ell(X_i)$, which makes J an admissible test function in the sense that the divergence of J is defined distributionally.

As above, a simple scaling argument (based on scaling of the domain and change of variables) reveals that the dissipation integral in $\overline{\Omega}$ has scaling $\mathcal{O}(1)$: Indeed,

$$\int_{\overline{\Omega}} \frac{1}{m} |J_{out}|^2 \, dx = \int_{\overline{\Omega}} |\nabla \psi_{out}|^2 \, dx \leq C$$

for some constant $C = \mathcal{O}(1)$. Combining this bound with (4.8) and (4.9) yields the desired upper bound, which differs from the lower bound only by an amount of $\mathcal{O}(1)$. □

4.2 Migration of droplets

4.2.1 The model problem: Isolated droplet in a flux field

We consider a single equilibrium droplet $\widetilde{h} = \widetilde{h}(x - X(t))$ with fixed mass centered at $X = X(t)$ in a surrounding constant flux field J_∞, see Figure 4.3. We expect the droplet to migrate with speed $\dot{X}$ to minimize the dissipation under the flux boundary condition. Let us write $r := |x - X|$ and $\nu := (x - X)/r$ for shortness.

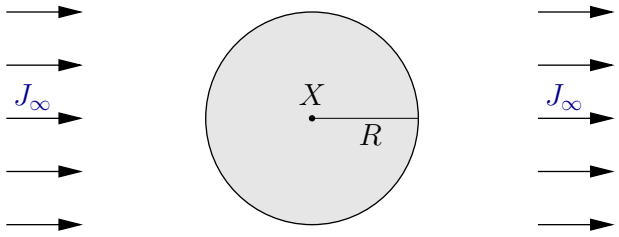

Figure 4.3: An equilibrium droplet in an ambient constant flux field J_∞.

To characterize the response $\dot{X}$ of the droplet, we apply the Rayleigh principle (4.1): The flux J and the migration velocity $\dot{X}$ minimize as a couple the dissipation rate

$$\tfrac{1}{2} D(J) = \tfrac{1}{2} \int \frac{1}{m} |J|^2 \, dx \tag{4.14}$$

subject to the continuity equation

$$-\dot{X} \cdot \nabla \widetilde{h} + \nabla \cdot J = 0 \tag{4.15}$$

with boundary condition

$$J \cdot \nu \to J_\infty \cdot \nu \quad \text{as} \quad r \to \infty. \tag{4.16}$$

Note that the energy is translation-invariant, which implies $\dot{E} = 0$ in this case.

Let us now argue that the flux J and the migration speed $\dot{X}$ are characterized by the following second-order elliptic problem for a pressure ψ with flux boundary conditions

and an additional solvability condition:

$$-\dot{X}\cdot\nabla\widetilde{h}-\nabla\cdot(m\nabla\psi) = 0, \tag{4.17a}$$

$$J\cdot\nu\to J_\infty\cdot\nu \quad \text{as } r\to\infty, \qquad \text{where } J:=-m\nabla\psi, \tag{4.17b}$$

$$\int\nabla\widetilde{h}\,\psi\,dx = 0. \tag{4.17c}$$

The solvability condition (4.17c) allows us to extract a characterization of the migration speed $\dot{X}$.

First, the variation of (4.14) in J reveals that the minimizing flux is L^2-orthogonal to all divergence-free test fluxes, so that it is a gradient of a pressure ψ:

$$J=-m\nabla\psi. \tag{4.18}$$

This implies (4.17a) from (4.15).

Furthermore, the continuity equation (4.15) induces

$$\nabla\cdot(-\dot{X}(\widetilde{h}-h_\infty)+J)=0.$$

Hence, the variation of (4.14) w.r.t. $\dot{X}$ yields

$$0=\int\frac{1}{m}(\widetilde{h}-h_\infty)\,J\,dx=-\int(\widetilde{h}-h_\infty)\nabla\psi\,dx=\int\nabla\widetilde{h}\,\psi\,dx \tag{4.19}$$

for a minimizing flux.

4.2.2 Characterization of the droplet velocity: The migration factor

In the following, we utilize (4.17) to characterize the migration speed.

One-dimensional case

In the one-dimensional case, the continuity equation (4.17a) together with the boundary condition (4.17b) can be integrated explicitly. We obtain the solution $J=J_\infty+\dot{X}(\widetilde{h}-h_\infty)$, so that (4.17c) yields

$$\begin{aligned}0 &= \int\nabla\widetilde{h}\,\psi\,dx=\int\frac{1}{m}(\widetilde{h}-h_\infty)\,J\,dx\\ &= J_\infty\int\frac{1}{m}(\widetilde{h}-h_\infty)\,dx+\dot{X}\int\frac{1}{m}(\widetilde{h}-h_\infty)^2\,dx.\end{aligned}$$

Then the migration velocity is characterized by

$$\dot{X}=-\frac{\int\frac{1}{m}(\widetilde{h}-h_\infty)\,dx}{\int\frac{1}{m}(\widetilde{h}-h_\infty)^2\,dx}\,J_\infty. \tag{4.20}$$

We call the integral expression on the left hand side the *migration factor*

$$\mathfrak{mig} = \frac{\int \frac{1}{m}(\widetilde{h} - h_\infty)\, dx}{\int \frac{1}{m}(\widetilde{h} - h_\infty)^2\, dx},$$

which to leading order depends on the droplet radius R: $\mathfrak{mig} \approx \mathfrak{mig}(R)$. The result (4.20) is in accordance with the equation of migration derived by Glasner and Witelski, see (4.10) in [15].

Corollary 3 (Sign of migration velocity in 1-d)**.** *The droplet moves in the direction opposite to J_∞:*

$$\frac{\dot{X}}{J_\infty} = -\mathfrak{mig} < 0.$$

It follows easily from property (2.3) of the stationary droplet profile $\widetilde{h}$.

Proposition 6 (Leading order behavior of the migration factor in 1-d)**.** *In the regime of large droplets, that is $R \gg 1$, we have to leading order*

$$\int \frac{1}{m}(\widetilde{h} - h_\infty)\, dx \;\approx\; \begin{cases} C\, R^{2-q} & \text{for } q \in [0,2), \\ \sqrt{2}\, \log R & \text{for } q = 2, \\ C & \text{for } q > 2, \end{cases} \tag{4.21}$$

$$\int \frac{1}{m}(\widetilde{h} - h_\infty)^2\, dx \;\approx\; \begin{cases} C\, R^{3-q} & \text{for } q \in [0,3), \\ \sqrt{2}\, \log R & \text{for } q = 3, \\ C & \text{for } q > 3, \end{cases} \tag{4.22}$$

where $C > 0$ denotes a generic constant independent of R (but depending on q). Consequently, the migration factor has the following leading order behavior:

$$\mathfrak{mig}(R) \;=\; -\frac{\dot{X}}{J_\infty} \;\approx\; \begin{cases} CR^{-1} & \text{for } q \in [0,2), \\ CR^{-1} \log R & \text{for } q = 2, \\ CR^{q-3} & \text{for } q \in (2,3), \\ C(\log R)^{-1} & \text{for } q = 3, \\ C & \text{for } q > 3. \end{cases} \tag{4.23}$$

Proof. To investigate integrals of the form

$$I_\gamma := \int \frac{1}{m}(\widetilde{h} - h_\infty)^\gamma\, dx = \int \frac{(\widetilde{h} - h_\infty)^\gamma}{\widetilde{h}^q}\, dx,$$

we invoke the first integral of $-\partial_x^2 \widetilde{h} + \mathcal{U}'(\widetilde{h}) = P$, that is,

$$-\tfrac{1}{2}(\partial_x \widetilde{h})^2 + \widetilde{\mathcal{U}}(\widetilde{h}) = 0, \tag{4.24}$$

where $\widetilde{\mathcal{U}}$ is defined in (2.12). Because of the properties (2.3) of the equilibrium droplet, (4.24) turns into

$$\partial_x \widetilde{h} \;=\; -\sqrt{2\widetilde{\mathcal{U}}(\widetilde{h})} \quad \text{for } x > 0,$$

so that

$$I_\gamma \;=\; 2\int_{h_\infty}^{\widetilde{h}(0)} \frac{(h-h_\infty)^\gamma}{h^q}\,\frac{1}{\sqrt{2\widetilde{\mathcal{U}}(h)}}\,dh. \tag{4.25}$$

We recall from (2.4) that $h_\infty \approx 1$ for $P \sim R^{-1} \ll 1$, so that (4.25) turns to leading order into

$$\begin{aligned} I_\gamma \quad &\approx \quad 2\int_1^{\widetilde{h}(0)} \frac{(h-1)^\gamma}{h^q}\,\frac{1}{\sqrt{2\mathcal{U}(h)}}\,dh \\ &\overset{(2.24)}{=} \quad 2\int_1^{1+R/\sqrt{2}} \frac{(h-1)^\gamma}{h^q}\,\frac{1}{\sqrt{2\mathcal{U}(h)}}\,dh. \end{aligned} \tag{4.26}$$

Due to $\gamma > 0$ and $\sqrt{2\mathcal{U}(h)} \overset{(1.7)}{\sim} (h-1)$ at $h = 1$, the (potential) singularity at $h = 1$ is integrable.

For $q > \gamma + 1$, (4.26) is also integrable as $h \to \infty$, so that I_γ is to leading order independent of R:

$$I_\gamma \;\approx\; 2\int_1^{\infty} \frac{(h-1)^\gamma}{h^q}\,\frac{1}{\sqrt{2\mathcal{U}(h)}}\,dh \;\in\; (0,\infty).$$

Note that the leading order scaling of I_γ depends on the details of the potential $\mathcal{U}$.

On the other hand, for $q = \gamma + 1$, we have a logarithmic divergence

$$I_\gamma \;\approx\; \sqrt{2}\,\log R,$$

and for $q < \gamma + 1$, the divergence

$$I_\gamma \;\approx\; CR^{\gamma-q+1},$$

which concludes the proof. □

Remark.

- The proof reveals that there is a cross-over at $q = \gamma + 1$: For $q < \gamma + 1$, the contribution of the cap region dominates the scaling behavior of I_γ, while for $q > \gamma + 1$, the contribution of the foot region dominates (since the upper bound of the integral, i.e. $1 + R/\sqrt{2}$, could be replaced by ∞).
- Consequently, the migration factor, that is $-I_1/I_2$, has two cross-overs: at $q = 2$ and $q = 3$. For $q < 2$, the migration factor is dominated by contributions of the cap region, and for $q > 3$ by contributions of the foot region. We have already discussed this in the introduction of this thesis.

Two-dimensional case

We will again deduce the migration factor from the solvability condition and furthermore show in the regime of large droplets that it has the same scaling behavior as in one dimension.

A straightforward explicit integration as in the one-dimensional case does not apply. Instead of that, we reformulate the model problem (4.17) in terms of two auxiliary problems for pressures:

1. the pressure ψ_0 that stems from a normalized flux boundary condition at infinity:

$$-\nabla \cdot (m\nabla\psi_0) = 0 \tag{4.27a}$$

$$J_0 \cdot \nu \to \binom{1}{0} \cdot \nu \quad \text{as} \quad r \to \infty, \quad \text{where} \quad J_0 := m\nabla\psi_0. \tag{4.27b}$$

2. the pressure ψ_1 that makes the droplet move in x_1-direction with unit speed:

$$-\partial_1 \widetilde{h} - \nabla \cdot (m\nabla\psi_1) = 0 \tag{4.28a}$$

$$J_1 \cdot \nu \to 0 \quad \text{as} \quad r \to \infty, \quad \text{where} \quad J_1 := -m\nabla\psi_1. \tag{4.28b}$$

These auxiliary pressures allow us to decompose ψ:

$$\psi = -J_\infty \psi_0 + \dot{X}\psi_1. \tag{4.29}$$

Note that we identify the vectors J_∞ and $\dot{X}$ with the scalar quantities in $\binom{J_\infty}{0}$ and $\binom{\dot{X}}{0}$ (referring to isotropy). Hence, with the help of condition (4.17c), the migration speed is characterized through

$$\dot{X} = -\mathfrak{mig}\, J_\infty, \tag{4.30}$$

where we define the migration factor $\mathfrak{mig}$ by

$$\mathfrak{mig} = -\frac{\int \psi_0 \partial_1 \widetilde{h}\, dx}{\int \psi_1 \partial_1 \widetilde{h}\, dx},$$

whose leading order behavior will be identified in terms of the radius R.

To investigate the migration factor, let us first study the asymptotic behavior of the auxiliary pressures. For this purpose, it is convenient (since $\widetilde{h}$ only depends on $|x - X|$) to introduce polar coordinates (r, θ) by

$$r = |x - X| \quad \text{and} \quad \cos\theta = \frac{x - X}{|x - X|} \cdot \frac{\dot{X}}{|\dot{X}|}, \tag{4.31}$$

such that

$$x - X = r\begin{pmatrix}\cos\theta\\ \sin\theta\end{pmatrix}.$$

In particular for the auxiliary problems, we have

$$r\cos\theta = (x - X)\cdot\begin{pmatrix}1\\ 0\end{pmatrix}.$$

A Fourier series Ansatz in the angle variable θ for (4.27) and (4.28) reveals that both ψ_0 and ψ_1 are of the form

$$\begin{aligned}\psi_0(x) &= \psi_0(r)\cos\theta,\\ \psi_1(x) &= \psi_1(r)\cos\theta,\end{aligned} \tag{4.32}$$

i.e. the first mode is the only non-vanishing mode, where the radial functions are determined by

$$-\partial_r(m\partial_r\psi_0) - \frac{m}{r}\partial_r\psi_0 + \frac{m}{r^2}\psi_0 = 0, \tag{4.33a}$$

$$\psi_0(0) = 0, \qquad \lim_{r\to\infty}\partial_r\psi_0(r) = 1, \tag{4.33b}$$

and

$$-\partial_r(\widetilde{h} - h_\infty) - \partial_r(m\partial_r\psi_1) - \frac{m}{r}\partial_r\psi_1 + \frac{m}{r^2}\psi_1 = 0, \tag{4.34a}$$

$$\psi_1(0) = 0, \qquad \lim_{r\to\infty}\partial_r\psi_1(r) = 0, \tag{4.34b}$$

respectively. For convenience, we again use the same notation for $\psi_0(x)$ and $\psi_0(r)$. It will be clear from the context to which we refer. Since $\widetilde{h}$ only depends on r, the mobility m can also be understood as a function of r.

Lemma 11 (Asymptotic behavior of auxiliary pressures)**.** *The auxiliary pressures have the following asymptotic properties to leading order:*

1. $$\left.\begin{aligned}\psi_0(r) &= r + \tfrac{const}{r}\\ \psi_1(r) &= \tfrac{const}{r}\end{aligned}\right\} \quad \textit{for} \quad r - R \gg 1. \tag{4.35}$$

2. $$\lim_{r\to\infty} r\psi_1(r) = \frac{1}{2\pi}\int \psi_0(x)\partial_1\widetilde{h}(x)\,dx = \frac{1}{2}\int_0^\infty \psi_0(r)\partial_r\widetilde{h}(r)\,dr. \tag{4.36}$$

Therefore, the constant for ψ_1 in (4.35) *is determined by* (4.36)*.*

Figures 4.4 and 4.5 show typical shapes of the auxiliary pressures for the mobility exponent $q = 2$ derived numerically.

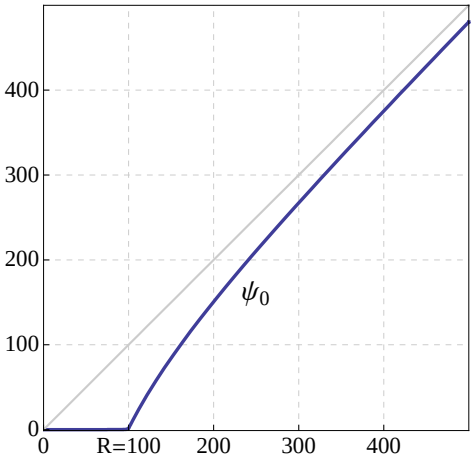

Figure 4.4: Typical profile of ψ_0 for a mesoscopic droplet profile with radius $R = 100$ and mobility exponent $q = 2$, which asymptotically behaves like $r + \frac{\text{const}}{r}$ as $r \to \infty$.

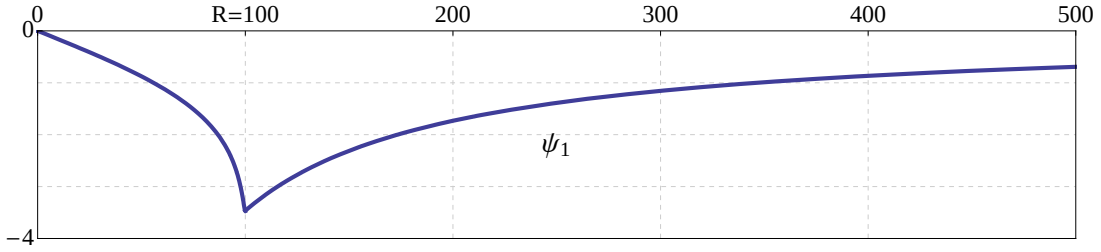

Figure 4.5: Typical profile of ψ_1 for a mesoscopic droplet profile with radius $R = 100$ and mobility exponent $q = 2$, which asymptotically behaves like $\frac{\text{const}}{r}$ as $r \to \infty$.

Proof. Let us recall that $\widetilde{h}$ is to leading order constant in the precursor region:

$$\widetilde{h} \approx h_\infty \qquad \text{for} \quad r - R \gg 1.$$

Therefore, we obtain in particular

$$m \approx \text{const} \qquad \text{for} \quad r - R \gg 1.$$

Hence, (4.33) and (4.34) simplify in the precursor film region such that $\{r, r^{-1}\}$ is a fundamental system. We infer from the boundary conditions (4.33b) and (4.34b) that (4.35) are indeed solutions in the precursor film region.

Regarding the proof of the second claim, we use Green's formula on a ball $B_r(0)$ for a

sufficiently large r:

$$\begin{aligned}&\int_{B_r(0)} \nabla\cdot(m\nabla\psi_1)\;\psi_0\;dx - \int_{B_r(0)} \psi_1\;\nabla\cdot(m\nabla\psi_0)\;dx\\ &= \int_{\partial B_r(0)} \psi_0\; m\;\nabla\psi_1\cdot\frac{x-X}{|x-X|}\;dx - \int_{\partial B_r(0)} \psi_1\; m\;\nabla\psi_0\cdot\frac{x-X}{|x-X|}\;dx.\end{aligned}$$

Now we examine the four integral terms:

1. $$\int_{B_r(0)} \nabla\cdot(m\nabla\psi_1)\;\psi_0\;dx \overset{(4.28a)}{=} -\int_{B_r(0)} \partial_1\widetilde{h}\;\psi_0\;dx.$$

2. $$\int_{B_r(0)} \psi_1\;\nabla\cdot(m\nabla\psi_0)\;dx \overset{(4.27a)}{=} 0.$$

3. $$\begin{aligned}&\int_{\partial B_r(0)} m\,(\psi_0\;\nabla\psi_1 - \psi_1\;\nabla\psi_0)\cdot\frac{x-X}{|x-X|}\;dx\\ \overset{(4.32)}{=}\;& \int_0^{2\pi} m\,(\psi_0(r)\partial_r\psi_1(r) - \psi_1(r)\partial_r\psi_0(r))\cos^2\theta\, r\;d\theta\\ =\;& \pi\; m(r)\,[\psi_0(r)\partial_r\psi_1(r) - \psi_1(r)\partial_r\psi_0(r)]\,r\\ \overset{(4.35)}{\approx}\;& \pi\,[-\psi_1(r) - \psi_1(r)]\,r = -2\pi r\psi_1(r).\end{aligned}$$

   Note that the last line follows in particular from the asymptotic behavior $\partial_r\psi_1(r) \approx -\frac{1}{r}\psi_1(r)$ due to (4.34a).

The combination of these expressions yields assertion (4.36). □

The asymptotic behavior justifies the integration by parts of the denominator of the migration factor in (4.30):

$$\int \psi_1\partial_1\widetilde{h}\;dx = \int \psi_1\,\partial_1(\widetilde{h} - h_\infty)\;dx = -\int \psi_1\nabla\cdot(m\nabla\psi_1)\;dx = \int m|\nabla\psi_1|^2\;dx$$

but clarifies that the numerator has to be kept as is:

$$\dot{X} = \frac{\int \psi_0\partial_1\widetilde{h}\;dx}{\int m|\nabla\psi_1|^2\;dx}\,J_\infty, \tag{4.37}$$

or in polar coordinates

$$\dot{X} = \frac{\int_0^\infty \psi_0\,\partial_r\widetilde{h}\,r\;dr}{\int_0^\infty m((\partial_r\psi_1)^2 + r^{-2}(\psi_1)^2)\,r\;dr}\,J_\infty. \tag{4.38}$$

Not surprisingly, we obtain a result analogous to the one-dimensional case:

Corollary 4 (Sign of migration velocity in 2-*d*)**.** *The droplet moves in the direction opposite to* J_∞*:*

$$\frac{\int_0^\infty \psi_0\, \partial_r \widetilde{h}\, r\, dr}{\int_0^\infty m((\partial_r \psi_1)^2 + r^{-2}(\psi_1)^2)\, r\, dr} = -\mathfrak{mig} < 0.$$

The result is intuitively clear as we pointed out in the introduction of this thesis: If one thinks of a prescribed flux from west to east, i.e. $J_\infty > 0$, the droplet is gaining mass at the western side and loosing mass at the eastern side, so that its center is moving westwards, see Figure 4.6.

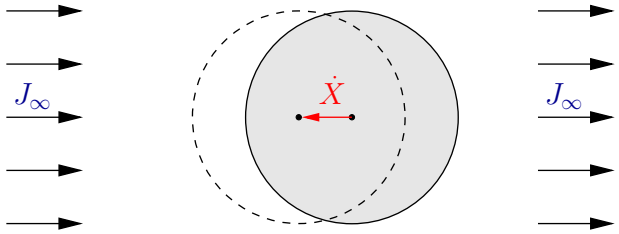

Figure 4.6: The equilibrium droplet migrates in the opposite direction to J_∞.

Proof. The denominator has obviously positive sign. Therefore, it suffices to show that $\int_0^\infty \psi_0\, \partial_r \widetilde{h}\, r\, dr < 0$. We have already shown in (2.3) that $\partial_r \widetilde{h} < 0$ for $r > 0$. Hence, we will now argue that

$$\psi_0(r) > 0 \quad \text{for} \quad r > 0. \tag{4.39}$$

Note that $\psi_0(0) = 0$ by definition and $\psi_0 > 0$ for sufficiently large r according to (4.35). Hence, the one-dimensional maximum principle for the second-order elliptic operator $-\partial_r(m\partial_r) - \frac{m}{r}\partial_r + \frac{m}{r^2}$ yields $\psi_0(r) \geq 0$ for $r \geq 0$. Now assume that $\psi_0(r_0) = 0$ for an interior point $r_0 > 0$. However, according to the strong maximum principle [35], this would yield $\psi_0 \equiv 0$ in contradiction to its asymptotic behavior (4.35). □

In the regime $R \gg 1$, the migration factor in the two-dimensional case has the same scaling behavior as in the one-dimensional case:

Proposition 7 (Leading order behavior of the migration factor in 2-*d*)**.** *In the regime* $R \gg 1$*, we have the leading order behavior*

$$\begin{aligned} \mathcal{I}_{\psi_0} := -\int \psi_0 \partial_1 \widetilde{h}\, dx &= -\pi \int_0^\infty \psi_0 \partial_r \widetilde{h} r\, dr \\ &\approx \begin{cases} \frac{\sqrt{2}\pi}{4}\, R^3 & \text{for } q = 0, \\ C_0(q)\, R^{3-q} & \text{for } q \in (0,2), \\ \sqrt{2}\pi\, R \log R & \text{for } q = 2, \\ C_0(q)\, R & \text{for } q > 2, \end{cases} \end{aligned} \tag{4.40}$$

$$\mathcal{I}_{\psi_1} := \int m|\nabla\psi_1|^2\,dx \;=\; \pi\int_0^\infty m((\partial_r\psi_1)^2 + r^{-2}(\psi_1)^2)r\,dr$$
$$\approx \begin{cases} \frac{\pi}{12}\,R^4 & \text{for } q=0,\\ C_1(q)\,R^{4-q} & \text{for } q\in(0,3),\\ \frac{\pi}{\sqrt{2}}\,R\log R & \text{for } q=3,\\ C_1(q)\,R & \text{for } q>3, \end{cases} \tag{4.41}$$

where the constants $C_0(q)$ and $C_1(q)$ are independent of R. Consequently, the migration factor has the following leading order behavior:

$$\mathfrak{mig}(R) \;=\; -\frac{\dot X}{J_\infty} \;\approx\; \begin{cases} C\,R^{-1} & \text{for } q\in[0,2),\\ C\,(\log R)\,R^{-1} & \text{for } q=2,\\ C\,R^{q-3} & \text{for } q\in(2,3),\\ C\,(\log R)^{-1} & \text{for } q=3,\\ C & \text{for } q>3. \end{cases} \tag{4.42}$$

Remark. In terms of scaling, the migration factors in the one- and two-dimensional case coincide. Furthermore, we observe the following:

- Again, we find a crossover at $q=2$ in (4.40) and at $q=3$ in (4.41), respectively, as in the one-dimensional case. As the proof reveals, this is due to the fact that for $0<q<2$ and $0<q<3$, respectively, the leading order scaling contribution comes from the cap region of the droplet, whereas for $q\geq 2$ and $q\geq 3$, respectively, the foot region gives leading order contributions.
- The migration factor in (4.42) reveals that the response of a large droplet on the ambient flux J_∞ is slower than that of smaller ones in terms of scaling. However, the stronger the growth rate of m as parametrized by the exponent q is, the less pronounced is this effect. Eventually for $q>3$, there is no dependence on R at all to leading order. In the introduction, we already explained the intuition behind it.

Remark (Constants $C_0(q)$ and $C_1(q)$). For numerical tests the explicit knowledge of the numerical constants depending on q is necessary. However, we are not able to determine all the constants by means of the asymptotic analysis:

- $C_0(q)$ for $q\in(0,2)$: The main contribution to the integral comes from the cap region. However, as the asymptotic analysis reveals, the cap profile of ψ_0 cannot be matched quantitatively to the foot region, see Table 4.1, so that the constant remains undetermined in this case.
- $C_0(q)$ for $q>2$: The explicit form depends on details of the potential $\mathcal{U}$, since the main contribution comes from the foot region. Nevertheless, we appeal to the mesoscopic profile and therefore expect an error of order one in the constants.

- $C_1(q)$ for $q \in (0,3)$: This constant is determined by a variational problem, see (4.60). We will solve it numerically to obtain the constants.
- $C_1(q)$ for $q > 3$: The explicit form depends on details of the potential $\mathcal{U}$, see (4.64).

Nevertheless, we can derive the integrals $\mathcal{I}_{\psi_0}$ and $\mathcal{I}_{\psi_1}$ explicitly by solving the equations for ψ_0 and ψ_1 numerically, so that we can check the convergence of our asymptotic analysis in terms of the radius R. Figure 4.7 and 4.8 show these convergence tests based on numerical solutions derived with *Mathematica* [39]. Note that we used the mesoscopic droplet profile for the numerics. Nevertheless, one striking insight, which should be kept in mind at least for the numerical tests, is that relatively large droplets are needed to reach the asymptotic state.

The proof of the scaling relations in Proposition 7 is given in the following two sections, which present asymptotic analysis of the two auxiliary pressures.

4.2.3 Asymptotic analysis of ψ_0

We have to get an understanding of the auxiliary pressure ψ_0 of (4.27), or (4.33), respectively, itself. Let us clearly state that we do not find universal functions $C_q(R)$ and $\hat{\psi}_0(\frac{r}{R})$ such that $\psi_0(r) = C_q(R)\hat{\psi}_0(\frac{r}{R})$ on the whole domain. Depending on the mobility exponent q, we derive asymptotic expressions for ψ_0 separately in the precursor, foot and cap region, which unfortunately cannot be merged quantitatively by matching in general. For our analysis, we will refer to the leading order droplet profile (2.24), where we identified the three different regions. Consequently, some constants will depend on the details of $\mathcal{U}$, provided the main scaling contribution comes from the foot region.

As a warm-up, let us first study ψ_0 in the easiest case of $q = 0$, that is $m \equiv 1$. Then equation (4.33a) turns into

$$-\partial_r^2\psi_0 - r^{-1}\partial_r\psi_0 + r^{-2}\psi_0 = 0$$

with the boundary condition

$$\psi_0(0) = 0, \qquad \lim_{r\to\infty} \partial_r\psi_0(r) = 1.$$

The solution is

$$\psi_0(r) = r,$$

so that we get for the leading order profile (2.24)

$$-\pi \int_0^\infty \psi_0\, \partial_r \widetilde{h}\, r\, dr \approx \frac{\sqrt{2}\pi}{R} \int_0^R r^3\, dr = \frac{\sqrt{2}\pi}{4} R^3,$$

which is the claimed scaling in (4.40).

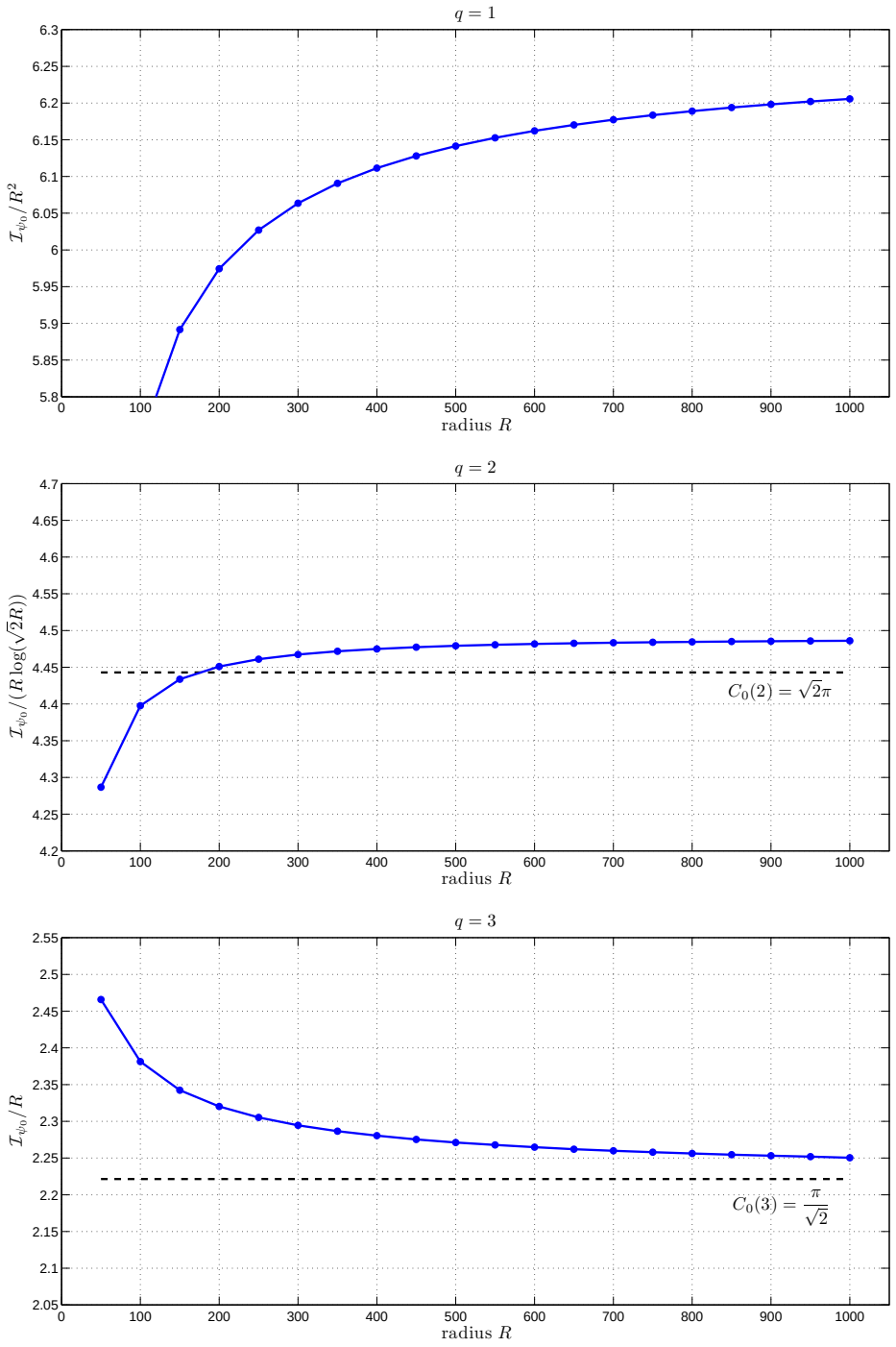

Figure 4.7: Convergence of $\mathcal{I}_{\psi_0}$ to the leading order expressions in (4.40) for mobility exponents $q = 1, 2, 3$ (from top to bottom).

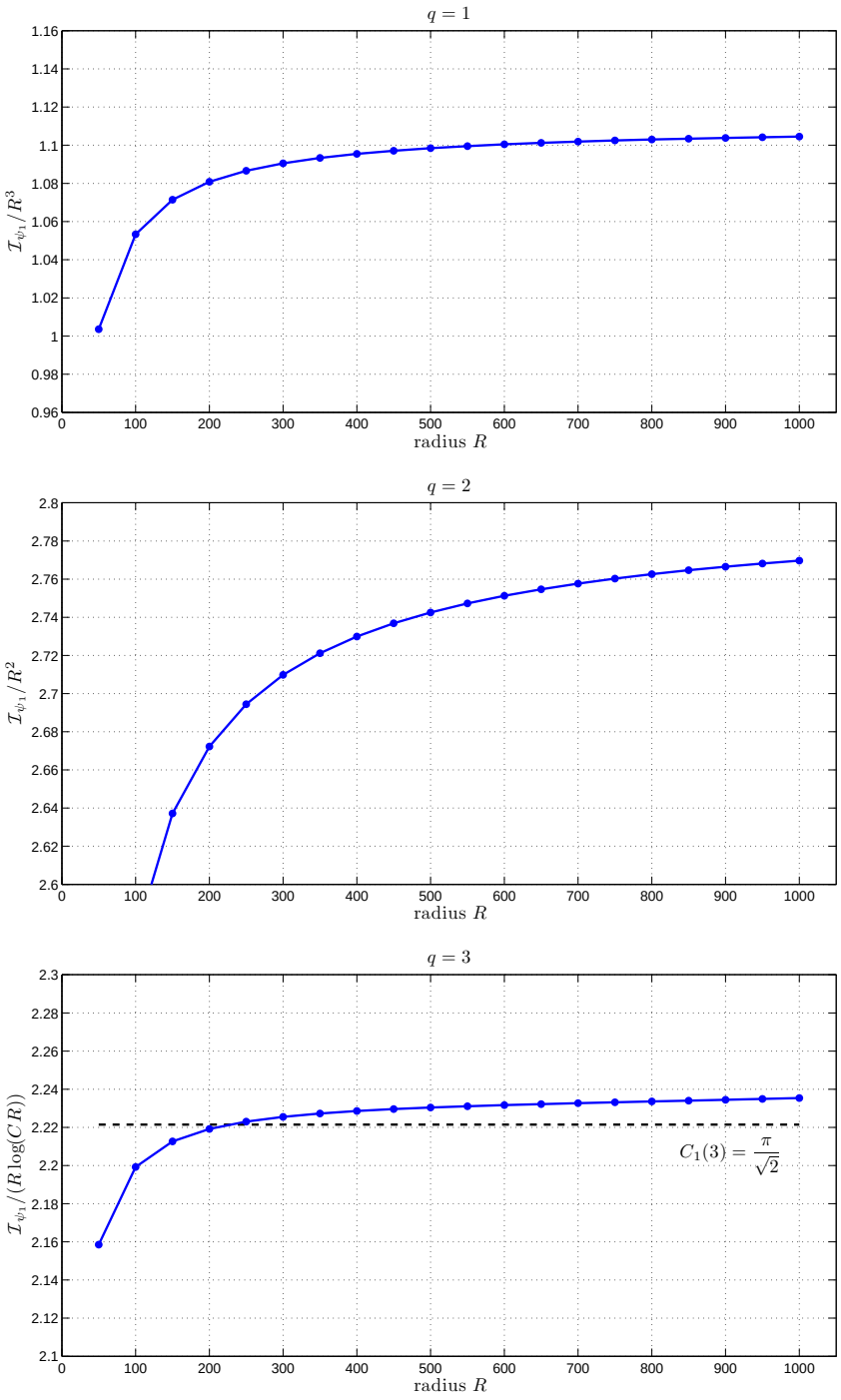

Figure 4.8: Convergence of $\mathcal{I}_{\psi_1}$ to the leading order expressions in (4.41) for mobility exponents $q = 1, 2, 3$ (from top to bottom).

The reduced order equation

For the general case $q > 0$, an order reduction of the second-order equation (4.33) helps to understand the radial solution ψ_0. For this purpose we rewrite the equation for $r \in (0, \infty)$:

$$-\frac{r^2}{\psi_0}\partial_r^2\psi_0 - \left(q\partial_r(\log\widetilde{h}) + \frac{1}{r}\right)\frac{r^2}{\psi_0}\partial_r\psi_0 + 1 = 0. \tag{4.43}$$

Note that

$$\lim_{r\to 0}\frac{r}{\psi_0}\partial_r\psi_0 = 1, \tag{4.44}$$

where we use l'Hospital's rule together with the fact that $\partial_r\psi_0(0) \neq 0$ (see e.g. in the proof of Corollary 4).

Then a suitable reduction is done by means of the new function

$$u(r) := \frac{d\log\psi_0}{d\log r} = \frac{r}{\psi_0}\frac{d\psi_0}{dr},$$

which is well-defined again according to (4.39). In particular, by taking $\log\psi_0$ we are able to treat the zero-order term. This definition immediately implies

$$\partial_r u = \frac{1}{r}\left(u - u^2 + \frac{r^2}{\psi_0}\partial_r^2\psi_0\right),$$

so that we obtain from (4.43) the first-order, but non-linear equation

$$-r\partial_r u - u^2 - qr\partial_r(\log\widetilde{h})u + 1 = 0.$$

The variable transformation

$$s := \log(\tfrac{r}{R})$$

finally yields

$$\partial_s u = -u^2 + qau + 1 = 0, \tag{4.45}$$

where

$$a = -\partial_s(\log\widetilde{h}) = -\frac{r}{\widetilde{h}}\partial_r\widetilde{h} \geq 0,$$

together with the limit behavior

$$\lim_{s\to-\infty} u = 1. \tag{4.46}$$

In particular, we follow from (4.44) and (4.45) that

$$u \geq 1 \quad \text{for all } s, \tag{4.47}$$

since $\lim_{s\to-\infty} u = 1$ and the slope of u will become positive as soon as $u \leq 1$ due to the defining equation.

Note that we can identify the cap, foot and precursor region in the new variable s:

- cap region: $-s \gg 1$
- foot region: $0 < -s \ll 1$
- precursor region: $s > 0$

Approximate solutions u for leading order droplet profile

We will derive solutions of (4.45) to leading order in the regime $R \gg 1$ based on the droplet profile (2.24) for the three different regions. More precisely, we will first plug in the profile to obtain leading order expressions of the ODE coefficient a. These expressions allow us to deduce approximate solutions, which coincide with the exact ones to leading order. For the convenience of the reader, we summarize all intermediate and final results for the leading order solutions u and ψ_0 in Table 4.1 below.

Let us clearly state the following: For $q > 3$, the integral $\mathcal{I}_{\psi_0}$ is dominated by the foot region of the equilibrium profile. Hence, we expect an $\mathcal{U}$-dependent error of order one in the constant of the leading order term, since we appeal to the mesoscopic profile.

Using the profile (2.24), we obtain for the coefficient a

$$a = -\partial_s(\log \widetilde{h}) = \begin{cases} \frac{2\exp(2s)}{1-\exp(2s)+\frac{\sqrt{2}}{R}} & \text{for } s < 0, \\ 0 & \text{for } s > 0. \end{cases} \tag{4.48}$$

Then the leading order behavior of a in the different regions is given by

$$a = \begin{cases} 2\exp(2s) & \text{for } -s \gg 1, \\ \frac{2}{-2s+\frac{\sqrt{2}}{R}} & \text{for } 0 < -s \ll 1, \\ 0 & \text{for } s > 0. \end{cases} \tag{4.49}$$

In particular, a is to leading order independent of R for $-s \gg \frac{1}{R}$. Let us now deduce from (4.49) the leading order expressions of u.

Cap region $-s \gg 1$. We start with analyzing the cap region. Note that we have $a = 2\exp(2s) \ll 1$ for $-s \gg 1$. Hence, (4.45) turns into

$$\partial_s u = -u^2 + 1,$$

so that due to the boundary condition (4.46) it is reasonable to gain information from the linearization around 1, that is $u \approx 1 + \bar{u}$. We obtain to leading order for $-s \gg 1$

$$\partial_s \bar{u} = -2\bar{u} + 2q\exp(2s).$$

The solutions of this linear ODE are easy to get (by Duhamel's principle):

$$\bar{u} = \tfrac{1}{2}q\exp(2s) + \text{const}\exp(-2s),$$

so that in view of the limit behavior (4.46)

$$u = 1 + \tfrac{1}{2}q\exp(2s)$$

in the cap region $-s \gg 1$. Obviously, the solution is to leading order independent of R. Since the coefficient a is independent of R for $-s \gg \frac{1}{R}$, we obtain by matching that

$$u \text{ is to leading order independent of } R \text{ for } -s \gg \frac{1}{R}. \tag{4.50}$$

Therefore, the overlap region with the foot is defined by $\frac{1}{R} \ll -s \ll 1$.

Foot region $0 < -s \ll 1$**.** Since $a \gg 1$ in the foot region, see (4.49), it follows that $u \gg 1$ according to (4.45) and $q > 0$. Hence, to leading order (4.45) turns into

$$\partial_s u = -u^2 + \frac{q}{-s + \frac{1}{\sqrt{2}R}} u. \tag{4.51}$$

A solution can be derived by introducing v through $u = \frac{\partial_s v}{v}$. Then (4.51) transforms into

$$\partial_s^2 v = \frac{q}{-s + \frac{1}{\sqrt{2}R}} \partial_s v,$$

which finally gives for $w = \partial_s v$

$$\partial_s w = \frac{q}{-s + \frac{1}{\sqrt{2}R}} w.$$

It can be readily seen that

$$w = C \left(-s + \frac{1}{\sqrt{2}R} \right)^{-q},$$

and consequently,

$$v = \begin{cases} -C \log(-s + \frac{1}{\sqrt{2}R}) + \tilde{C} & \text{for } q = 1, \\ -\frac{C}{1-q}(-s + \frac{1}{\sqrt{2}R})^{-q+1} + \tilde{C} & \text{for } q \neq 1. \end{cases}$$

Finally, the solution u is given by

$$u = \frac{\partial_s v}{v} = \begin{cases} \frac{1}{(-s+\frac{1}{\sqrt{2}R})(C - \log(-s+\frac{1}{\sqrt{2}R}))} & \text{for } q = 1, \\ \frac{q-1}{(-s+\frac{1}{\sqrt{2}R})(1+C(-s+\frac{1}{\sqrt{2}R})^{q-1})} & \text{for } q \neq 1. \end{cases}$$

To see whether C depends on R or not, we simplify this equation in the regime $\frac{1}{R} \ll -s \ll 1$ to

$$u = \begin{cases} \frac{1}{-s(C - \log(-s))} & \text{for } q = 1, \\ \frac{q-1}{(-s)(1+C(-s)^{q-1})} & \text{for } q \neq 1. \end{cases}$$

By matching with the cap region (4.50), we infer that the constant C is independent of R to leading order. Hence, we obtain the leading order solution for $0 < -s \ll 1$

$$u = \begin{cases} \frac{q-1}{-s+\frac{1}{\sqrt{2}R}} & \text{for } q > 1, \\ \frac{1}{(-s+\frac{1}{\sqrt{2}R}) \log(\frac{1}{-s+\frac{1}{\sqrt{2}R}})} & \text{for } q = 1, \\ \frac{\overline{C}}{(-s+\frac{1}{\sqrt{2}R})^q} & \text{for } q \in (0,1), \end{cases} \tag{4.52}$$

where $\overline{C}$ is a constant independent of R. These expressions are in accordance with the initially expected behavior $u \gg 1$.

Precursor region $s > 0$**.** In the precursor region, (4.45) simplifies to

$$\partial_s u = -u^2 + 1 \quad \text{for } s > 0.$$

According to (4.47), the only relevant solution is

$$u = \frac{1}{\tanh(s + C)} \quad \text{for } s > 0.$$

The constant C is determined by matching with the foot region. In particular, it is not independent of R. To leading order in $R \gg 1$

$$u = \begin{cases} \frac{1}{\tanh(s + \frac{1}{(q-1)\sqrt{2}R})} & \text{for } q > 1, \\ \frac{1}{\tanh(s + \frac{\log(\sqrt{2}R)}{\sqrt{2}R})} & \text{for } q = 1, \\ \frac{1}{\tanh(s + \frac{1}{C(\sqrt{2}R)^q})} & \text{for } q \in (0,1). \end{cases} \tag{4.53}$$

Recovering ψ_0 **from** u

Case $q > 1$**.** Let us first turn to the *precursor region* $s > 0$. It is easy to see that for $\tilde{s} \ll 1$

$$\tanh^{-1}(s + \tilde{s}) = \frac{1 + \exp(-2(s + \tilde{s}))}{1 - \exp(-2(s + \tilde{s}))} \approx \frac{1 + (1 - 2\tilde{s})\exp(-2s)}{1 - (1 - 2\tilde{s})\exp(-2s)}.$$

Hence, we obtain in the regime $R \gg 1$

$$\tanh^{-1}\left(s + \frac{1}{(q-1)\sqrt{2}R}\right) \approx \frac{1 + \left(1 - \frac{\sqrt{2}}{(q-1)R}\right)\exp(-2s)}{1 - \left(1 - \frac{\sqrt{2}}{(q-1)R}\right)\exp(-2s)}. \tag{4.54}$$

Next we recall that for large r, the pressure ψ_0 is of the form

$$\psi_0(r) \approx r + \frac{C}{r},$$

see (4.35). Thus, one readily sees

$$\log \psi_0(s) = s + \log\left(1 + \frac{C}{R^2}\exp(-2s)\right),$$

and consequently,

$$\partial_s \log \psi_0(s) = \frac{1 - \frac{C}{R^2}\exp(-2s)}{1 + \frac{C}{R^2}\exp(-2s)},$$

so that matching with (4.54) yields the constant $C = -R^2 + \frac{\sqrt{2}}{(q-1)}R$. We finally end up with

$$\psi_0(r) = r - \left(1 - \frac{\sqrt{2}}{(q-1)R}\right)\frac{R^2}{r} \qquad \text{for } r \geq R.$$

Next we turn to the *foot region* $0 < -s \ll 1$. Elementary integration of (4.52) yields

$$\log \psi_0(s) = (1-q) \log \left(-s + \frac{1}{\sqrt{2}R} \right) + C,$$

so that

$$\psi_0(r) = C \left(\frac{1}{\sqrt{2}R} \right)^{1-q} \left(-\sqrt{2}R \log \left(\frac{r}{R} \right) + 1 \right)^{1-q}.$$

Matching with the precursor region, i.e. $r \to R$, gives $C(\frac{1}{\sqrt{2}R})^{1-q} = \frac{\sqrt{2}}{q-1}$. For $r \approx R$, we can approximate $\log(\frac{r}{R}) \approx \frac{r}{R} - 1$ and obtain to leading order

$$\psi_0(r) = \frac{\sqrt{2}}{q-1} \left(\sqrt{2}(R-r) + 1 \right)^{1-q} \qquad \text{for } r \approx R,\ r < R.$$

Let us conclude with the *cap region* $-s \gg 1$. Again, integrating (4.50) and replacing s by $\log \frac{r}{R}$ yield

$$\log \psi_0(r) = C + \log \frac{r}{R} + \frac{1}{4} q \left(\frac{r}{R} \right)^2.$$

We can approximate $\exp\left(\frac{1}{4} q \left(\frac{r}{R} \right)^2 \right) \approx 1 + \frac{1}{4} q \left(\frac{r}{R} \right)^2$ for $0 < r \ll R$, so that

$$\psi_0(r) = C \left(1 + \frac{1}{4} q \left(\frac{r}{R} \right)^2 \right) \frac{r}{R}.$$

From the foot region, we can only gain information on the scaling of C in terms of R; a quantitative matching is not possible, since the regions do not overlap. We find that $C = C_q R^{1-q}$, which finally gives

$$\psi_0(r) = C_q \left(1 + \frac{1}{4} q \left(\frac{r}{R} \right)^2 \right) \frac{r}{R^q} \qquad \text{for } 0 < r \ll R.$$

Case $q = 1$. The asymptotic expressions of ψ_0 are derived analogously to the case $q > 1$. Hence, we will present only the main steps and results.

In the *precursor region* $s > 0$, we obtain

$$\psi_0(r) = r - \left(1 - \frac{\sqrt{2} \log(\sqrt{2}R)}{R} \right) \frac{R^2}{r} \qquad \text{for } r \geq R.$$

The expression of u in the *foot region* $0 < -s \ll 1$ can be again integrated:

$$\log \psi_0(s) = \log \log \left(-s + \frac{1}{\sqrt{2}R} \right) + C,$$

so that in the regime $r \approx R$

$$\psi_0(r) = -\sqrt{2} \log \left(1 - \frac{r}{R} + \frac{1}{\sqrt{2}R} \right) \qquad \text{for } r \approx R,\ r < R,$$

where the constant $C = -\sqrt{2}$ is obtained by matching with the precursor region.

The analysis for the *cap region* works completely analogous to the case $q > 1$. We get

$$\psi_0(r) = C\left(1 + \frac{1}{4}\left(\frac{r}{R}\right)^2\right)\frac{r}{R} \qquad \text{for } 0 < r \ll R.$$

Case $q \in (0,1)$**.** The same procedure as in the other cases yields for the *precursor region* $s > 0$ the expression

$$\psi_0(r) = r - \left(1 - \frac{2}{C(\sqrt{2}R)^q}\right)\frac{R^2}{r}.$$

Next, for the *foot region* we obtain

$$\log\psi_0(s) = \frac{1}{q-1}\tilde{C}\left(-s + \frac{1}{\sqrt{2}R}\right)^{1-q} + C,$$

where $\tilde{C}$ is a constant independent of R. The constant C can be again determined by matching with the precursor region. It reveals that

$$C = \frac{(1-q)(\sqrt{2}R)^{1-q}}{(1-q)(\sqrt{2}R)^{1-q} - \tilde{C}}\frac{\sqrt{2}}{\tilde{C}}(\sqrt{2}R)^{1-q} \approx \frac{\sqrt{2}}{\tilde{C}}(\sqrt{2}R)^{1-q}$$

to leading order in $R \gg 1$. Therefore, we get

$$\psi_0(r) = (\sqrt{2}R)^{1-q}\left(\frac{\sqrt{2}}{\tilde{C}} - \frac{\sqrt{2}}{1-q}\left(1 - \frac{r}{R} + \frac{1}{\sqrt{2}R}\right)^{1-q}\right) \qquad \text{for } r \approx R,\ r < R.$$

In the *cap region* $-s \gg 1$, we have as before

$$\psi_0(r) = C_q\left(1 + \frac{1}{4}q\left(\frac{r}{R}\right)^2\right)\frac{r}{R^q} \qquad \text{for } r \ll R$$

with a constant C_q independent of R to leading order.

A summary of the asymptotic analysis of this subsection is given in Table 4.1.

Table 4.1: Analysis of ψ_0: Overview of leading order expressions.

		cap region $-s \gg 1 \quad (r \ll R)$	**foot region** $0 < -s \ll 1 \quad (r \approx R \text{ and } r < R)$	**precursor region** $s > 0 \quad (r \geq R)$
ODE coefficient a		$2\exp(2s)$	$\left(-s + \frac{1}{\sqrt{2}R}\right)^{-1}$	0
$u = \partial_s \log \psi_0$ $(s = \log\left(\frac{r}{R}\right))$	$q \in (0,1)$	$1 + \frac{1}{2}q\exp(2s)$	$C\left(-s + \frac{1}{\sqrt{2}R}\right)^{-q}$	$\tanh^{-1}\left(s + \frac{1}{C(\sqrt{2}R)^q}\right)$
	$q = 1$		$\left(-s + \frac{1}{\sqrt{2}R}\right)^{-1} \log^{-1}\left(\frac{1}{-s+\frac{1}{\sqrt{2}R}}\right)$	$\tanh^{-1}\left(s + \frac{\log(\sqrt{2}R)}{\sqrt{2}R}\right)$
	$q > 1$		$(q-1)\left(-s + \frac{1}{\sqrt{2}R}\right)^{-1}$	$\tanh^{-1}\left(s + \frac{1}{(q-1)\sqrt{2}R}\right)$
pressure ψ_0	$q \in (0,1)$	$C_q\left(1 + \frac{1}{4}q\left(\frac{r}{R}\right)^2\right)\frac{r}{R^q}$	$(\sqrt{2}R)^{1-q}\left(\frac{\sqrt{2}}{C} - \frac{\sqrt{2}}{1-q}\left(1 - \frac{r}{R} + \frac{1}{\sqrt{2}R}\right)^{1-q}\right)$	$r - \left(1 - \frac{2}{C(\sqrt{2}R)^q}\right)\frac{R^2}{r}$
	$q = 1$		$-\sqrt{2}\log\left(1 - \frac{r}{R} + \frac{1}{\sqrt{2}R}\right)$	$r - \left(1 - \frac{\sqrt{2}\log(\sqrt{2}R)}{R}\right)\frac{R^2}{r}$
	$q > 1$		$\frac{\sqrt{2}}{q-1}(\sqrt{2}(R-r)+1)^{1-q}$	$r - \left(1 - \frac{\sqrt{2}}{(q-1)R}\right)\frac{R^2}{r}$

Scaling of $\mathcal{I}_{\psi_0}$

Based on the asymptotic expressions of ψ_0, see Table 4.1, we will present the scaling of the numerator of the migration factor (4.40), i.e.

$$\mathcal{I}_{\psi_0} = -\int \psi_0(x)\partial_1\widetilde{h}(x)\,dx = -\pi\int_0^\infty \psi_0(r)\partial_r\widetilde{h}(r)r\,dr, \tag{4.55}$$

in terms of $R \gg 1$. In particular, we will identify depending on the mobility exponent q, which region provides the dominant contribution to the scaling.

Note that we will – as a leading order approximation in $R \gg 1$ – again plug in the profile (2.24), so that in particular we have

$$\partial_r\widetilde{h}(r) \approx \begin{cases} -\sqrt{2}\frac{r}{R} & \text{for } r \le R, \\ 0 & \text{for } r > R, \end{cases}$$

to leading order. Hence, we obtain

$$\mathcal{I}_{\psi_0} \approx \frac{\sqrt{2}\pi}{R}\int_0^R \psi_0(r)r^2\,dr.$$

Obviously, the precursor region has no impact; only the cap and foot region compete.

The contribution of the cap region can be derived in general for all $q > 0$:

$$\begin{aligned} \frac{\sqrt{2}\pi}{R}\int_0^R \psi_0(r)r^2\,dr &= C_q\frac{\sqrt{2}\pi}{R}\int_0^R \left(1+\frac{1}{4}q\left(\frac{r}{R}\right)^2\right)\left(\frac{r}{R}\right)^3\frac{1}{R^{q-3}}\,dr \\ &= C_q\sqrt{2}\pi\,R^{3-q}\int_0^1\left(1+\frac{1}{4}q\hat{r}^2\right)\hat{r}^3\,d\hat{r}, \end{aligned}$$

so that in terms of scaling

$$\mathcal{I}_{\psi_0}(\text{cap}) \approx CR^{3-q}$$

for $R \gg 1$.

Now we turn to the foot region contribution, which dominates for $q \ge 2$: Based on the asymptotic profile of ψ_0 in the case $q > 1$, we derive for $\hat{r} = \frac{r}{R}$

$$\begin{aligned} \mathcal{I}_{\psi_0}(\text{foot}) &\approx \frac{2\pi}{q-1}\,R^2\int_0^1 \frac{\hat{r}^2}{(\sqrt{2}R(1-\hat{r})+1)^{q-1}}\,d\hat{r} \\ &\approx \frac{2\pi}{q-1}\,R^2\left(\int_0^{1-\frac{1}{\sqrt{2}R}} \frac{\hat{r}^2}{(\sqrt{2}R(1-\hat{r}))^{q-1}}\,d\hat{r} + \int_{1-\frac{1}{\sqrt{2}R}}^1 \hat{r}^2\,d\hat{r}\right) \\ &\approx \frac{2\pi R^2}{q-1}\begin{cases} \frac{1}{\sqrt{2}R}\log R & \text{for } q = 2, \\ \frac{1}{\sqrt{2}(q-2)}\frac{1}{R} & \text{for } q > 2, \end{cases} \\ &= \begin{cases} \sqrt{2}\pi R\log R & \text{for } q = 2, \\ \frac{\sqrt{2}\pi}{(q-2)(q-1)}R & \text{for } q > 2. \end{cases} \end{aligned}$$

Collecting the scaling results from the cap and foot region, we have proven the scaling relations (4.40), the first part of Proposition 7.

4.2.4 Asymptotic analysis of ψ_1

For the analysis of (4.41), let us first point out how the 2-d expression relates to the corresponding 1-d expression, see (4.22). For this purpose, rewrite

$$\mathcal{I}_{\psi_1} = \int m|\nabla\psi_1|^2\,dx = \int \frac{1}{m}|J_1|^2\,dx,$$

where J_1 solves $-\partial_1(\widetilde{h} - h_\infty) + \nabla \cdot J_1 = 0$. In one dimension, a solution to this can be given explicitly, that is $J_1 = \widetilde{h} - h_\infty$. Hence,

$$\mathcal{I}_{\psi_1} = \int \frac{1}{m}(\widetilde{h} - h_\infty)^2\,dx$$

in accordance with (4.22). Note that in the following, we will replace the limit value h_∞ by 1 since these values only differ by an order of $\frac{1}{R}$, which is negligible.

As in the one-dimensional case, we may expect a crossover at $q = 3$: For $q < 3$, the main contribution in terms of scaling comes from the cap region, which has to leading order parabolic shape, see (2.24), and for $q > 3$, it comes from the foot region and therefore in particular depends on the special form of the potential $\mathcal{U}$.

Case $q = 0$. The case $q = 0$ is special in the sense that ψ_1 as a solution of (4.34) can be given explicitly for the leading order parabolic droplet profile, that is, as a solution of

$$\begin{aligned}
\sqrt{2}\frac{r}{R} - \partial_r^2\psi_1 - \frac{1}{r}\partial_r\psi_1 + \frac{1}{r^2}\psi_1 &= 0, \qquad r \le R,\\
-\partial_r^2\psi_1 - \frac{1}{r}\partial_r\psi_1 + \frac{1}{r^2}\psi_1 &= 0, \qquad r > R,\\
\psi_1(0) = 0, \qquad &\lim_{r\to\infty}\partial_r\psi_1(r) = 0.
\end{aligned}$$

As mentioned before, the fundamental system of the ODE operator $-\partial_r^2 - \frac{1}{r}\partial_r + \frac{1}{r^2}$ is given by $\{r, \frac{1}{r}\}$, where only the first one is relevant due to the boundary condition at $r = 0$. Since $\frac{R^2}{4\sqrt{2}}\left(\frac{r}{R}\right)^3$ is a special solution for $r \le R$, we gain solutions

$$\psi_1(r) = \frac{R^2}{4\sqrt{2}}\left(\left(\frac{r}{R}\right)^3 + C\frac{r}{R}\right) \qquad \text{for } r \le R.$$

On the other hand, the solutions for $r > R$ are given by $\frac{\tilde{C}}{r}$. Therefore, we get by C^1-matching at $r = R$ that $C = -2$ and $\tilde{C} = -\frac{R^2}{4\sqrt{2}}$, and consequently,

$$\psi_1(r) = \frac{R^2}{4\sqrt{2}}\begin{cases}\left(\frac{r}{R}\right)^3 - 2\frac{r}{R} & \text{for } r < R,\\ -\frac{R}{r} & \text{for } r \ge R.\end{cases}$$

Hence, we obtain as claimed

$$\int m|\nabla\psi_1|^2\,dx = \int \partial_1\widetilde{h}\,\psi_1\,dx = \pi\int_0^R \partial_r\widetilde{h}\,\psi_1\,r\,dr \approx \frac{\pi}{12}\,R^4.$$

However, for the general case $q > 0$ and in contrast to the analysis of $\mathcal{I}_{\psi_0}$, we do not need an explicit knowledge of the (asymptotic) form of ψ_1, since $\mathcal{I}_{\psi_1}$ has the following variational characterization:

$$\begin{aligned} \tfrac{1}{2}\mathcal{I}_{\psi_1} &= \min_J \left\{ \tfrac{1}{2}\int \frac{1}{m}|J|^2 \, dx \;\middle|\; -\partial_1 \widetilde{h} + \nabla \cdot J = 0 \right\} && \text{(4.56a)} \\ &= \max_\psi \left\{ -\tfrac{1}{2}\int m|\nabla\psi|^2 \, dx + \int \partial_1 \widetilde{h}\, \psi \, dx \right\}. && \text{(4.56b)} \end{aligned}$$

This representation allows us to identify the limiting behavior (depending on q) by "sandwiching" the rescaled limit of $\mathcal{I}_{\psi_1}$ for $R \to \infty$ by the minimizer and maximizer, respectively, in suitable non-dimensionalization.

Case $q \in (0,3)$**.** We introduce the rescaling $x = R\hat{x}$ or $r = R\hat{r}$, respectively. According to the leading order cap profile of the droplet, a suitable rescaling of the other quantities is given by

$$\widetilde{h} = R\hat{h}, \quad m = R^q \hat{m}, \quad \psi = R^{2-q}\hat{\psi}, \quad J = R\hat{J}.$$

Note that this rescaling is consistent with the scaling of ψ_1 in the case $q = 0$. In this new variables, the variational characterization (4.56) turns into

$$\begin{aligned} R^{q-4}\ \tfrac{1}{2}\mathcal{I}_{\psi_1} &= \min_{\hat{J}} \left\{ \tfrac{1}{2}\int \frac{1}{\hat{m}}|\hat{J}|^2 \, d\hat{x} \;\middle|\; -\hat{\partial}_1 \hat{h} + \hat{\nabla}\cdot\hat{J} = 0 \right\} && \text{(4.57a)} \\ &= \max_{\hat{\psi}} \left\{ -\tfrac{1}{2}\int \hat{m}|\hat{\nabla}\hat{\psi}|^2 \, d\hat{x} + \int \hat{\partial}_1 \hat{h}\, \hat{\psi} \, d\hat{x} \right\}. && \text{(4.57b)} \end{aligned}$$

Now let us study the limiting behavior of the variational problem. Referring to the leading order droplet profile, we obtain for the rescaled profile in the limit

$$\hat{h} = R^{-1}\widetilde{h} \overset{R\uparrow\infty}{\longrightarrow} \hat{h}_{\lim} := \begin{cases} \frac{1}{\sqrt{2}}(1-\hat{r}^2) & \text{for } \hat{r} < 1, \\ 0 & \text{for } \hat{r} > 1, \end{cases}$$

and consequently,

$$\hat{m} = \hat{h}^q \overset{R\uparrow\infty}{\longrightarrow} \hat{m}_{\lim} := \begin{cases} \left(\frac{1}{\sqrt{2}}(1-\hat{r}^2)\right)^q & \text{for } \hat{r} < 1, \\ 0 & \text{for } \hat{r} > 1. \end{cases}$$

Now we prepare the sandwich. We immediately obtain from (4.57) that

$$\begin{aligned} & \max_{\hat{\psi}} \left\{ -\tfrac{1}{2}\int \hat{m}_{\lim}|\hat{\nabla}\hat{\psi}|^2 \, d\hat{x} + \int \hat{\partial}_1 \hat{h}_{\lim}\hat{\psi} \, d\hat{x} \right\} && \text{(4.58)} \\ \leq\ & \liminf_{R\to\infty}\ R^{q-4}\ \tfrac{1}{2}\mathcal{I}_{\psi_1} \\ \leq\ & \limsup_{R\to\infty}\ R^{q-4}\ \tfrac{1}{2}\mathcal{I}_{\psi_1} \\ \leq\ & \min_{\hat{J}} \left\{ \tfrac{1}{2}\int \frac{1}{\hat{m}_{\lim}}|\hat{J}|^2 \, d\hat{x} \;\middle|\; -\hat{\partial}_1 \hat{h}_{\lim} + \hat{\nabla}\cdot\hat{J} = 0 \right\} && \text{(4.59)} \end{aligned}$$

where we set $\int \frac{1}{\hat{m}_{\lim}} |\hat{J}|^2 \, d\hat{x} = \infty$, if the support of $\hat{J}$ is not contained in the support of $\hat{m}_{\lim}$. Next note that a minimizer $\hat{J}_{\min}$ of (4.59), if it exists, has the form of a gradient: $\hat{J}_{\min} = -\hat{m}\hat{\nabla}\hat{\psi}_{\min}$. In turn, $\hat{\psi}_{\min}$ is the maximizer of (4.58), so that the sandwich is squeezed to

$$\begin{aligned} \lim_{R\to\infty} R^{q-4} \, \tfrac{1}{2}\mathcal{I}_{\psi_1} &= \max_{\hat{\psi}} \left\{ -\tfrac{1}{2} \int \hat{m}_{\lim} |\hat{\nabla}\hat{\psi}|^2 \, d\hat{x} + \int \hat{\partial}_1 \hat{h}_{\lim} \hat{\psi} \, d\hat{x} \right\} \\ &= \min_{\hat{J}} \left\{ \tfrac{1}{2} \int \frac{1}{\hat{m}_{\lim}} |\hat{J}|^2 \, d\hat{x} \;\Big|\; -\hat{\partial}_1 \hat{h}_{\lim} + \hat{\nabla}\cdot\hat{J} = 0 \right\}. \end{aligned}$$

This equation shows the claimed scaling behavior (4.40), where the constant C_q^1 is determined by the non-dimensionalized variational problem, that is in polar coordinates

$$C_1(q) := \tag{4.60}$$
$$\pi \max_{\hat{\psi}} \left\{ -\int_0^1 \left(\tfrac{1}{\sqrt{2}} \left(1 - \hat{r}^2\right) \right)^q \left(\left(\partial_{\hat{r}} \hat{\psi} \right)^2 + \left(\tfrac{1}{\hat{r}} \hat{\psi} \right)^2 \right) \hat{r} \, d\hat{r} - 2\sqrt{2} \int_0^1 \hat{\psi} \, \hat{r}^2 \, d\hat{r} \right\}.$$

Remark (Derivation of the numerical constant $C_1(q)$). For later purposes it is necessary to determine the numerical constant $C_1(q)$ for different $q \in (0, 3)$. While for the case $q = 1$ the maximizer in (4.60) can be given explicitly, namely $\psi = -r$, this is done numerically by a Galerkin Ansatz with piecewise linear functions to solve the maximum problem in (4.60).

In the figure to the right, the numerically derived maximizer ψ is given for different values of q and 10^5 grid points on the interval $[0, 1]$. For $C_1(q)$ we obtain the following values:

	$q = 0.5$	$q = 1$	$q = 1.5$	$q = 2$	$q = 2.5$
$C_1(q)$	0.7259	1.1107	1.7142	2.8026	5.5615

Furthermore the numerics reveal (logarithmic) singularities in $r = 1$ for $q \geq 2$, see figure to the right, as suggested by back-of-the-envelope arguments based on the Euler–Lagrange equation of the variational problem in (4.60).

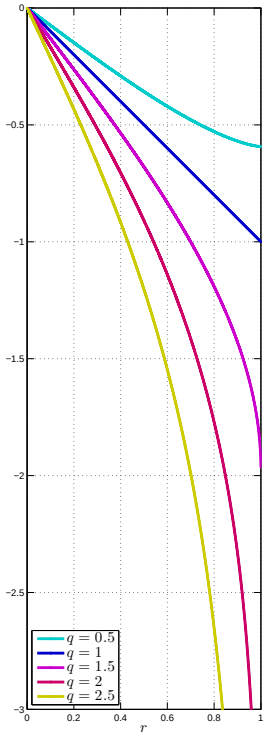

It remains to show the existence of a $\hat{J}$ such that

$$-\hat{\partial}_1 \hat{h}_{\lim} + \hat{\nabla}\cdot\hat{J} = 0 \quad \text{with} \quad \int \frac{1}{\hat{m}_{\lim}} |\hat{J}|^2 \, d\hat{x} < \infty.$$

Then the existence of a unique minimizer is guaranteed. For this purpose, choose $\hat{J} := \binom{\hat{h}_{\lim}}{0}$, so that in particular the support of $\hat{J}$ coincides with the support of $\hat{m}_{\lim}$. Obviously, $\hat{J}$ satisfies the continuity equation. Furthermore,

$$\int \frac{1}{\hat{m}_{\lim}} |\hat{J}|^2 \, d\hat{x} = 2\sqrt{2}^{2-q}\pi \int_0^1 (1-\hat{r}^2)^{2-q}\hat{r} \, d\hat{r} < \infty$$

provided $q < 3$. This finishes the treatment of the case $q \in (0,3)$.

For the subsequent analysis, let us rewrite the variational characterization (4.56a) in the following way:

$$\begin{aligned} & \min_J \left\{ \tfrac{1}{2} \int \frac{1}{m} |J|^2 \, dx \;\middle|\; -\partial_1 \widetilde{h} + \nabla \cdot J = 0 \right\} \\ = \; & \min_J \left\{ \tfrac{1}{2} \int \frac{1}{m} \left| J + (\widetilde{h}-1)\begin{pmatrix} 1 \\ 0 \end{pmatrix} \right|^2 dx \;\middle|\; \nabla \cdot J = 0 \right\}. \end{aligned}$$

According to the special form of ψ_1 in (4.32), the flux $J = -m\nabla\psi_1 - (\widetilde{h}-1)\binom{1}{0}$ in polar coordinates assumes the form

$$J(r,\theta) = \begin{pmatrix} \cos\theta & -\sin\theta \\ \sin\theta & \cos\theta \end{pmatrix} \begin{pmatrix} \cos\theta \, J_1(r) \\ -\sin\theta \, J_2(r) \end{pmatrix}.$$

Therefore, we get

$$\begin{aligned} & \min_J \left\{ \tfrac{1}{2} \int \frac{1}{m} \left| J + (\widetilde{h}-1)\begin{pmatrix} 1 \\ 0 \end{pmatrix} \right|^2 dx \;\middle|\; \nabla \cdot J = 0 \right\} \\ = \; & \min_{(J_1,J_2)} \left\{ \tfrac{\pi}{2} \int_0^\infty \frac{1}{m} \left((J_1 + (\widetilde{h}-1))^2 + (J_2 + (\widetilde{h}-1))^2 \right) r \, dr \;\middle|\; \partial_r J_1 + \tfrac{1}{r} J_1 - \tfrac{1}{r} J_2 = 0 \right\} \\ = \; & \min_{J_1} \left\{ \tfrac{\pi}{2} \int_0^\infty \frac{1}{m} \left((J_1 + (\widetilde{h}-1))^2 + (r\partial_r J_1 + J_1 + (\widetilde{h}-1))^2 \right) r \, dr \right\}. \end{aligned}$$

Hence, in the following, we will refer to the reformulation of (4.56) in polar coordinates

$$\begin{aligned} & \tfrac{1}{2\pi} \mathcal{I}_{\psi_1} \\ = \; & \min_{J_1} \left\{ \tfrac{1}{2} \int_0^\infty \frac{1}{m} \left((J_1 + (\widetilde{h}-1))^2 + (r\partial_r J_1 + J_1 + (\widetilde{h}-1))^2 \right) r \, dr \right\} \quad (4.61a) \\ = \; & \max_{\psi} \left\{ -\tfrac{1}{2} \int_0^\infty m \left((\partial_r \psi)^2 + \left(\tfrac{1}{r}\psi\right)^2 \right) r \, dr - \int_0^\infty (\widetilde{h}-1)\partial_r \psi \, r \, dr \right\}. \quad (4.61b) \end{aligned}$$

Case $q > 3$. We will proceed in the same manner as in the previous case but refer to the reformulation (4.61). Inspired by the asymptotic analysis for the foot region of a stationary droplet we choose the rescaling

$$r = R \exp\left(\tfrac{\hat{r}}{R}\right), \qquad J_1 = R^{-1}\hat{J}_1.$$

In this new variables, we obtain on the one hand from (4.61a)

$$\begin{aligned} &\tfrac{1}{2\pi}\mathcal{I}_{\psi_1} \\ &= R \min_{\hat{J}_1} \left\{ \tfrac{1}{2} \int_{-\infty}^{\infty} \frac{1}{\hat{m}} \left(\left(R^{-1}\hat{J}_1 + (\hat{h}-1) \right)^2 + \left(\partial_{\hat{r}}\hat{J}_1 + R^{-1}\hat{J}_1 + (\hat{h}-1) \right)^2 \right) \, d\hat{r} \right\}, \end{aligned}$$

and on the other hand from (4.61b)

$$\begin{aligned} &\tfrac{1}{2\pi}\mathcal{I}_{\psi_1} \\ &= R \max_{\hat{\psi}} \left\{ -\tfrac{1}{2} \int_{-\infty}^{\infty} \hat{m} \left((\partial_{\hat{r}}\hat{\psi})^2 + R^{-2} \left(\tfrac{1}{\hat{r}}\hat{\psi} \right)^2 \right) \, d\hat{r} - \int_{-\infty}^{\infty} (\hat{h}-1)\partial_{\hat{r}}\hat{\psi} \exp\left(\frac{\hat{r}}{R} \right) \, d\hat{r} \right\}. \end{aligned}$$

Now again, we turn to the question how the limit $\hat{h}_{\lim}$ of the rescaled droplet profile is characterized. From the asymptotic analysis of Section 2.1, we know that in the rescaling $r = R\exp\left(\frac{\hat{r}}{R}\right)$, the rescaled profile $\hat{h}$ is characterized through

$$\int_{\hat{h}(\hat{r})}^{2} \frac{1}{\sqrt{2\widetilde{\mathcal{U}}(h)}} \, dh = \hat{r} \qquad \text{for } |\hat{r}| \ll R,$$

where $\widetilde{\mathcal{U}}$ is defined in (2.12). In particular, in the limit $R \to \infty$ we have $\widetilde{\mathcal{U}}(h) = \mathcal{U}(h)$, which gives the integral characterization of $\hat{h}_{\lim}$ (as pointwise limits)

$$\int_{\hat{h}_{\lim}(\hat{r})}^{2} \frac{1}{\sqrt{2\mathcal{U}(h)}} \, dh = \hat{r} \qquad \text{for all } \hat{r}.$$

Consequently, we also obtain $\hat{m}_{\lim} = \hat{h}_{\lim}^q$. Finally by differentiation, it turns into

$$\partial_{\hat{r}}\hat{h}_{\lim} = -\sqrt{2\mathcal{U}(\hat{h}_{\lim})}$$

with the boundary conditions

$$\lim_{\hat{r}\to-\infty} \hat{h}_{\lim} = +\infty, \qquad \lim_{\hat{r}\to\infty} \hat{h}_{\lim} = 1.$$

Note that the details of $\hat{h}_{\lim}$ in particular depend on the explicit form of the potential $\mathcal{U}$.

Hence, in the limit one gets

$$\begin{aligned} &\max_{\hat{\psi}} \left\{ -\tfrac{1}{2} \int_{-\infty}^{\infty} \hat{m}_{\lim} (\partial_{\hat{r}}\hat{\psi})^2 \, d\hat{r} - \int_{-\infty}^{\infty} (\hat{h}_{\lim}-1)\partial_{\hat{r}}\hat{\psi} \, d\hat{r} \right\} \qquad (4.62) \\ \leq\ &\liminf_{R\to\infty} \ R^{-1} \ \tfrac{1}{2\pi}\mathcal{I}_{\psi_1} \\ \leq\ &\limsup_{R\to\infty} \ R^{-1} \ \tfrac{1}{2\pi}\mathcal{I}_{\psi_1} \\ \leq\ &\min_{\hat{J}_1} \left\{ \tfrac{1}{2} \int_{-\infty}^{\infty} \frac{1}{\hat{m}_{\lim}} \left((\hat{h}_{\lim}-1)^2 + (\partial_{\hat{r}}\hat{J}_1 + (\hat{h}_{\lim}-1))^2 \right) \, d\hat{r} \right\}. \qquad (4.63) \end{aligned}$$

Elementary optimization reveals that the maximizer of (4.62) is characterized by $\partial_r \hat{\psi} = -\frac{\hat{h}_{\rm lim}-1}{\hat{m}_{\rm lim}}$, and the minimizer of (4.63) by $\partial_{\hat{r}} \hat{J}_1 = -(\hat{h}_{\rm lim}-1)$, so that the upper bound and the lower bound coincide:

$$\begin{aligned} & \max_{\hat{\psi}} \left\{ -\tfrac{1}{2} \int_{-\infty}^{\infty} \hat{m}_{\rm lim} (\partial_{\hat{r}} \hat{\psi})^2 ; d\hat{r} - \int_{-\infty}^{\infty} (\hat{h}_{\rm lim}-1) \partial_{\hat{r}} \hat{\psi} \, d\hat{r} \right\} \\ = \; & \tfrac{1}{2} \int_{-\infty}^{\infty} \frac{(\hat{h}_{\rm lim}-1)^2}{\hat{m}_{\rm lim}} \, d\hat{r} \\ = \; & \min_{\hat{J}_1} \left\{ \tfrac{1}{2} \int_{-\infty}^{\infty} \frac{1}{\hat{m}_{\rm lim}} \left((\hat{h}_{\rm lim}-1)^2 + (\partial_{\hat{r}} \hat{J}_1 + (\hat{h}_{\rm lim}-1))^2 \right) \, d\hat{r} \right\}. \end{aligned}$$

The critical value

$$\tfrac{1}{2} \int_{-\infty}^{\infty} \frac{(\hat{h}_{\rm lim}-1)^2}{\hat{m}_{\rm lim}} \, d\hat{r} = \tfrac{1}{2} \int_{-\infty}^{\infty} \frac{(\hat{h}_{\rm lim}-1)^2}{\hat{h}_{\rm lim}^q} \, d\hat{r}$$

is finite since $q > 3$.

So finally, we obtain

$$\lim_{R\to\infty} R^{-1} \, \tfrac{1}{2\pi} \mathcal{I}_{\psi_1} = \tfrac{1}{2} \int_{-\infty}^{\infty} \frac{(\hat{h}_{\rm lim}-1)^2}{\hat{m}_{\rm lim}} \, d\hat{r}, \tag{4.64}$$

which validates the scaling relation (4.41) in the case $q > 3$. In particular, the constant $C_1(q)$ determined by the right hand side of (4.64) depends on the details of $\mathcal{U}$ according to the characterization of $\hat{h}_{\rm lim}$.

Case $q = 3$. Elementary optimization of (4.62) and (4.63) in the case $q > 3$ provided a differential characterization of the maximizer and minimizer, respectively.

In the following, we will give test functions for both of the variational characterization, which give identical bounds on $\frac{1}{2\pi}\mathcal{I}_{\psi_1}$ to leading order in $R \gg 1$. These functions coincide in the foot region $r \approx R$ with the maximum of (4.62) and the minimum of (4.63), respectively.

Let us begin with (4.61a): A suitable test function is

$$J_1(r) := \begin{cases} \frac{R}{\sqrt{2}} \left(1 - \frac{r}{R}\right)^2 & \text{for } r < R, \\ 0 & \text{for } r \geq R. \end{cases}$$

This function is constructed such that its derivative

$$\partial_r J_1 = \begin{cases} -\sqrt{2} \left(1 - \frac{r}{R}\right) & \text{for } r < R, \\ 0 & \text{for } r \geq R, \end{cases}$$

satisfies $r \partial_r J_1 \approx -(\widetilde{h} - 1)$ in the foot region.

Before we study the various contribution to the scaling, note that due to the triangle inequality

$$\begin{aligned} & \tfrac{1}{2}\int_0^\infty \frac{1}{m}\left(\left(J_1+(\widetilde{h}-1)\right)^2+\left(r\partial_r J_1+J_1+(\widetilde{h}-1)\right)^2\right) r\,dr \\ \leq\ & \tfrac{1}{2}\int_0^\infty \frac{1}{m}\left(2(J_1)^2+(\widetilde{h}-1)^2+(r\partial_r J_1+(\widetilde{h}-1))^2\right) r\,dr. \end{aligned} \tag{4.65}$$

Now, we investigate the scaling behavior in R of the individual terms:

$$\begin{aligned} \int_0^\infty \frac{1}{m}(J_1)^2\, r\,dr &\leq \int_0^R \frac{1}{(\widetilde{h}-1)^3}(J_1)^2\, r\,dr \\ &= \int_0^R \frac{\left(\frac{R}{\sqrt{2}}\left(1-\frac{r}{R}\right)^2\right)^2}{\left(\frac{R}{\sqrt{2}}\left(1-\frac{r}{R}\right)\left(1+\frac{r}{R}\right)\right)^3} r\,dr \\ &= \sqrt{2}R\int_0^1 \frac{1-\hat{r}}{(1+\hat{r})^3}\,\hat{r}\,d\hat{r} \\ &\sim R \ll R\log R, \end{aligned}$$

$$\begin{aligned} \tfrac{1}{2}\int_0^\infty \frac{1}{m}(\widetilde{h}-1)^2 r\,dr &\approx \tfrac{1}{2}\int_0^R \frac{\left(\frac{R}{\sqrt{2}}\left(1-\left(\frac{r}{R}\right)^2\right)\right)^2}{\left(\frac{R}{\sqrt{2}}\left(1-\left(\frac{r}{R}\right)^2\right)+1\right)^3} r\,dr \\ &= \tfrac{1}{2}R\int_0^1 \frac{\left(\frac{1}{\sqrt{2}}(1-\hat{r}^2)\right)^2}{\left(\frac{1}{\sqrt{2}}(1-\hat{r}^2)+\frac{1}{R}\right)^3}\,\hat{r}\,d\hat{r} \\ &\approx \tfrac{1}{2\sqrt{2}}\,R\log R, \end{aligned}$$

$$\begin{aligned} \tfrac{1}{2}\int_0^\infty \frac{1}{m}(r\partial_r J_1+(\widetilde{h}-1))^2\, r\,dr &\leq \tfrac{1}{2}\frac{1}{(\widetilde{h}-1)^3}(r\partial_r J_1+(\widetilde{h}-1))^2\, r\,dr \\ &\approx \tfrac{1}{2}\int_0^R \frac{\left(-\sqrt{2}r\left(1-\frac{r}{R}\right)+\frac{R}{\sqrt{2}}\left(1-\frac{r}{R}\right)\left(1+\frac{r}{R}\right)\right)^2}{\left(\frac{R}{\sqrt{2}}\left(1-\frac{r}{R}\right)\left(1+\frac{r}{R}\right)\right)^3} r\,dr \\ &= \tfrac{1}{\sqrt{2}}\,R\int_0^1 \frac{1-\hat{r}}{(1+\hat{r})^3}\,\hat{r}\,d\hat{r} \\ &\sim R \ll R\log R. \end{aligned}$$

Hence, using (4.65), we obtain in summation the upper bound

$$\tfrac{1}{2\pi}\mathcal{I}_{\psi_1} \lessapprox \tfrac{1}{2\sqrt{2}}\,R\log R.$$

For (4.61b), we choose the Ansatz

$$\psi(r) := \begin{cases} -\frac{1}{\sqrt{2}}\frac{r}{R}\frac{1}{\sqrt{2}(R-r)+1} & \text{for } r<R, \\ -\frac{1}{\sqrt{2}}\frac{R}{r} & \text{for } r\geq R. \end{cases}$$

This function is constructed such that its derivative

$$\partial_r \psi(r) = \begin{cases} -\left(1 + \frac{1}{\sqrt{2}R}\right) \frac{1}{(\sqrt{2}(R-r)+1)^2} & \text{for } r < R, \\ \frac{1}{\sqrt{2}} \frac{R}{r^2} & \text{for } r \geq R, \end{cases}$$

satisfies $m\partial_r \psi \approx -\widetilde{h}$ in the foot region.

Now, we turn to the scaling of the individual terms in (4.61b) to leading order in $R \gg 1$: Inside the droplet

$$\begin{aligned} -\tfrac{1}{2} \int_0^R m \left(\partial_r \psi\right)^2 r \, dr &\approx -\frac{R}{2} \int_0^R \frac{(\frac{1}{\sqrt{2}}(R-r)(1+\frac{r}{R})+1)^3}{(\sqrt{2}(R-r)+1)^4} \frac{r}{R} \, dr \\ &= -\frac{R}{2} \int_0^1 \frac{(\frac{1}{\sqrt{2}}(1-\hat{r}^2)+\frac{1}{R})^3}{(\sqrt{2}(1-\hat{r})+\frac{1}{R})^4} \hat{r} \, d\hat{r} \\ &\approx -\tfrac{1}{2\sqrt{2}} R \log R, \\ -\tfrac{1}{2} \int_0^R m \left(\tfrac{1}{r}\psi\right)^2 r \, dr &\approx -\tfrac{1}{4} R \int_0^1 \frac{(\frac{1}{\sqrt{2}}(1-\hat{r}^2)+\frac{1}{R})^3}{(\sqrt{2}(1-\hat{r})+\frac{1}{R}))^2} \hat{r} \, d\hat{r} \\ &\sim R \ll R \log R, \\ \int_0^\infty \partial_r \widetilde{h} \, \psi \, r \, dr &\approx R \int_0^1 \frac{1}{\sqrt{2}(1-\hat{r})+\frac{1}{R}} \hat{r}^3 \, d\hat{r} \\ &\approx \tfrac{1}{\sqrt{2}} R \log R, \end{aligned}$$

and outside the droplet (where $m \approx 1$ and $\partial_r \widetilde{h} \approx 0$)

$$\int_R^\infty \left(\left(\partial_r \psi\right)^2 + \left(\tfrac{1}{r}\psi\right)^2 \right) r \, dr = \tfrac{1}{2} \ll R \log R.$$

In conclusion, we obtain the lower bound

$$\tfrac{1}{2\pi} \mathcal{I}_{\psi_1} \gtrsim \tfrac{1}{2\sqrt{2}} R \log R.$$

Thus, the upper and lower bound coincide to leading order, so that we gain the asserted scaling behavior (4.41):

$$\mathcal{I}_{\psi_1} \approx \tfrac{\pi}{\sqrt{2}} R \log R.$$

This finishes the asymptotic analysis for ψ_1 and eventually the proof of Proposition 7.

5 Interacting droplets in a reduced configuration space

In the previous chapter, we studied the relevant mechanisms in the coarsening dynamics, namely the *mass exchange* between two immobile droplets and the *migration* of a single droplet in an ambient flux field. Now we are interested in the interaction of both mechanisms in a configuration of N droplets ($N \geq 2$) and their relative importance to the coarsening process. One of the basic questions is how mass exchange influences migration and vice versa. Furthermore, we will give heuristic time scales for both mechanisms, which allow us to identify the dominant coarsening mechanism.

The regime of interest is a configuration of large, well-separated droplets:

$$1 \ll R \sim V^{\frac{1}{d+1}} \ll L. \tag{5.1}$$

Here, we recall that R is the typical radius, V the typical volume of a droplet, and L is the typical distance between droplets. Beside this separation of length scales, we further reduce the configuration space by restricting our analysis to the mesoscopic level. More precisely, we consider mesoscopic droplets as stated in (2.32), which are minimizers of the mesoscopic energy (2.25). The reduction allows us to pass from an infinite- to a finite-dimensional configuration space, which is fully described by the centers and the radii (or volumes, respectively) of the droplets, see Figure 5.1. In the following section, we will review this reduction.

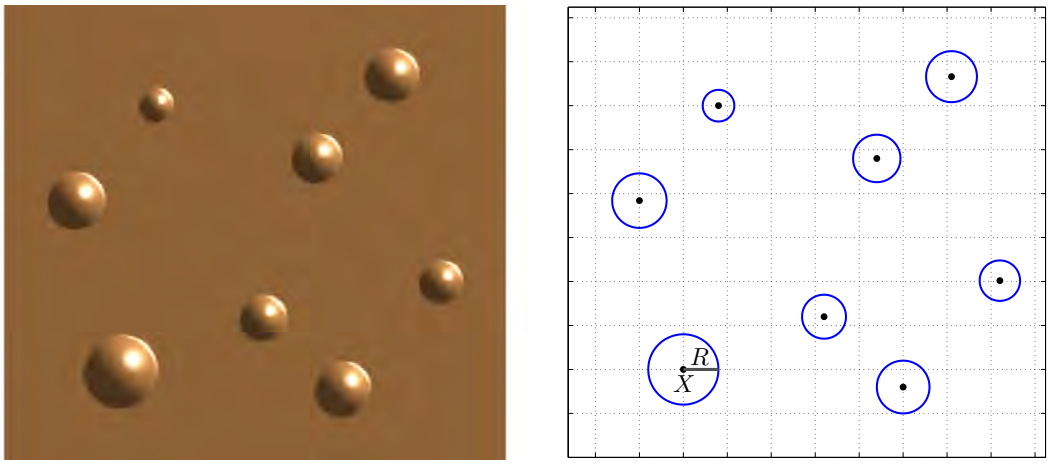

Figure 5.1: Configuration of equilibrium droplets (left) and its reduction to a finite-dimensional configuration space given by radii and centers of droplets (right).

The dynamics of the interacting droplets is determined by the Rayleigh principle (1.24). Let us recall it rephrased in terms of the flux J, see (4.1): At any time the flux J minimizes

$$\mathcal{R}(J) = \frac{1}{2}D(J) + \dot{E}(h).J = \frac{1}{2}\int \frac{1}{m}|J|^2 \, dx + \int \nabla \frac{\delta E}{\delta h} \cdot J \, dx.$$

Then the configuration change is defined by the continuity equation $\partial_t h + \nabla \cdot J = 0$.

The analysis of Chapter 4 reveals that for $q \leq 2$ the migration of droplets to leading order depends only on the mesoscopic droplet profile and not on the details of the potential $\mathcal{U}$. However, in the case $q > 2$ the migration factor depends on the details of $\mathcal{U}$, so that our asymptotic analysis based on the mesoscopic profile gives rise to an error of order 1. Thus, our reduced system of ODEs differs in this case from the actual limiting dynamics by a constant in the migration factor.

First, we introduce the reduction to the finite-dimensional configuration space, which entails the simplified Rayleigh dynamics. Based on the conclusions of the asymptotic analysis of Chapter 4, we present the analysis of the droplet interaction both for one and two dimensions, for clarity at least for a two-droplet configuration. In the one-dimensional case, the results are in agreement with the conclusions of Glasner and Witelski [15, 16], who already studied this case by (different) asymptotic analysis. We finally deduce heuristic time scales for both Ostwald ripening and migration to identify the relative importance of both mechanisms. It turns out that the relative importance depends on the mobility exponent q and the average film height $\overline{H}$.

In traditional Ostwald ripening in binary mixtures as described by the Cahn–Hilliard equation, migration of particles is a much slower process and does not affect the ripening in the regime $L \gg R$. The dynamics of these particles was studied analytically in the sharp-interface limit, i.e. the Mullins–Sekerka free boundary problem, see [1] and [2].

5.1 Reduced structure

Reduced configuration space

According to (2.32a), the parabolic droplets, which are steady states of the mesoscopic energy (2.25), are parametrized by their volume V (above the precursor height) and center X:

$$h_{V,X}(x) = \max\left\{0, -\tfrac{1}{\sqrt{2}\omega} V^{-\frac{1}{d+1}}|x - X|^2 + \tfrac{\omega}{\sqrt{2}} V^{\frac{1}{d+1}}\right\}.$$

Then a configuration of N droplets is fully described by its centers $(X_1^T, \ldots, X_N^T)^T$ with $X_i \in \mathbb{R}^d$ and its volumes $(V_1, \ldots, V_N)^T$, conglomerated in the configuration vector

$$\Theta := (V_1, \ldots, V_N, X_1^T, \ldots, X_N^T)^T \in \mathbb{R}^{(d+1)N}.$$

Let us recall the notation $h_i(x) := h_{V_i,X_i}(x)$, so that the height profile of an ensemble of N mesoscopic droplets is given by $1 + \sum_{i=1}^N h_i(x)$. Furthermore, let us denote the

droplet distances by $L_{ij} := |X_i - X_j|$ and the mobility of a single mesoscopic droplet by $m_i(x) := m(1 + h_i(x))$.

An infinitesimal change of a configuration Θ is described by the infinitesimal change of the droplet volumes and their centers, denoted by $\dot{\Theta}$:

$$\dot{\Theta} := (\dot{V}_1, \dots, \dot{V}_N, \dot{X}_1^T, \dots, \dot{X}_N^T)^T \in \mathbb{R}^{(d+1)N}.$$

Due to the conservation of mass, the change vector $\dot{\Theta}$ is admissible, if $\sum_{i=1}^N \dot{V}_i = 0$, or in other words, if $\dot{\Theta}$ is orthogonal to

$$p = \tfrac{1}{\sqrt{N}}(1_N, 0_{dN})^T.$$

(Here, we use the notation $z_k := (z, \dots, z) \in \mathbb{R}^k$, for $z \in \{0, 1\}$.) The infinitesimal change of the height profile of the configuration corresponding to the change vector $\dot{\Theta}$ is given by

$$\delta h_{\dot{\Theta}} := \sum_{i=1}^N \partial_{V_i} h_i \, \dot{V}_i - \nabla h_i \cdot \dot{X}_i,$$

where

$$\partial_{V_i} h_i(x) = \tfrac{1}{\sqrt{2}(d+1)\omega} \, V_i^{-\frac{d+2}{d+1}} |x - X_i|^2 + \tfrac{\omega}{\sqrt{2}(d+1)} \, V_i^{-\frac{d}{d+1}} \tag{5.2}$$

for $x \in B_{R_i}(X_i)$.

Reduced energy

On the restricted configuration space, the total energy (2.25) of the configuration Θ has the simple form

$$E(\Theta) = \tfrac{\sqrt{2}(d+1)}{\omega} \sum_{i=1}^N V_i^{\frac{d}{d+1}}, \tag{5.3}$$

to which we will refer in the following. In particular, it depends only on the volumes but not on the centers. The infinitesimal change of energy generated by the infinitesimal change of the configuration in the direction of $\dot{\Theta}$ is

$$\dot{E}(\Theta).\dot{\Theta} = \nabla E \cdot \dot{\Theta} = \tfrac{\sqrt{2}d}{\omega} \sum_{i=1}^N V_i^{-\frac{1}{d+1}} \dot{V}_i, \tag{5.4}$$

where $\nabla E \in \mathbb{R}^{(d+1)N}$ stands for the gradient of (5.3) with respect to Θ.

Reduced Rayleigh dynamics

As stated before, the trajectory $t \mapsto \Theta(t)$ of the system is determined by the fact that at any time t the change vector $\dot{\Theta}$ along with the flux J minimize as a pair the Rayleigh functional $\mathcal{R}$ with the infinitesimal change of energy given in (5.4). A variation in J reveals that the minimizing flux is a gradient of a pressure (here denoted by $\varphi_{\dot{\Theta}}$):

$$J = -m \nabla \varphi_{\dot{\Theta}},$$

where the pressure solves

$$\delta h_{\dot\Theta} - \nabla \cdot (m \nabla \varphi_{\dot\Theta}) = 0$$

with boundary condition $\nabla \varphi_{\dot\Theta} \cdot \nu \to 0$ as $|x| \to \infty$. Consequently, one needs to minimize

$$\tfrac{1}{2} \int m |\nabla \varphi_{\dot\Theta}|^2 dx + \nabla E \cdot \dot\Theta \tag{5.5}$$

in order to determine the configuration change $\dot\Theta$.

In the one-dimensional case, we can derive the flux J, which generates the dissipation by explicit integration of the continuity equation. However, in the two-dimensional case it is not possible, so that we fall back to the model pressures examined in the previous chapter. We will see that approximately (at least in the sense that the associated quadratic form of the minimal dissipation, i.e. $D = \int m\,|\nabla \varphi_{\dot\Theta}|^2\,dx$, is well-approximated) the pressure $\varphi_{\dot\Theta}$ is a linear combination of the "decoupled" model pressures, which were introduced in Chapter 4. Let us recall them here (in a slightly modified form):

- *Pressure relevant to droplet motion:* We recall the two auxiliary problems (4.27) and (4.28), where we replace the equilibrium droplet profile by the mesoscopic profile (2.32a).

  We introduce the pressure ψ_0 (generated by a non-zero flux boundary condition far from the droplet) by

  $$\begin{aligned} -\nabla \cdot (m \nabla \psi_0) &= 0, \\ J_0 \cdot \nu \to \tbinom{1}{0} \cdot \nu \text{ as } |x| \to \infty, \qquad &\text{where } J_0 := m \nabla \psi_0, \end{aligned} \tag{5.6}$$

  and the pressure ψ_1, which makes the droplet move with unit speed, by

  $$\begin{aligned} -\partial_1 h_{V,X} - \nabla \cdot (m \nabla \psi_1) &= 0, \\ J_1 \cdot \nu \to 0 \text{ as } |x| \to \infty, \qquad &\text{where } J_1 := -m \nabla \psi_1. \end{aligned} \tag{5.7}$$

  Let us generalize the notation of ψ_1 by accounting for arbitrary distortions $\dot X \in \mathbb{R}^2$ (instead of $(1,0)^T$) of the center X. We denote this pressure by $\psi_1^{\dot X}$, which solves the equation $-\dot X \cdot \nabla h_{V,X} - \nabla \cdot (m \nabla \psi_1^{\dot X}) = 0$. It has a dipolar form:

  $$\psi_1^{\dot X}(x) = \psi_1(r)\ |\dot X|\ \cos\theta \tag{5.8}$$

  in the polar coordinates determined by $r := |x - X|$ and

  $$\frac{x - X}{|x - X|} \cdot \frac{\dot X}{|\dot X|} = \cos\theta.$$

- *Pressure relevant to droplet mass change:* We already introduced the pressure (4.6), which moves the mass 1 from a single mesoscopic droplet into the surrounding precursor film: ψ_V is a radially symmetric solution of

  $$-\partial_V h_{V,0} - \nabla \cdot (m \nabla \psi_V) = 0,$$

and in particular has the form of the fundamental solution outside the droplet, see (4.7).

Since $\varphi_{\dot\Theta}$ depends linearly on the change $\dot\Theta$, the first term in (5.5) defines a quadratic form in $\dot\Theta$. The associated bilinear form is

$$D(\dot\Theta,\dot\Xi) := \int \frac{1}{m}\, J_{\dot\Theta}\cdot J_{\dot\Xi}\, dx = \int m\,\nabla\varphi_{\dot\Theta}\cdot\nabla\varphi_{\dot\Xi}\, dx \tag{5.9}$$

for admissible change vectors $\dot\Theta$ and $\dot\Xi$. Since the space of admissible change vectors is finite-dimensional, there is a symmetric matrix G representing the bilinear form:

$$\dot\Theta^T G\,\dot\Xi = D(\dot\Theta,\dot\Xi).$$

Such matrix G is not unique. The canonical choice is the matrix $\overline{G}$, which also satisfies $\overline{G}\,p = 0$. A symmetric matrix G represents the same bilinear form on the set of admissible change vectors if and only if $\Pi G\Pi = \overline{G}$, where $\Pi = \mathbb{I}\mathrm{d} - pp^T$ is the projection to the orthogonal complement of p.

Minimizing (5.5) in the form $\frac{1}{2}\dot\Theta^T G\dot\Theta + \nabla E\cdot\dot\Theta$ in $\dot\Theta$ with the constraint $\dot\Theta\cdot p = 0$ gives that $\dot\Theta$ is uniquely determined by

$$\begin{aligned}\Pi(G\dot\Theta + \nabla E) &= 0\\ \dot\Theta\cdot p &= 0.\end{aligned} \tag{5.10}$$

The coefficients of G describe the dissipation generated by the fluxes that stem from the mass exchange and droplet migration. For clarity, we subdivide the matrix $G\in\mathbb{R}^{(d+1)N\times(d+1)N}$ into three sub-matrices: the volume change matrix $G^v\in\mathbb{R}^{N\times N}$ with entries G^v_{ij}, the migration matrix $G^m\in\mathbb{R}^{dN\times dN}$ with entries G^m_{ij} and the coupling matrix $C\in\mathbb{R}^{dN\times N}$ with entries C_{ij}:

$$G = \begin{pmatrix} G^v & C^T\\ C & G^m\end{pmatrix}. \tag{5.11}$$

In the following sections, we will give asymptotic expressions of the entries of G in terms of the auxiliary pressures ψ_0, ψ_1 and ψ_V in the regime (5.1) and solve the problem explicitly for a two-droplet configuration both in one and two dimensions.

5.2 Interacting droplets in one dimension

In contrast to the two-dimensional case, the flux J that generates the dissipation can be derived by elementary integration of $\delta h_{\dot{\Theta}} + \partial_x J = 0$ on $\mathbb{R}$ with no-flux boundary conditions $J(-\infty) = J(\infty) = 0$.

5.2.1 Approximate coefficients of G

We show by elementary integration that the coefficient of G can be approximated to leading order in $L \gg V^{\frac{1}{2}}$ by the following expressions:

- *Volume change:*

$$G^v_{ij} = \begin{cases} -\frac{1}{2}L_{ij} + \mathcal{O}(V_i^{\frac{1}{2}}) + \mathcal{O}(V_j^{\frac{1}{2}}), & \text{if } i \neq j, \\ 0, & \text{if } i = j. \end{cases} \tag{5.12}$$

- *Migration:*

$$G^m = \operatorname{diag}(g_1, \ldots, g_N) \tag{5.13}$$

with diagonal entries

$$g_i := \int_{B_{R_i}(X_i)} \frac{1}{m} (h_i)^2 \, dx.$$

- *Coupling:*

$$C = \operatorname{diag}(c_1, \ldots, c_N)\, T, \qquad \text{where } T_{ij} = \begin{cases} 1, & \text{if } i < j, \\ 0, & \text{if } i = j, \\ -1, & \text{if } i > j, \end{cases} \tag{5.14}$$

with diagonal entries

$$c_i := \tfrac{1}{2} \int_{B_{R_i}(X_i)} \frac{1}{m} \, h_i \, dx.$$

It is sufficient to present the approximation of the coefficients of G only for the two-droplet configuration. A consistent generalization to N-droplet configurations is straightforward. Hence, we will consider a configuration $(V_1, V_2, X_1, X_2)^T \in \mathbb{R}^4$, see Figure 5.2, where we set $L := L_{12}$.

Derivation of the volume change matrix G^v

Let the configuration change vector be $w := (1, -1, 0, 0)^T \in \mathbb{R}^4$. Then we have

$$w^T G w = G^v_{11} - G^v_{12} - G^v_{21} + G^v_{22} = \int \frac{1}{m} |J_w|^2 \, dx,$$

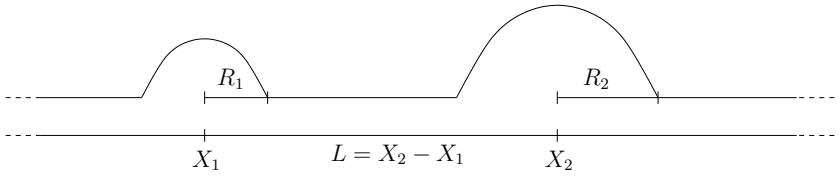

Figure 5.2: Two-droplet configuration in one dimension.

where J_w solves $(\partial_{V_1} h_1 - \partial_{V_2} h_2) + \partial_x J_w = 0$. The above is the only requirement on the coefficients of G^v, which allows us to define

$$\begin{aligned} G^v_{11} &= G^v_{22} := 0, \\ G^v_{12} &= G^v_{21} := -\tfrac{1}{2} \int \frac{1}{m} |J_w|^2 \, dx. \end{aligned}$$

The solution J_w and the leading order behavior of $\int \frac{1}{m} |J_w|^2 \, dx$ were already derived in Section 4.1. Therefore, we immediately obtain the desired coefficients

$$G^v_{12} = G^v_{21} \approx -\tfrac{1}{2} L.$$

For the N-droplet configuration, it is easy to check that the generalized choice $G^v_{ij} = -\frac{1}{2} L_{ij}$ is consistent with this formula.

Derivation of the migration matrix G^m

Let $w_1 := (0, 0, 1, 0)^T$ and $w_2 := (0, 0, 0, 1)^T \in \mathbb{R}^4$. Then we obtain

$$G^m_{ii} = w_i^T G w_i = \int \frac{1}{m} |J_{w_i}|^2 \, dx,$$

where J_{w_i} is a solution of $-\partial_x J_{w_i} = \delta h_{w_i} = -\partial_x h_i$, for $i = 1, 2$. Elementary integration yields $J_{w_i}(x) = h_i(x)$ and thus,

$$G^m_{ii} = \int_{B_{R_i}(X_i)} \frac{1}{m} (h_i)^2 \, dx = g_i.$$

Since J_{w_i} has support in $B_{R_i}(X_i)$, it follows that

$$G^m_{12} = G^m_{21} = \int \frac{1}{m} J_{w_1} \cdot J_{w_2} \, dx = 0.$$

Derivation of the coupling matrix C

For the coupling part we plug in the aforementioned change vectors w, w_1 and w_2. Then we obtain for $i = 1, 2$

$$\begin{aligned} w_i^T G w &= C_{i1} - C_{i2} \\ &= \int \frac{1}{m} J_{w_i} \cdot J_w \, dx, \end{aligned}$$

where $-\partial_x J_{w_i} = -\partial_x h_i$ and $-\partial_x J_w = (\partial_{V_1} h_1 - \partial_{V_2} h_2)$ and therefore,

$$\begin{aligned} &= \int_{B_{R_i}(X_i)} \frac{1}{m} h_i \left(c(x - X_i)^3 + \tilde{c}(x - X_i) - \tfrac{1}{2} \right) dx \\ &= -\tfrac{1}{2} \int_{B_{R_i}(X_i)} \frac{1}{m} h_i \, dx. \end{aligned}$$

This allows us to define

$$\begin{aligned} C_{11} &= C_{22} = 0, \\ C_{12} &= \tfrac{1}{2} \int_{B_{R_1}(X_1)} \frac{1}{m} h_1 \, dx = c_1, \\ C_{21} &= -\tfrac{1}{2} \int_{B_{R_2}(X_2)} \frac{1}{m} h_2 \, dx = -c_2. \end{aligned}$$

5.2.2 Reduced Rayleigh dynamics

System of ODEs for two droplets

Collecting the results of the preceding part, the symmetric matrix G is given by

$$G = \left(\begin{array}{cc|cc} 0 & -\frac{1}{2}L & 0 & -\frac{1}{2}\int \frac{1}{m} h_2 \, dx \\ -\frac{1}{2}L & 0 & \frac{1}{2}\int \frac{1}{m} h_1 \, dx & 0 \\ \hline 0 & \frac{1}{2}\int \frac{1}{m} h_1 \, dx & \int \frac{1}{m} h_1^2 \, dx & 0 \\ -\frac{1}{2}\int \frac{1}{m} h_2 \, dx & 0 & 0 & \int \frac{1}{m} h_2^2 \, dx \end{array} \right) \tag{5.15}$$

to leading order in $V^{\frac{1}{2}} \gg 1$.

According to (5.3), the right hand side is given by $\nabla E = \frac{\sqrt{2}}{\omega}(V_1^{-\frac{1}{2}}, V_2^{-\frac{1}{2}}, 0, 0)^T$. Then due to (5.10), the configuration change $\dot{\Theta} = (\dot{V}_1, \dot{V}_2, \dot{X}_1, \dot{X}_2)^T$ is the solution of the following system of linear ODE:

$$\begin{aligned} G^v_{12}(\dot{V}_2 - \dot{V}_1) - c_2\dot{X}_2 - c_1\dot{X}_1 &= -\frac{\sqrt{2}}{\omega}(V_1^{-\frac{1}{2}} - V_2^{-\frac{1}{2}}), \\ c_1\dot{V}_2 + g_1\dot{X}_1 &= 0, \\ -c_2\dot{V}_1 + g_2\dot{X}_2 &= 0, \\ \dot{V}_1 + \dot{V}_2 &= 0. \end{aligned}$$

In particular, solving the system for the volume change yields

$$\dot{V}_1 = \frac{\sqrt{2}}{\omega} \left(\frac{c_1^2}{g_1} + \frac{c_2^2}{g_2} + 2G^v_{12} \right)^{-1} (V_1^{-\frac{1}{2}} - V_2^{-\frac{1}{2}}),$$

and for the migration

$$\dot{X}_1 = \frac{c_1}{g_1}\,\dot{V}_1.$$

Note that in the regime $L \gg V_i^{\frac{1}{2}}$ we obtain $G^v_{12} \gg \frac{c_1^2}{g_1} + \frac{c_2^2}{g_2}$ according to the estimates on the coefficients from (4.21) and (4.22), so that to leading order

$$\left(\frac{c_1^2}{g_1} + \frac{c_2^2}{g_2} + 2G^v_{12}\right) \approx 2G^v_{12} \approx -L.$$

Therefore, the reduced Rayleigh dynamics for two droplets in the one-dimensional case is given by the following system:

Volume change: $$\dot{V}_1 = \frac{\sqrt{2}}{\omega}\,L^{-1}\,(V_2^{-\frac{1}{2}} - V_1^{-\frac{1}{2}}), \qquad \dot{V}_2 = -\dot{V}_1. \tag{5.16}$$

Migration: $$\dot{X}_1 = \frac{\int \frac{1}{m}\,h_1\,dx}{\int \frac{1}{m}\,h_1^2\,dx}\,\dot{V}_1, \qquad \dot{X}_2 = \frac{\int \frac{1}{m}\,h_2\,dx}{\int \frac{1}{m}\,h_2^2\,dx}\,\dot{V}_1. \tag{5.17}$$

System of ODEs for N-droplet configuration

To determine the dynamics for the N-droplet configuration in a transparent form, assume that $X_i < X_{i+1}$ for all $i = 1, \dots, N-1$. Let us use the notation $\dot{V} := (\dot{V}_1, \dots, \dot{V}_N)^T$ and $\dot{X} := (\dot{X}_1, \dots, \dot{X}_N)^T$. Then the equations of the dynamics are

$$\begin{gathered}(\mathbb{I}\mathrm{d} - pp^T)(G^v\dot{V} + C^T\dot{X}) = -(\mathbb{I}\mathrm{d} - pp^T)\nabla E \\ C\dot{V} + G^m\dot{X} = 0.\end{gathered}$$

Here, p has been restricted to its first N coordinates. It follows that

$$\dot{X} = -\mathrm{diag}\,\left(\frac{c_1}{g_1}, \dots, \frac{c_N}{g_N}\right) T\dot{V}. \tag{5.18}$$

Furthermore, we observe in the regime $L \gg V^{\frac{1}{2}}$ that

$$C(G^m)^{-1}C^T \ll G^v$$

as for two droplets. Therefore, we obtain the following approximation of the first equation by substituting (5.18):

$$(\mathbb{I}\mathrm{d} - pp^T)G^v\dot{V} = -(\mathbb{I}\mathrm{d} - pp^T)\nabla E, \tag{5.19}$$

provided $L_{ij} \gg V_k^{\frac{1}{2}} \gg 1$ for $i, j, k = 1, \dots, N$, $i \neq j$.

The remainder of this section is devoted to find a solution of this equation with $\sum_{i=1}^{N} \dot{V} = 0$. For this purpose, note that the submatrix G^v has the form of a Green's function in one dimension: The i-th entry of the product $G^v \dot{V}$, i.e.

$$-\tfrac{1}{2} \sum_{j \neq i} |X_i - X_j| \, \dot{V}_j,$$

realizes the superposition of potentials in X_i generated by "mass sources" at X_j with masses $\dot{V}_j$. Thus, it is reasonable that equation (5.19) can be solved by applying a discrete Laplace operator D, which has the form of a tridiagonal matrix:

$$D_{ij} := \begin{cases} \frac{1}{L_{i-1\,i}}, & \text{if } j = i-1, \\ -\left(\frac{1}{L_{i-1\,i}} + \frac{1}{L_{i\,i+1}} \right), & \text{if } j = i, \\ \frac{1}{L_{i\,i+1}}, & \text{if } j = i+1, \\ 0, & \text{else,} \end{cases}$$

with no-flux condition at the boundary. Here, we use the convention $L_{0\,1} = L_{N\,N+1} = \infty$. Note that $D(\mathbb{I}\mathrm{d} - pp^T) = D$.

Indeed, a direct calculation of $-DG^v$ based on the relation $L_{i\,j+1} = L_{i\,j} + L_{j\,j+1}$ yields

$$-DG^v = \tfrac{1}{2} \begin{pmatrix} 1 & -1 & \dots & \dots & -1 \\ & 2 & & & \\ & & \ddots & & \\ & & & 2 & \\ -1 & \dots & \dots & -1 & 1 \end{pmatrix},$$

and finally, using the conservation of volume $\sum_{i=1}^{N} \dot{V}_i = 0$, the identity

$$-DG^v \dot{V} = \dot{V}.$$

Applying the same transformation to the right hand side gives for $i = 1, \dots, N$

$$\frac{(\nabla E)_{i+1} - (\nabla E)_i}{L_{i\,i+1}} - \frac{(\nabla E)_i - (\nabla E)_{i-1}}{L_{i-1\,i}} = \frac{\sqrt{2}}{\omega} \left(\frac{V_{i+1}^{-\frac{1}{2}} - V_i^{-\frac{1}{2}}}{L_{i\,i+1}} - \frac{V_i^{-\frac{1}{2}} - V_{i-1}^{-\frac{1}{2}}}{L_{i-1\,i}} \right).$$

Hence, we obtain the equation for the volume change given by (5.19):

$$\dot{V}_i = \frac{\sqrt{2}}{\omega} \left(\frac{V_{i+1}^{-\frac{1}{2}} - V_i^{-\frac{1}{2}}}{L_{i\,i+1}} - \frac{V_i^{-\frac{1}{2}} - V_{i-1}^{-\frac{1}{2}}}{L_{i-1\,i}} \right). \tag{5.20}$$

To determine $\dot{X}$, we use (5.18). It follows from (5.20) that

$$\dot{X}_i = \frac{\sqrt{2}}{\omega} \frac{\int \frac{1}{m} h_i dx}{\int \frac{1}{m} h_i^2 dx} \left(\frac{V_i^{-\frac{1}{2}} - V_{i-1}^{-\frac{1}{2}}}{L_{i-1\,i}} + \frac{V_{i+1}^{-\frac{1}{2}} - V_i^{-\frac{1}{2}}}{L_{i\,i+1}} \right). \tag{5.21}$$

It is straightforward to check that equations (5.20) and (5.21) indeed coincide with the equations of motion and pressure change proposed by Glasner and Witelski in [15]. To switch between the volume and the pressure one applies the relation (2.34).

5.3 Interacting droplets in two dimensions

5.3.1 Approximate coefficients of G

In the following, we will show that the coefficients of G can be approximated by the auxiliary model pressures in the following way:

- *Volume change:*

$$\begin{aligned} G^v_{ij} &= \begin{cases} -\frac{1}{2}\left(\int_{B_L(0)} m|\nabla\psi_{V_i}|^2\,dx + \int_{B_L(0)} m|\nabla\psi_{V_j}|^2\,dx\right) + \mathcal{O}(1), & \text{if } i \neq j, \\ 0, & \text{else,} \end{cases} \\ &\approx \begin{cases} -\frac{1}{4\pi}\left(\log(L_{ij}/V_i^{\frac{1}{3}}) + \log(L_{ij}/V_j^{\frac{1}{3}})\right), & \text{if } i \neq j, \\ 0, & \text{else.} \end{cases} \end{aligned} \tag{5.22}$$

  The auxiliary pressure ψ_{V_i} relevant to mass exchange is defined in (4.6).

- *Migration:*

$$G^m_{ij} = \begin{cases} \operatorname{diag}(g_i, g_i) + \mathcal{O}(g_i)_{2\times 2}, & \text{if } i = j, \\ \mathcal{O}(\sqrt{g_i g_j})_{2\times 2}, & \text{else,} \end{cases} \tag{5.23}$$

  where the diagonal entries are

$$g_i = \int m_i\,|\nabla\psi_1|^2\,dx, \tag{5.24}$$

  and the error term is defined by $\mathcal{O}(f)_{2\times 2} := \begin{pmatrix} \mathcal{O}(f) & \mathcal{O}(f) \\ \mathcal{O}(f) & \mathcal{O}(f) \end{pmatrix}$. The pressure ψ_1 relevant to droplet motion solves $-\partial_1 h_1 - \nabla\cdot(m_i\nabla\psi_1) = 0$ as defined in (5.7).

- *Coupling:*

$$C_{ij} = \begin{cases} \frac{X_i - X_j}{|X_i - X_j|}\,c_{ij} + \mathcal{O}(c_{ij})_{2\times 1}, & \text{if } i \neq j, \\ 0, & \text{else,} \end{cases} \tag{5.25}$$

  where the coefficients are defined by

$$c_{ij} = \frac{1}{2\pi}\frac{1}{|X_i - X_j|}\int \partial_1 h_i\,\psi_0\,dx. \tag{5.26}$$

  The pressure ψ_0 is determined by (5.6).

The leading order scaling behavior of (5.24) and (5.26) was identified in the preceding chapter in (4.40) and (4.41).

Again, we present the details of the leading order derivation of coefficients of G only for a configuration of two droplets. It contains all the essential ingredients of the derivation with N droplets, but is significantly easier to present. Hence, let us consider a configuration of two droplets, $\Theta = (V_1, V_2, X_1^T, X_2^T)^T$, with distance $L = |X_2 - X_1|$.

Derivation of the volume change matrix G^v

Consider the general mass exchange given by the change vector $w = (\dot{V}_1, \dot{V}_2, 0_4)^T$ with $\dot{V}_1 + \dot{V}_2 = 0$. Then the profile distortion is

$$\delta h_w = \dot{V}_1 \, \partial_{V_1} h_1 + \dot{V}_2 \, \partial_{V_2} h_2 = \dot{V}_1 (\partial_{V_1} h_1 - \partial_{V_2} h_2).$$

By the definition of the dissipation rate (5.9), it follows that

$$G^v_{11}(\dot{V}_1)^2 + G^v_{22}(\dot{V}_2)^2 + 2G^v_{12}\dot{V}_1 \, \dot{V}_2 = w^T G w = \int m |\nabla \varphi_w|^2 \, dx,$$

where $\delta h_w - \nabla \cdot (m \nabla \varphi_w) = 0$ and $\nabla \varphi_w \cdot \nu \to 0$ as $|x| \to \infty$. The above condition fully determines the volume exchange part of the bilinear form D, but as we discussed before, the matrix G is not unique. Since we think of dissipation due to mass exchange, we choose the matrix G^v for which $G^v_{11} = G^v_{22} = 0$. Accordingly, we get

$$2G^v_{12} \, \dot{V}_1 \dot{V}_2 = -2G^v_{12} \, (\dot{V}_1)^2 = \int m |\nabla \varphi_w|^2 \, dx.$$

To determine the value on the right hand side, we only have to refer to the asymptotic results gained in the study of the model pressure relevant for mass exchange, see (4.10) in Section 4.1. In this part, we have shown that φ_w is in a sense well-approximated by

$$-\dot{V}_1 \, \psi_{V_1}(\cdot - X_1) - \dot{V}_2 \, \psi_{V_2}(\cdot - X_2).$$

Hence, we immediately get the claimed scaling behavior.

Derivation of the migration matrix G^m

Let $\dot{X}, \dot{Y} \in \mathbb{R}^2$. Consider the change vectors $w_1 := (0_2, \dot{X}^T, 0_2)^T$ and $w_2 := (0_2, \dot{Y}^T, 0_2)^T$, which both perturb the location of X_1. By the definition of the dissipation rate (5.9),

$$\dot{X}^T G^m_{11} \dot{Y} = \int m \, \nabla \varphi_{w_1} \cdot \nabla \varphi_{w_2} \, dx,$$

where $-\dot{X} \cdot \nabla h_1 - \nabla \cdot (m \nabla \varphi_{w_1}) = 0$ and $-\dot{Y} \cdot \nabla h_1 - \nabla \cdot (m \nabla \varphi_{w_2}) = 0$ and $\nabla \varphi_{w_i} \cdot \nu \to 0$ as $|x| \to \infty$.

The difference between φ_{w_1} and $\psi_1^{\dot{X}}$ defined in (5.7) originates from the different mobilities: $\psi_1^{\dot{X}}$ solves the same problem as φ_{w_1}, but with m replaced by the mobility m_1 for the single mesoscopic droplet h_1. However, we expect that φ_{w_1} can be well-approximated by $\psi_1^{\dot{X}}$ to leading order in the regime $L \gg R$, so that we can replace φ_{w_1} by $\psi_1(|x - X_1|) \frac{x - X_1}{|x - X_1|} \cdot \dot{X}$.

For further calculations, the following identity is helpful: Let $\xi \in C([0, \infty), [0, \infty))$ and $\int_0^\infty \xi(r) r^3 dr < \infty$. Then it holds that

$$\int \xi(|x|)(\dot{X} \cdot x)(\dot{Y} \cdot x) \, dx = \frac{\dot{X} \cdot \dot{Y}}{2} \int \xi(|x|) \, |x|^2 \, dx.$$

It is verified by elementary calculation, e.g. via transformation in polar coordinates.

Now we are in the position to derive the coefficient based on the approximation described above:

$$\begin{aligned}
\dot{X}^T G_{11}^m \dot{Y} &= \int \varphi_{w_1} \nabla h_1 \cdot \dot{Y} \, dx \\
&\approx \int \left(\psi_1(|x - X_1|) \frac{x - X_1}{|x - X_1|} \cdot \dot{X} \right) \left(\nabla h_1 \cdot \dot{Y} \right) \, dx \\
&= \frac{\dot{X} \cdot \dot{Y}}{2} \int \psi_1(|x - X_1|) \frac{x - X_1}{|x - X_1|} \cdot \partial_r h_1(|x - X_1|) \frac{x - X_1}{|x - X_1|} \, dx \\
&= \dot{X} \cdot \dot{Y} \int \psi_1(|x - X_1|) \frac{x_1 - X_1^{(1)}}{|x - X_1|} \, \partial_r h_1(|x - X_1|) \frac{x_1 - X_1^{(1)}}{|x - X_1|} \, dx \\
&= \dot{X} \cdot \dot{Y} \int \psi_1(|x - X_1|) \frac{x_1 - X_1^{(1)}}{|x - X_1|} \, \partial_1 h_1 \, dx \\
&= \dot{X} \cdot \dot{Y} \int m_1 |\nabla \psi_1|^2 \, dx.
\end{aligned} \tag{5.27}$$

Here, we use that h_1 is a radially symmetric function w.r.t. X. Hence, we finally obtain that $G_{11}^m \approx \operatorname{diag}(g_1, g_1)$ with

$$g_1 = \int m_1 |\nabla \psi_1|^2 dx.$$

The coefficient $G_{22}^m \approx \operatorname{diag}(g_2, g_2)$ is analogously computed with the same approximation argument. Furthermore, the off-diagonal element G_{12}^m is of lower order compared to the diagonal entries to leading order: Consider the change vectors $w_1 := (0_2, \dot{X}^T, 0_2)^T$ and $w_2 := (0_4, \dot{Y}^T)^T$, which perturb the location X_1 and X_2, respectively. Then we find in the regime $L \gg R \sim V^{\frac{1}{3}}$

$$\begin{aligned}
\left| \dot{X}^T G_{12}^m \dot{Y} \right| &= \left| \int \varphi_{w_1} \nabla h_2 \cdot \dot{Y} \, dx \right| \\
&\approx \left| \int \psi_1(|x - X_1|) \frac{x - X_1}{|x - X_1|} \cdot \dot{X} \, \nabla h_2 \cdot \dot{Y} \, dx \right| \\
&\approx L^{-1} |\dot{X}| \left| \int_{B_{R_2}(X_2)} \nabla h_2 \cdot \dot{Y} \, dx \right| \\
&\lesssim |\dot{X}| \, |\dot{Y}| \, V_2^{\frac{1}{3}} L^{-1} \\
&\ll |\dot{X}| \, |\dot{Y}|,
\end{aligned}$$

which is small compared to $|\dot{X}| \, |\dot{Y}| o(\sqrt{g_1 g_2})$ in the regime $V^{\frac{1}{3}} \gg 1$. Note that we use the asymptotic behavior of ψ_1 far away from $B_{R_1}(X_1)$ as stated in (4.35) in Lemma 11.

Derivation of the coupling matrix C

To analyze the interaction of volume change and migration, consider the change vectors $w_1 := (0_2, \dot{X}^T, 0_2)^T$ and $w_2 := (1, -1, 0_4)^T$. Again, we expect that φ_{w_1} is well-

approximated by the model pressure $\psi_1^{\dot{X}}$ to leading order in $L \gg R$:

$$\begin{aligned}
\dot{X}^T[C_{11}, C_{12}]\begin{pmatrix}1\\-1\end{pmatrix} &= \int m\nabla\varphi_{w_1}\cdot\nabla\varphi_{w_2}\,dx \\
&= -\int \varphi_{w_1}\left(\partial_{V_1}h_1 - \partial_{V_2}h_2\right)\,dx \\
&\approx -\int \psi_1^{\dot{X}}\left(\partial_{V_1}h_1 - \partial_{V_2}h_2\right)\,dx \qquad (5.28)\\
&= \int_{B_{R_2}(X_2)} \psi_1(|x-X_1|)\frac{x-X_1}{|x-X_1|}\cdot\dot{X}\,\partial_{V_2}h_2\,dx \qquad (5.29)\\
&\approx \psi_1(|X_2-X_1|)\frac{X_2-X_1}{|X_2-X_1|}\cdot\dot{X}\int_{B_{R_2}(X_2)}\partial_{V_2}h_2\,dx \\
&= \psi_1(|X_2-X_1|)\frac{X_2-X_1}{|X_2-X_1|}\cdot\dot{X}.
\end{aligned}$$

Note that we in particular exploit the fact that $\frac{x-X_1}{|x-X_1|}\cdot\dot{X}$ is an odd function w.r.t. the center X_1. Thus, we get

$$C_{11} - C_{12} \approx \psi_1(|X_2-X_1|)\,\frac{X_2-X_1}{|X_2-X_1|} \approx \lim_{r\to\infty} r\,\psi_1(r)\,\frac{X_2-X_1}{|X_2-X_1|^2}.$$

As above, this is the only requirement on C_{11} and C_{12}. We set $C_{11} = 0$ and finally have

$$C_{12} \approx -\lim_{r\to\infty} r\,\psi_1(r)\,\frac{X_2-X_1}{|X_2-X_1|^2} \approx \frac{1}{2\pi}\frac{1}{|X_1-X_2|}\int \partial_1 h_1\,\psi_0\,dx\,\frac{X_1-X_2}{|X_1-X_2|}$$

due to the asymptotic behavior (4.36). The approximation of C_{21} is treated analogously.

5.3.2 Reduced Rayleigh dynamics

First, let us recall the leading order scaling relations for the coefficients of G: For $i \neq j$

$$G_{ij}^v \approx -\frac{1}{4\pi}\left(\log(L_{ij}/V_i^{\frac{1}{3}}) + \log(L_{ij}/V_j^{\frac{1}{3}})\right), \qquad (5.30)$$

$$g_i \approx \begin{cases} C\,V_i^{\frac{4-q}{3}} & \text{for } q\in[0,3),\\ \frac{\pi^{\frac{2}{3}}}{3}\,V_i^{\frac{1}{3}}\,\log V_i & \text{for } q=3,\\ C\,V_i^{\frac{1}{3}} & \text{for } q>3,\end{cases} \qquad (5.31)$$

$$c_{ij} \approx -\frac{1}{L_{ij}}\begin{cases} C\,V_i^{\frac{3-q}{3}} & \text{for } q\in[0,2),\\ \frac{1}{3\pi^{\frac{4}{3}}}\,V_i^{\frac{1}{3}}\,\log V_i & \text{for } q=2,\\ C\,V_i^{\frac{1}{3}} & \text{for } q>2.\end{cases} \qquad (5.32)$$

The leading order values of g_i and c_{ij} follow from (4.40) and (4.41).

System of ODEs for two droplets

As an insightful illustration, we consider the particular case of two droplets in detail. Let us compute the equations for $\dot{\Theta}$ in the natural coordinates $\{e_1, e_2\}$ for the two-droplet configuration:

$$e_1 = \frac{X_2 - X_1}{|X_2 - X_1|}, \qquad e_2 \perp e_1,\ |e_2| = 1. \tag{5.33}$$

The characterization of G given in (5.22)-(5.26) yields

$$G = \left(\begin{array}{cc|cccc} 0 & G^v_{12} & 0 & 0 & c_{21} & 0 \\ G^v_{12} & 0 & -c_{12} & 0 & 0 & 0 \\ \hline 0 & -c_{12} & g_1 & 0 & 0 & 0 \\ 0 & 0 & 0 & g_1 & 0 & 0 \\ c_{21} & 0 & 0 & 0 & g_2 & 0 \\ 0 & 0 & 0 & 0 & 0 & g_2 \end{array}\right).$$

According to (5.10), we obtain that the reduced Rayleigh dynamics is given by the following system of ODEs:

$$\begin{aligned} -G^v_{12}\dot{V}_1 + G^v_{21}\dot{V}_2 + c_{12}\dot{X}^{(1)}_1 + c_{21}\dot{X}^{(1)}_2 &= -\frac{2\sqrt{2}}{\omega}(V_1^{-\frac{1}{3}} - V_2^{-\frac{1}{3}}), \\ g_1\dot{X}^{(1)}_1 - c_{12}\dot{V}_2 &= 0, \\ \dot{X}^{(2)}_1 &= 0, \\ g_2\dot{X}^{(1)}_2 + c_{21}\dot{V}_1 &= 0, \\ \dot{X}^{(2)}_2 &= 0, \\ \dot{V}_1 + \dot{V}_2 &= 0. \end{aligned}$$

In particular, we have

$$\dot{V}_1 = \frac{2\sqrt{2}}{\omega}\left(2G^v_{12} + \frac{c^2_{12}}{g_1} + \frac{c^2_{21}}{g_2}\right)^{-1}(V_1^{-\frac{1}{3}} - V_2^{-\frac{1}{3}}). \tag{5.34}$$

Using (5.30), (5.31) and (5.32), the assumption $L_{12} \gg V_i^{\frac{1}{3}}$ for $i = 1, 2$ yields

$$-G^v_{12} \gg 1 \gg \frac{c^2_{12}}{g_i}.$$

Therefore, the reduced Rayleigh dynamics for two droplets in the two-dimensional case is determined to leading order by the following system:

Volume change:

$$\dot{V}_1 = -\frac{4\pi^{\frac{4}{3}}}{\log(L/V_1^{\frac{1}{3}}) + \log(L/V_2^{\frac{1}{3}})} \left(V_1^{-\frac{1}{3}} - V_2^{-\frac{1}{3}}\right), \qquad (5.35)$$
$$\dot{V}_2 = -\dot{V}_1.$$

Migration:

$$\dot{X}_1^{(1)} = -\tfrac{1}{2\pi} L^{-1} \frac{\int \partial_1 h_1 \, \psi_0 \, dx}{\int m_1 |\nabla \psi_1|^2 \, dx} \, \dot{V}_1, \qquad (5.36)$$
$$\dot{X}_2^{(1)} = -\tfrac{1}{2\pi} L^{-1} \frac{\int \partial_1 h_2 \, \psi_0 \, dx}{\int m_2 |\nabla \psi_1|^2 \, dx} \, \dot{V}_1.$$

The equations (5.36) for the motion of the droplets provide a nice way of interpreting the connection between J_∞ in the model problem in Section 4.2 and the case of a configuration of droplets with at least two droplets. For this purpose, consider the equation (5.36) in standard Euclidean coordinates:

$$\begin{aligned} \dot{X}_1 &= -\frac{\dot{V}_2}{g_1} C_{12} \\ &= \frac{\int \partial_1 h_1 \, \psi_0 \, dx}{\int m_1 |\nabla \psi_1|^2 \, dx} \left(-\frac{\dot{V}_2}{2\pi} \frac{X_1 - X_2}{|X_1 - X_2|^2} \right) \\ &= \frac{\int \partial_1 h_1 \, \psi_0 \, dx}{\int m_1 |\nabla \psi_1|^2 \, dx} \left(-\nabla \left(\frac{\dot{V}_2}{2\pi} \log |x - X_2| \right) \Big|_{x = X_1} \right), \end{aligned} \qquad (5.37)$$

and compare it to (4.37) in Section 4.2. It reveals that in the context of a two-droplet configuration, J_∞ can be interpreted as the flux $-\dot{V}_2 \nabla \psi_{V_2}(X_1 - X_2)$ at X_1 generated by the harmonic potential $\dot{V}_2 \psi_{V_2}(. - X_2)$, which transports mass $\dot{V}_2$ out of the droplet centered in X_2. In conclusion, migration is slaved to Ostwald ripening.

Furthermore, the equations reveal that both droplets move in the direction of the smaller one: Assume that $V_1 < V_2$, which implies $\dot{V}_1 < 0$ due to (5.35). Then it also holds that $\dot{X}_1^{(1)} < 0$ (and similarly $\dot{X}_2^{(1)} < 0$), since the migration factor $-\frac{\int \partial_1 h_1 \, \psi_0 \, dx}{\int m_1 |\nabla \psi_1|^2 \, dx}$ is positive. However, the larger droplet will never reach the smaller one, as the migration factor is smaller for larger R, see e.g. (4.42). Figure 6.21 (bottom) shows a typical chase of two isolated droplets.

The results of *Pismen and Pomeau* in [33] significantly differ from our findings, namely in the sign of the velocity. They claim for a two-droplet configuration that both droplets "migrate in the direction of the larger droplet", see Equation (38) in [33], as opposed to our results. Since they also find that smaller droplets are faster, they argue that the smaller droplets might catch up to larger ones causing collision. This implies a completely different understanding of the impact of migration for the coarsening process.

5.4 Heuristic time scales in the reduced dynamics

The reduced dynamics of a two-droplet configuration, namely (5.16) and (5.17) for $d = 1$ and (5.35) and (5.36) for $d = 2$, allows us to deduce heuristically the typical time scale for Ostwald ripening and migration in terms of the typical volume V and the typical distance L in the regime $L \gg V^{\frac{1}{d+1}}$. Here, we assume that the typical lengths exhibit scaling in time. In addition to the scaling in V, we further investigate how the time scales depend on the average film height $\overline{H}$ (up to logarithmic corrections). By mass conservation, we have the relation

$$\overline{H} L^d \sim V \tag{5.38}$$

for arbitrary dimension d.

Time scale for Ostwald ripening

For Ostwald ripening, we obtain from (5.16) and (5.35)

$$\begin{aligned} \dot{V} &\sim \begin{cases} L^{-1} V^{-\frac{1}{2}} & \text{for } d = 1, \\ (\log L)^{-1} V^{-\frac{1}{3}} & \text{for } d = 2. \end{cases} \\ &\overset{(5.38)}{\sim} \begin{cases} \overline{H} V^{-\frac{3}{2}} & \text{for } d = 1, \\ (\log V)^{-1} V^{-\frac{1}{3}} & \text{for } d = 2. \end{cases} \end{aligned}$$

Note that we neglect the logarithmic correction term in $\overline{H}$ for the two-dimensional case. Hence, the time scale for ripening is

$$\tau_{\text{rip}} \sim \frac{V}{\dot{V}} \sim \begin{cases} \overline{H}^{-1} V^{\frac{5}{2}} & \text{for } d = 1, \\ \log V \, V^{\frac{4}{3}} & \text{for } d = 2. \end{cases} \tag{5.39}$$

Time scale for migration

For migration, equations (5.17) and (5.36) imply the scaling

$$\dot{L} \sim |\dot{X}| \sim \mathfrak{mig}(V) \, L^{-1} \dot{V} \sim \mathfrak{mig}(V) \begin{cases} L^{-1} \, V^{-\frac{1}{2}} & \text{for } d = 1, \\ L^{-1} (\log L)^{-1} V^{-\frac{1}{3}} & \text{for } d = 2. \end{cases}$$

Hence, we obtain

$$\begin{aligned} \tau_{\text{mig}} \sim \frac{L}{\dot{L}} &\sim \mathfrak{mig}(V)^{-1} \begin{cases} L^2 \, V^{\frac{1}{2}} & \text{for } d = 1, \\ L^2 \log L \, V^{\frac{1}{3}} & \text{for } d = 2. \end{cases} \\ &\sim \mathfrak{mig}(V)^{-1} \begin{cases} \overline{H}^{-2} \, V^{\frac{5}{2}} & \text{for } d = 1, \\ \overline{H}^{-1} \, (\log V) V^{\frac{4}{3}} & \text{for } d = 2. \end{cases} \end{aligned}$$

The role of migration

The relative importance of migration can be deduced from the quotient of the time scales:

$$\frac{\tau_{\mathrm{mig}}}{\tau_{\mathrm{rip}}} \sim \mathfrak{mig}(V)^{-1}\,\overline{H}^{-1}.$$

The scaling of the migration factor in terms of V is determined by the asymptotic leading order values of g and c as stated in (5.31) and (5.32). Hence, we finally deduce the role of migration in terms of scaling in V and $\overline{H}$:

Role of migration:

$$\frac{\tau_{\mathrm{mig}}}{\tau_{\mathrm{rip}}} \sim \overline{H}^{-1} \begin{cases} V^{\frac{1}{d+1}} & \text{for } q \in [0,2), \\ (\log V)^{-1} V^{\frac{1}{d+1}} & \text{for } q = 2, \\ V^{\frac{3-q}{d+1}} & \text{for } q \in (2,3), \\ \log V & \text{for } q = 3, \\ 1 & \text{for } q > 3. \end{cases} \tag{5.40}$$

We argue in the introduction that migration generically leads to collision. Hence, these heuristics indicate the following:

- For $q < 3$, collapse eventually is the dominant mechanism, since the typical volume of a droplet increases during coarsening. In particular, droplets are nearly stationary in the long-time behavior.
- For $q > 3$, the average film height $\overline{H}$ sets the relative importance of migration for all times in terms of scaling (up to a logarithm for $q = 3$). In particular, the coarsening process for a configuration of large average height is collision-dominated.

An additional numerical study in Section 6.3.3 further enlightens the role of migration for coarsening by collision in the two-dimensional case. For the one-dimensional case, Glasner and Witelski [16] identified collision-dominated regimes in terms of the average film height by means of numerical parameter studies.

6 Numerics for thin liquid films

In this chapter, we will present the discretization of both the thin-film equation (1.1) and the reduced Rayleigh dynamics (5.10), and conduct several numerical test, which support our analytical results of the previous chapters.

6.1 Discretization of the thin-film equation

The thin-film equation (1.1) has a structure like the Cahn–Hilliard-type equation treated in [27]. Hence, we use an equivalent discretization scheme, which is guided by the following two features of the continuous problem:

- mass conservation (1.4): $\frac{d}{dt}\int h\,dx = 0$.
- energy decrease (1.5): $\frac{d}{dt}E(h) = -\int \frac{1}{m(h)}|J|^2\,dx \leq 0$.

The scheme is natural in the sense that it relies on the gradient flow structure of the problem as we will see in the following subsection.

For our numerical experiments, we apply either no-flux and equilibrium boundary conditions as stated in the original problem (1.1) or periodic boundary conditions in all spatial directions, respectively. As the intermolecular potential $\mathcal{U}$, we choose the special form

$$\mathcal{U}(h) := 2h^{-3} - 3h^{-2} + 1, \tag{6.1}$$

which was also used in [15]. The choice for the initial values depends on the numerical experiments we conduct.

6.1.1 Time discretization

Let $\{t_k\}_{k=0}^K$ be an equidistant finite partition of the time interval $[0,T]$ of step size $\tau := t_{k+1} - t_k$. For shortness, we denote by $h^k := h(t_k)$ and $J^k := J(t_k)$ the numerical solutions at time t_k.

Symmetric semi-implicit Euler scheme

The gradient flow structure of the thin-film equation as introduced in Section 3.2 gives us a natural way for a semi-implicit time discretization, see [10], which is stable in the sense that the discrete energy is non-increasing. This scheme is characterized by a minimization problem: For a given h^k, the solution h^{k+1} is determined by

$$h^{k+1} = \arg\min_{h\in\mathcal{M}} \left\{ \frac{1}{2\tau} d(h,h^k) + E(h) \right\}. \tag{6.2}$$

The distance d on the manifold is defined in (3.4). As an immediate consequence, the energy is non-increasing:

$$E(h^{k+1}) \leq \frac{1}{2\tau} d(h^{k+1}, h^k) + E(h^{k+1}) \leq \frac{1}{2\tau} d(h^k, h^k) + E(h^k) = E(h^k).$$

To avoid solving the non-linear, nested minimization problem (6.2), let us work with a quadratic approximation. We write $h := h^k + \tau\delta h$. Then, we reformulate (6.2) with the help of the leading order approximations

$$d(h, h^k)^2 \approx \tau^2 g_{h^k}(\delta h, \delta h),$$

and

$$E(h) \approx E(h^k) + \tau \operatorname{diff} E_{h^k}.\delta h + \frac{\tau^2}{2} g_{h^k}(\delta h, \operatorname{Hess} E_{h^k} \delta h)$$

as a minimization problem in terms of the change δh:

$$\delta h^* = \arg \min_{\delta h \in T_{h^k}\mathcal{M}} \left\{ \frac{\tau}{2} g_{h^k}(\delta h, \delta h) + E(h^k) + \tau \operatorname{diff} E_{h^k}.\delta h + \frac{\tau^2}{2} g_{h^k}(\delta h, \operatorname{Hess} E_{h^k} \delta h) \right\}.$$

Then we update h^k via $h^{k+1} = h^k + \tau\delta h^*$.

Of course, the rephrased problem still includes a minimization problem according to the definition of the metric tensor g. The remedy is to refer to the lifted gradient flow evolution as stated in the remark of Section 3.2 (rephrased in terms of the flux $J = hu$). According to this, one can easily verify that it is equivalent to seek the minimizer

$$J^{k+1} = \arg\min_J \left\{ \frac{1}{2} \int \frac{1}{m(h^k)} |J|^2 \, dx + \int \nabla \frac{\delta E}{\delta h}(h^k) \cdot J \, dx \right. \\ \left. + \frac{\tau}{2} \int |\nabla\nabla \cdot J|^2 + \mathcal{U}''(h^k)(\nabla \cdot J)^2 \, dx \right\} \quad (6.3)$$

and update $h^{k+1} = h^k - \tau\nabla \cdot J^{k+1}$.

Writing down the Euler–Lagrange equation of (6.3) together with the continuity equation, we obtain the semi-implicit Euler scheme

$$\left[\frac{1}{m(h^k)} \mathbb{I}\mathrm{d} + \tau\nabla(\Delta - \mathcal{U}''(h^k))\nabla\cdot \right] J^{k+1} = -\nabla \frac{\delta E}{\delta h}(h^k), \quad (6.4a)$$

$$h^{k+1} = h^k - \tau\nabla \cdot J^{k+1}. \quad (6.4b)$$

This scheme is semi-implicit in the sense that the base point of the metric is treated explicitly. One benefit of this natural discretization is the symmetry of the fourth-order operator.

6.1.2 Spatial discretization

We discretize the divergence and the gradient operator such that the following two features are kept:

- mass conservation of the continuous problem, see (1.4),
- symmetry of the fourth-order operator in (6.4a).

We restrict our explanations to the two-dimensional case. The one-dimensional case is analogously treated. Let $\Omega : [0, L_x] \times [0, L_y] \subset \mathbb{R}^2$ be a rectangular domain discretized by an equidistant grid of squared grid size $\triangle x \times \triangle x$.

Finite volume scheme

Let us consider a single box of the grid centered at $(i\triangle x, j\triangle x)$ with index (i, j). We treat h and the discrete divergence $\nabla^h \cdot J$ as to be defined on the volume of the box, labeled by $h(i, j)$ and $(\nabla^h \cdot J)(i, j)$. In contrast, both the first and second component of the flux $J = (J_1, J_2)^T$ and the discrete gradient $\nabla^h h$ are considered to be defined on the corresponding edges of each box; they are labeled by $(i \pm \frac{1}{2}, j)$ and $(i, j \pm \frac{1}{2})$, respectively, see Figure 6.1. Now, the space-discretized version of Gauss' theorem restricted to the

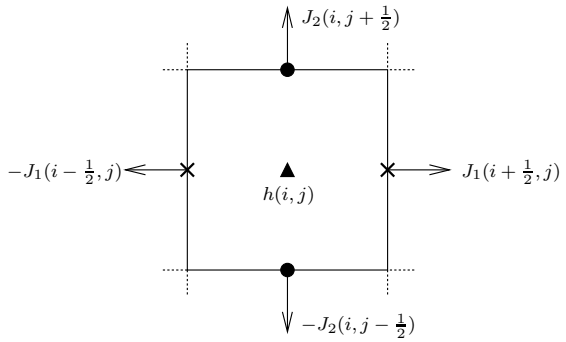

Figure 6.1: The discretized flux $J = (J_1, J_2)^T$ and film height h on a quadratic box of size $\triangle x \times \triangle x$. The function h lives on the volume, the components of J on the edges.

single box, i.e.

$$(\nabla^h \cdot J)(i, j)\triangle x^2 = (J_1(i + \tfrac{1}{2}, j) - J_1(i - \tfrac{1}{2}, j) + J_2(i, j + \tfrac{1}{2}) - J_2(i, j - \tfrac{1}{2}))\triangle x,$$

allows us to define the discrete divergence $\nabla^h \cdot$ in a consistent way:

$$(\nabla^h \cdot J)(i, j) := \left(\tfrac{1}{\triangle x}(J_1(i + \tfrac{1}{2}, j) - J_1(i - \tfrac{1}{2}, j)) + \tfrac{1}{\triangle x}(J_2(i, j + \tfrac{1}{2}) - J_2(i, j - \tfrac{1}{2}))\right).$$

The right hand side describes the total mass inflow per unit volume.

Now, it is easy to show that such a discretization of $\nabla^h \cdot$ guarantees mass conservation: Since the discretized flux J and the film height h are coupled through (6.4b), we have

$$\begin{aligned}
& \frac{1}{\tau}\left(\triangle x^2 \sum_{i,j} h^{k+1}(i,j) - \triangle x^2 \sum_{i,j} h^k(i,j)\right) \\
= \;& \triangle x^2 \sum_{i,j} \frac{1}{\tau}\Big(h^{k+1}(i,j) - h^k(i,j)\Big) \\
= \;& -\triangle x^2 \sum_{i,j} (\nabla^h \cdot J^{k+1})(i,j) \\
= \;& -\triangle x \sum_{i,j} \Big(J_1^{k+1}(i+\tfrac{1}{2},j) - J_1^{k+1}(i-\tfrac{1}{2},j) + J_2^{k+1}(i,j+\tfrac{1}{2}) - J_2^{k+1}(i,j-\tfrac{1}{2})\Big) \\
= \;& 0,
\end{aligned}$$

due to cancellation at the inner edges. The boundary edges either cancel for periodic boundary conditions or equal to zero for no-flux boundary conditions.

To keep the symmetry of the discretized operator in (6.4a), we have to define the discrete gradient ∇^h such that it is dual to the discrete divergence. In particular, it requires that ∇^h lives on the edges. Consequently, the dual operator is defined by

$$\begin{aligned}
(\nabla^h h)_1(i+\tfrac{1}{2},j) &= \tfrac{1}{\triangle x}(h(i+1,j) - h(i,j)), \\
(\nabla^h h)_2(i,j+\tfrac{1}{2}) &= \tfrac{1}{\triangle x}(h(i,j+1) - h(i,j)).
\end{aligned}$$

An easy calculation shows that these choices amount to a symmetric iteration matrix.

Treatment of the mobility

According to the definition of the flux J and the gradient, the discrete mobility function $m = m(h)$ should be defined on the edges of each box. As the discrete height h is in general discontinuous at the edges, we have to replace m by an averaged value, e.g. by

$$m(h)(i+\tfrac{1}{2},j) := f(m(h(i+1,j)), m(h(i,j))) \qquad \text{at edge } (i+\tfrac{1}{2},j),$$

where f is a suitable average function. It was shown in [18] for a finite element discretization that choosing f as the harmonic mean, i.e.

$$f(a,b) := \frac{1}{\frac{1}{2}(\frac{1}{a}+\frac{1}{b})},$$

yields a non-negativity preserving scheme. We follow that choice.

6.1.3 Linear solver

As we choose a symmetry-preserving spatial discretization of the operator, we can use the conjugate gradient method with preconditioning as an iterative solver for (6.4a).

Let us comment on why we expect the operator to be positive definite for a suitable time step τ: The weak formulation of the operator in (6.3) can be easily estimated by

$$\begin{aligned}
&\int \frac{1}{m(h^k)}|J|^2\,dx + \tau\left[\int |\nabla\nabla\cdot J|^2\,dx + \int \mathcal{U}''(h^k)(\nabla\cdot J)^2\,dx\right] \\
&\quad\geq\quad \frac{1}{M}\int |J|^2\,dx + \tau\left[\int |\nabla\nabla\cdot J|^2\,dx - C_0\int (\nabla\cdot J)^2\,dx\right] \\
&\quad\geq\quad 0, \qquad \text{provided} \quad \tau \leq \frac{4}{MC_0^2},
\end{aligned}$$

where we set $M := \max m(h^k)$ and $C_0 := -\min \mathcal{U}''(h^k) \approx 0.47$. The bound on τ strongly depends on the film height h^k. Nevertheless, we expect to use much larger time steps for our numerical tests: We are interested in the evolution of configurations consisting of equilibrium droplets. For a single equilibrium droplet, the Hessian of E, that is $-\Delta + \mathcal{U}''(h)$, is positive semi-definite, as the profile is a minimizer of the energy. Hence, we expect that the spectrum of the operator for an ensemble of near-equilibrium droplets is non-negative for fairly large time steps τ. Indeed, in numerical tests we gain the experience that choosing time steps (at least) of order 1 still leads to a positive definite iteration matrix.

FFT preconditioning

In the case of periodic boundary conditions, the Fast Fourier Transform (FFT) provides an easy but efficient method for preconditioning, see [27]. Let us briefly explain the main ideas.

We run numerical simulations to determine coarsening rates experimentally. For that purpose, a typical configuration is characterized by well-separated droplets connected by a precursor of constant height $h \approx 1$. Hence, the contribution of the mobility function to the flux concentrates on the sparse droplet matrix. By setting $m \equiv m(\text{precursor}) = 1$ and $\mathcal{U}'' \equiv \mathcal{U}''(\text{precursor}) = 6$, the operator in (6.4a) turns into a linear operator, which can be inverted by FFT in the case of periodic boundary conditions [34]. For instance in the one-dimensional case, the i-th Fourier multiplicator corresponding to (6.4a) is given by

$$1 + \tau\left(\frac{2}{\triangle x^4}\cos\left(\frac{4\pi i}{K}\right) - \left(\frac{8}{\triangle x^4} + \frac{2\mathcal{U}''(1)}{\triangle x^2}\right)\cos\left(\frac{2\pi i}{K}\right) + \frac{6}{\triangle x^4} + \frac{2\mathcal{U}''(1)}{\triangle x^2}\right),$$

where K is the total number of grid points. We apply the C subroutine library FFTW [13] to compute the discrete Fourier transform.

PETSc Toolkit

To solve (6.4a), we use the **P**ortable, **E**xtensible **T**oolkit for **Sc**ientific Computation (PETSc) [3], which provides data structures and large classes of efficient (non-)linear solvers for the implementation of high-dimensional problems. Especially, a broad class

of Krylov subspace iterative methods such as the conjugate gradient method and preconditioners are available.

The toolkit allows us to test a broad selection of preconditioners, particularly in the case of no-flux boundary conditions, where the "cheap" but efficient preconditioning described in the previous section does not apply.

6.1.4 Finite element implementation

An adaptive finite element formulation for Cahn–Hilliard-type equations is proposed in [32]. It relies on a weak formulation for the flux J derived from (6.3), which only requires $H(\nabla\cdot,\Omega)$-vector fields, where

$$H(\nabla\cdot,\Omega) := \left\{ J \in (L^2(\Omega))^2 \;\middle|\; \nabla\cdot J \in L^2(\Omega) \right\}.$$

Suitable $H(\nabla\cdot,\Omega)$-conforming elements are the Raviart–Thomas elements, whose normal component across edges is continuous, which provides the conformity.

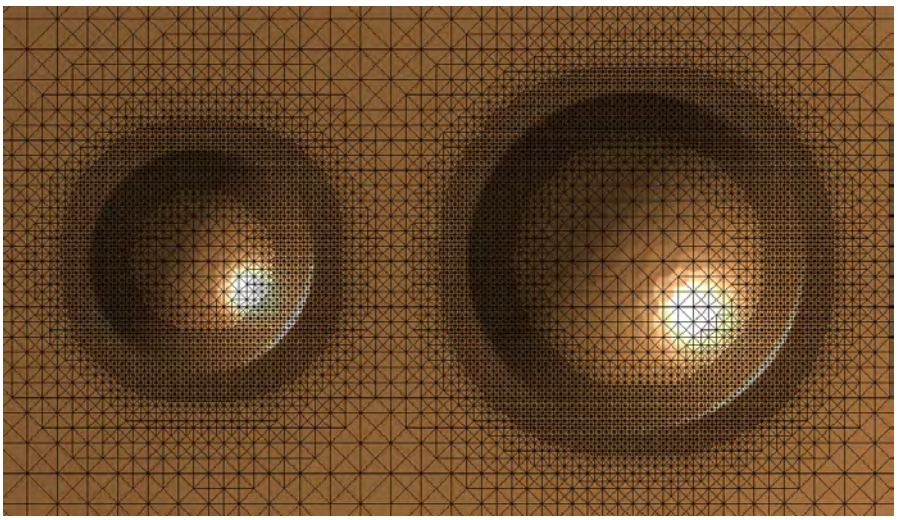

Figure 6.2: A geometrically refined mesh for the finite element implementation [32] of the thin-film equation for a two-droplet configuration.

Transition layers of small width are characteristic of Cahn–Hilliard-type equations. Therefore, the mesh refinement is a function of the distance to the transition layer. For the thin-film equation, the transition region is located in the droplet foot, see Section 2.1. In this region, the potential $\mathcal{U}$ has maximal slope, which is balanced by relatively large curvature of the profile. The local refinement of the grid allows us to reduce the number of unknowns of the discretized problem significantly, see Figure 6.2.

For the time discretization, both first- and second-order time schemes have been implemented.

6.2 Discretization of the reduced Rayleigh dynamics in two dimensions

We consider an N-droplet configuration in two dimensions, which is given by $\Theta := (V_1, \dots, V_N, X_1^T, \dots, X_N^T)^T \in \mathbb{R}^{3N}$. Then the reduced Rayleigh dynamics of this configuration is determined by the system of ODEs (5.10), that is

$$\begin{aligned} \Pi(G\dot{\Theta} + \nabla E) &= 0, \\ \dot{\Theta} \cdot p &= 0, \end{aligned}$$

where the projection Π to the mass-conserving subspace is defined by $\Pi = (\mathbb{I}\mathrm{d} - pp^T)$, and $p = \frac{1}{\sqrt{N}}(1_N, 0_{2N})^T \in \mathbb{R}^{3N}$ is the normal of the subspace.

The entries of the matrix $G = G(\Theta)$ are given to leading order by the approximate expressions in Section 5.3.2. However, most of the leading order expressions of the migration factor were identified only in terms of scaling. In particular, for $q > 2$ the coefficient c_{ij}, and for $q > 3$ the coefficient g_i depend to leading order on the detail of the potential $\mathcal{U}$ as we pointed out in Section 4.2. Hence in this cases, our asymptotic results differ from the actual limiting dynamics by a factor of order 1. Therefore, we focus on the (also physically relevant) case $q = 2$, for which the leading order coefficients rely on the mesoscopic droplet profile. For convenience, let us summarize the known approximate coefficients in the case $q = 2$:

$$G_{ij}^v = -\tfrac{1}{4\pi}\left(\log(L_{ij}/V_i^{\frac{1}{3}}) + \log(L_{ij}/V_j^{\frac{1}{3}})\right), \tag{6.5a}$$

$$g_i = \tfrac{2}{\pi^{\frac{2}{3}}}\, C_{\mathrm{num}}\, V_i^{\frac{2}{3}}, \tag{6.5b}$$

$$c_{ij} = -\tfrac{1}{3\pi^{\frac{1}{3}}}\, L_{ij}^{-1}\, V_i^{\frac{1}{3}} \log V_i, \tag{6.5c}$$

where we numerically derived the constant $C_{\mathrm{num}} \approx 2.8026$ by solving a variational problem, see (4.60).

We will comment on possible extensions to the case $q = 3$ in Section 6.3.2.

6.2.1 Time discretization

Let $\{t_k\}_{k=0}^K$ be a (not necessarily equidistant) finite partition of the time interval $[0, T]$ of step size $\tau_k := t_{k+1} - t_k$. Furthermore, we set $V_i^k := V_i(t_k)$, $X_i^k := X_i(t_k)$ and $\Theta^k := \Theta(t_k)$.

Explicit Euler scheme

As the simplest time discretization, we apply the explicit Euler scheme:

$$\Pi G(\Theta^k)\Theta^{k+1} = \Pi G(\Theta^k)\Theta^k - \tau_k\, \Pi \nabla E(\Theta^k), \tag{6.6a}$$

$$\Theta^{k+1} \cdot p = \Theta^k \cdot p. \tag{6.6b}$$

One can easily see that the first N rows of the $(3N \times 3N)$-system of equations (6.6a) are linearly dependent due to the projection Π. Consequently, we replace one of this rows by the second equation (6.6b), which finally defines a linear system of equations $A(\Theta^k)\Theta^{k+1} = b(\Theta^k)$. This system has a unique solution Θ^{k+1}, provided the droplet configuration is regular, which means that all volumes and distances defined by Θ are non-zero, see Section 6.2.3.

Let us now argue why the proposed explicit first-order scheme provides an accurate discretization for our purposes – even for fairly large time steps. We conduct a convergence test for a typical two-droplet configuration in the regime (5.1), which will be used in Section 6.3.2. As reference values we take the volumes and centers at time $T = 10^3$ derived numerically according to (6.6) with uniform time steps $\tau_k \equiv 10^{-3}$. Then we compare the results with the values derived with coarsened time steps $\tau_k \equiv 10^{m-3}$, $m = 1, \dots, 6$, in terms of the relative deviation, e.g. given by $\left(V_1^{\tau=10^{m-3}}/V_1^{\tau=10^{-3}} - 1\right)$. Figure 6.3 shows the relative deviation of the volumes and centers for all different time steps. (Of course, the linear shape to the right has been expected for a first-order discretization.) For instance at $\tau = 10$, the deviation is at most of order $\mathcal{O}(10^{-8})$, or extrapolated on

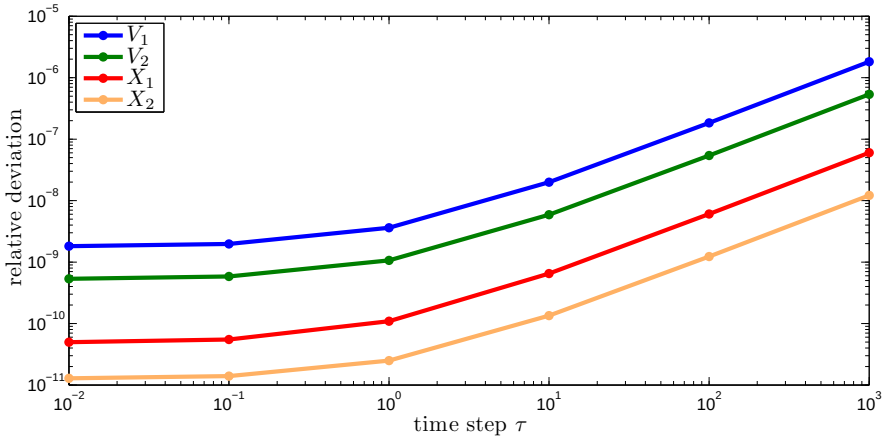

Figure 6.3: Convergence test for a typical configuration of two droplets at final time $T = 10^3$: Relative deviation for the reference time stepping $\tau = 10^{-3}$ in logarithmic plot.

$T = 10^5$ (typical for our numerical tests), of order $\mathcal{O}(10^{-6})$. Therefore, the uniform time step $\tau = 10$ gives results with sufficient accuracy for our purposes.

6.2.2 Linear solver

The matrix $A(\Theta^k)$ is non-symmetric, so that a direct application of the conjugate gradient method is not possible. For large systems, a direct method such as LU decomposition seems to be the most efficient method compared to iterative solvers. As before, we apply the PETSc Toolkit for the implementation.

However, the question of a suitable linear solver is only of minor importance, since we mainly focus on numerical tests for a configuration of only two droplets defined by $\Theta = (V_1, V_2, X_1^T, X_2^T)^T$, see 6.3.2. The time-discrete version of the system of ODEs for two-droplet configurations can be explicitly solved according to (5.35) and (5.36):

Volume update:

$$V_1^{k+1} = V_1^k - \tau_k \frac{4\pi^{\frac{4}{3}}}{\log(L^k/(V_1^k)^{\frac{1}{3}}) + \log(L^k/(V_2^k)^{\frac{1}{3}})} ((V_1^k)^{-\frac{1}{3}} - (V_2^k)^{-\frac{1}{3}}), \quad (6.7a)$$

$$V_2^{k+1} = V_2^k - (V_1^{k+1} - V_1^k), \quad (6.7b)$$

where $L^k = |X_1^k - X_2^k|$.

Center update:

$$X_1^{k+1} = X_1^k - \frac{c_{12}}{g_1}(V_1^{k+1} - V_1^k), \quad (6.7c)$$

$$X_2^{k+1} = X_2^k - \frac{c_{21}}{g_2}(V_1^{k+1} - V_1^k). \quad (6.7d)$$

The coefficients c_{ij} and g_i are defined in (6.5).

6.2.3 Coarsening rules

The validity of the reduced system of ODEs (5.10) breaks down when it leaves its asymptotic regime (5.1), namely when either one of the droplet volumes V or the distances L tend to zero (collapse or collision). When such events occur, the system needs to be updated to a system of ODEs with reduced dimension. In the following, we will give the two update criteria, which are similar to the ones given in [16].

Collapse rule. As it was argued in Section 2.1, a droplet of decreasing volume has increasing pressure $P \to P_{\max} = \max_{h>0} \mathcal{U}'(h)$. Hence, we detect a droplet collapse if the droplet volume satisfies

$$V \leq (1-\varepsilon)V_{\min} \overset{(2.34)}{=} (1-\varepsilon)8\pi\ P_{\max}^{-3},$$

where ε is small. In particular, the rule depends on details of the potential $\mathcal{U}$. The vanished droplet is eventually erased from the configuration vector.

Collision rule. We identify a droplet collision between two droplets when their contact lines meet:

$$|X_1 - X_2| - (R_1 + R_2) \leq \delta,$$

where δ is small. The size of the configuration vector, and therefore of the system of ODEs, has to be reduced by merging the droplets into a new one. In the one-dimensional

case, a "merging rule" for two droplets is proposed in [16]. We analogously adapt it for the two-dimensional case. Due to mass conservation, the volume of the merged droplet is the sum of the volumes of the collided droplets: $V^{\text{merge}} := V_1 + V_2$. Its center is symmetric with respect to the outer contact lines of the two droplets along the difference vector $X_2 - X_1$, that is

$$X^{\text{merge}} = \tfrac{1}{2}(X_1 + X_2) + \tfrac{1}{2}(R_2 - R_1)\frac{(X_2 - X_1)}{|X_2 - X_1|}. \tag{6.8}$$

As opposed to the one-dimensional case [14], no analysis is done in the two-dimensional case for a further justification of this rule.

Time adaptivity

Let us conclude this section by some comments on time adaptivity. The smaller the volume of the droplet the more rapid the change of its volume is, since the volume change scales as $\dot{V} \sim (\log V)^{-1} V^{-1/3}$ according to (5.35). Hence, a careful time stepping is needed when the system reaches a critical collapse event. The time step τ_k between V^k and V^{k+1} has to be chosen such that V^{k+1} stays positive until it satisfies the collapse rule. Figure 6.4 shows a typical adaptive time stepping while a droplet collapses. Here,

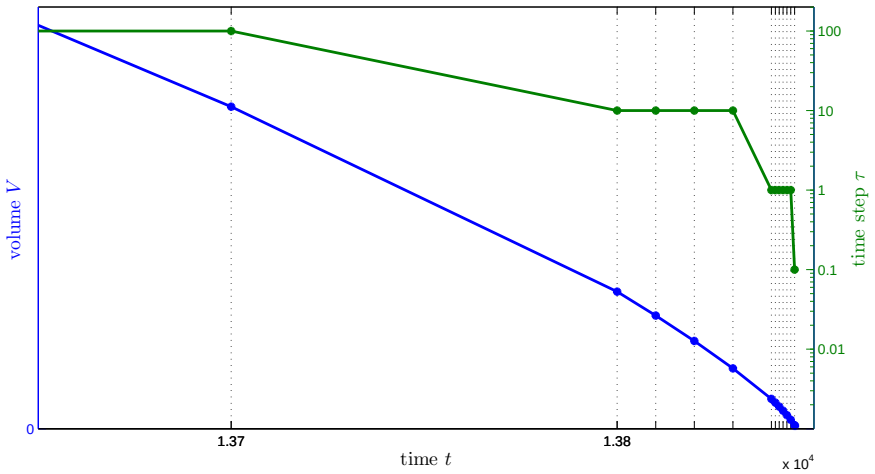

Figure 6.4: Adaptive time stepping at a collapse event.

one refinement step is given by the factor 0.1.

6.3 Numerical experiments

At first, we will present results of large-scale coarsening simulations of the thin-film equation in both one and two dimensions. They confirm the rigorous results on the coarsening rates in Chapter 3. Furthermore, we compare the reduced Rayleigh dynamics

(and further refinements of this approximation) with results obtained from the thin-film equation and enlighten the competition between collision and collapse of droplets in two dimensions.

6.3.1 Coarsening rates

In Chapter 3, we rigorously derive lower bounds on the energy decay in a time-averaged sense, from which we heuristically deduce upper bounds on the coarsening rate (3.59):

$$N(t) \gtrsim t^{-\frac{d(d+1)}{3d+2}}.$$

Numerical tests support these rigorous result as we will present in the following.

We conduct numerical simulations for mobility exponent $q = 1$ in both one and two dimensions based on the scheme (6.4) with periodic boundary conditions. The domain is given by a square $[0, \Lambda]^d$, where $\Lambda = 10000$ for $d = 1$ and $\Lambda = 1000$ for $d = 2$, with spatial resolution $\triangle x \approx 1$. As initial data, we take

$$h_0 = h^* + \text{small perturbation},$$

where we choose $h^* = 2$ within the unstable range, i.e. the concave part of the potential $\mathcal{U}$.

After an initial stage, a configuration of well-defined droplets connected by a precursor layer of height $h \approx 1 = \operatorname{argmin} \mathcal{U}$ emerges. For $d = 1$, this configuration consists of several hundred droplets, for $d = 2$ of several thousands. From then onwards, the configuration coarsens as already described. Figure 6.5 shows a logarithmic plot of the number of droplets and the energy densities vs. time both in one and two dimensions. Note that the data is averaged over ten runs.

In one dimension, our numerical experiments reveal the theoretical scaling exponent $-\frac{2}{5}$ for $d = 1$ (see Figure 6.5 left). This exponent is equal to the upper bound we obtained in (3.59). Experiments for $d = 2$ (see Figure 6.5 right) suggest a faster decrease of the number density than for $d = 1$, as theoretically predicted. The coarsening exponent is in agreement with the bound (3.56), but appears to be slightly different than the bound itself. Let us comment on this apparent discrepancy: The heuristics in Section 3.6 are based on the assumption that

$$\Lambda^{-d} E \overset{(3.54)}{\sim} L^{-\frac{d}{d+1}} \sim \left(\Lambda^{-d} N\right)^{\frac{1}{d+1}}.$$

We therefore monitor the system averaged quantity $\Lambda^{-d} E \left(\Lambda^{-d} N\right)^{-\frac{1}{d+1}}$ over time. For an infinite system this number should reach an asymptotic value if coarsening is statistically self-similar. Figure 6.6 shows this quantity vs. time and reveals that for $d = 2$ the numerical simulations have barely reached an asymptotic state. Hence in this case, a numerical confirmation of the optimality of our result would require much larger time horizons and thus much larger system sizes.

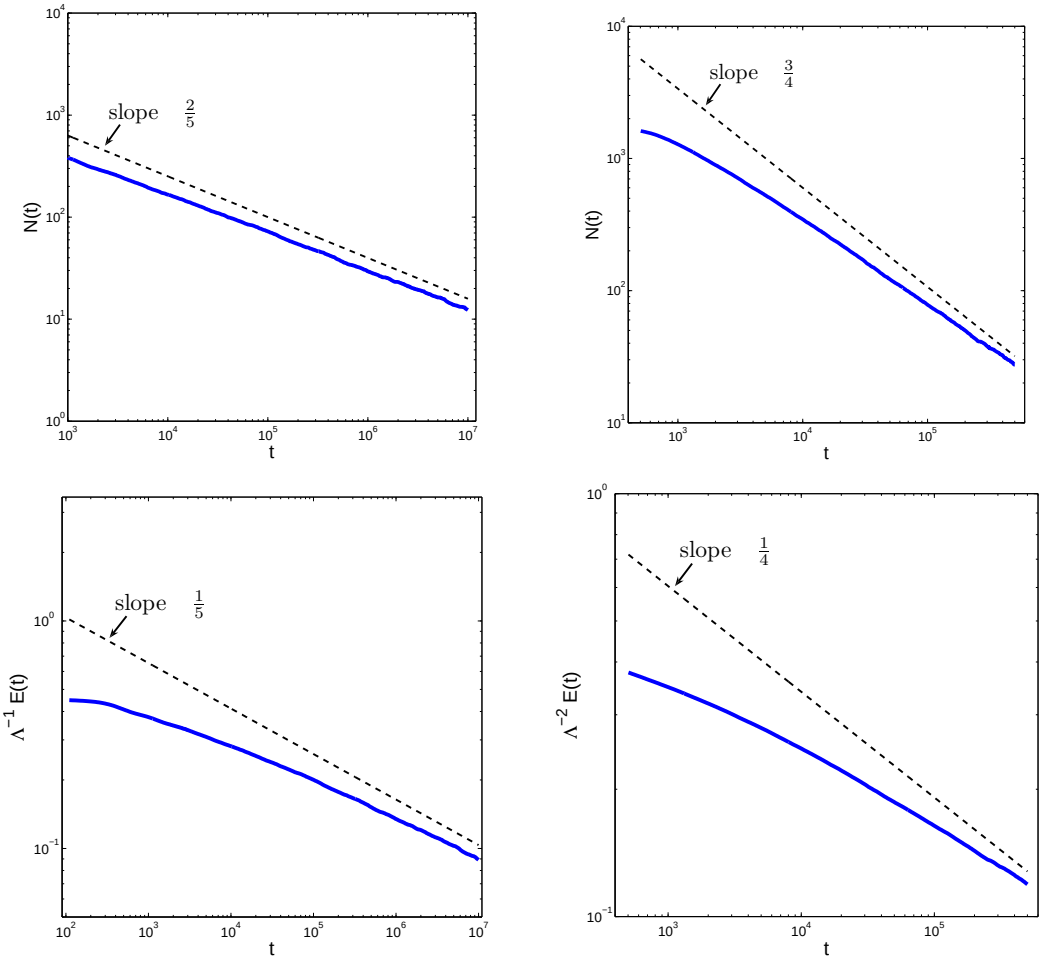

Figure 6.5: Number of droplets (top) and energy density of the droplet configuration (bottom) in dimension $d = 1$ (left) and for $d = 2$ (right) vs. time in logarithmic scale.

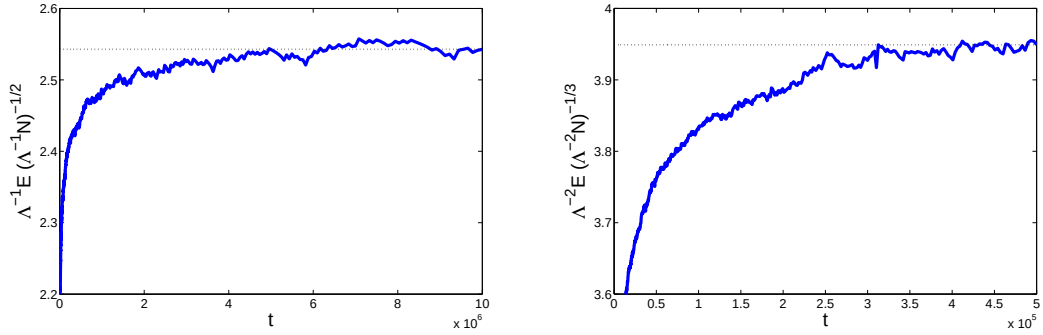

Figure 6.6: The system averaged quantity $\Lambda^{-d} E \left(\Lambda^{-d} N\right)^{-\frac{1}{d+1}}$ for $d = 1$ (left) and for $d = 2$ (right) vs. time.

6.3.2 Reduced Rayleigh dynamics: Comparison with the thin-film equation

In this section, we consider a two-droplet configuration $\Theta = (V_1, V_2, X_1^T, X_2^T)^T$ in two dimensions, see Figure 6.7. We will compare the evolution of this configuration given by the thin-film equation with the evolution given by the reduced Rayleigh dynamics. In particular, we will address the question how close to the thin-film equation we can get with the reduced model in order to convince ourselves of the validity of the approximations.

Set-up for numerical tests for the thin-film equation. Let us first introduce the set-up for the numerical tests conducted for the thin-film equation: We consider a rectangular domain $\Omega := [0, L_x] \times [0, L_y]$ with lengths $L_x = 500$ and $L_y = 300$. A suitable spatial resolution is defined by 800×480 grid points. We solve the thin-film equation numerically according to (6.4) and assume no-flux boundary conditions. As initial condition, we always take the profile representing the union of two mesoscopic droplets on a uniform precursor layer of height 1.

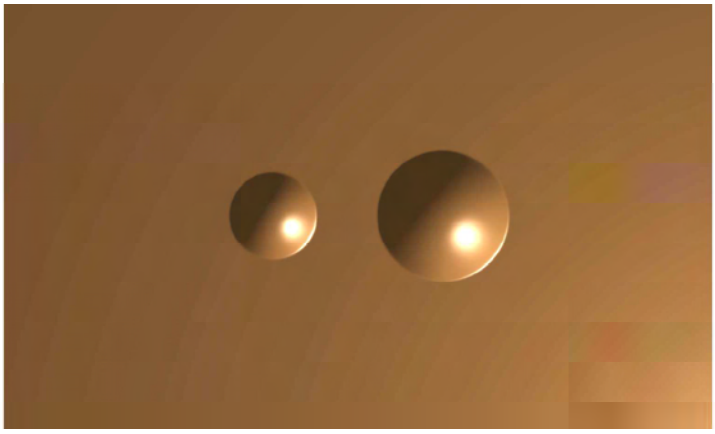

Figure 6.7: A typical initial two-droplet configuration.

To familiarize ourselves with the dynamics of this configuration according to the thin-film equation, consider the droplet evolution presented in Figure 6.8, which compares the different mobility exponents $q = 2$ and $q = 3$. Initial conditions are $R_1(0) = 30$, $R_2(0) = 45$, $X_1(0) = (190, 150)^T$ and $X_2(0) = (310, 150)^T$. Both droplets move westwards as we motivate in the introduction of the thesis. The migration speed strongly increases with q. Note that we only display the first coordinates of X_1 and X_2, because the second coordinates do not change in our symmetric set-up. Independent of q, the larger droplet (with volume V_2 and center X_2) migrates slower than the smaller droplet in accordance with the scaling of the migration factor. At the same time, the larger droplet grows at the expense of the smaller one. Furthermore, the volume evolution of both droplets varies only slightly for different q, more precisely, the higher mobility $q = 3$ leads to a somewhat faster mass transfer.

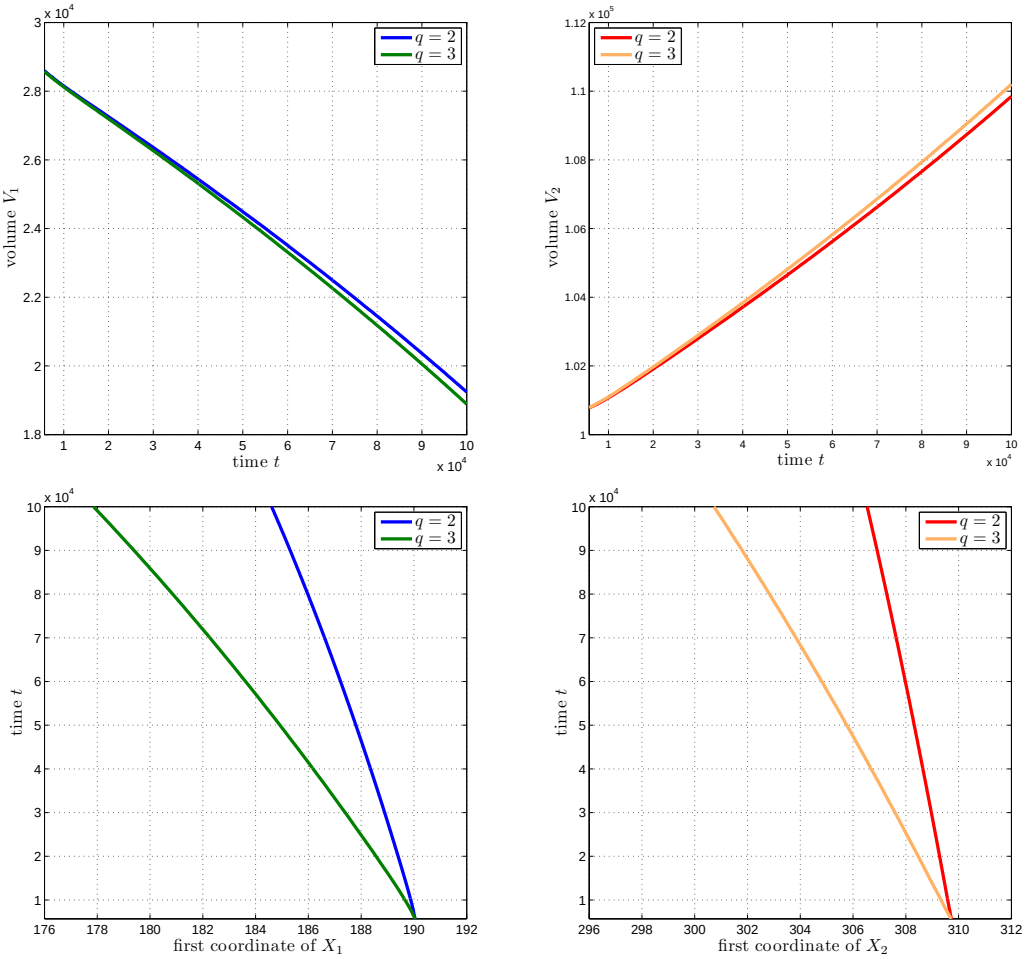

Figure 6.8: Evolution of the droplet volumes (top) and centers (bottom) for a two-droplet configuration according to the thin-film equation with different mobility exponents.

Initial relaxation layer. At the beginning, the sharp initial profile relaxes according to the thin-film equation to a near-equilibrium state. In detail, the droplets take their near-equilibrium shape, and the foot region smoothly connects to the precursor layer, whose height is slightly adjusted. Here, the relaxation of the profile happens much faster in the droplets of height $h \sim R$ than in the precursor $h \approx 1$, since the mobility h^q is much larger in this region. Hence, we expect that the total energy, whose leading order contribution comes from the droplets, relaxes on a faster time scale than the dissipation, whose leading order contribution stems from the precursor, see Section 4.1. Figure 6.9 compares the dissipation $D(u)$ in the precursor derived from the thin-film equation, see (1.25), with the dissipation $D(\dot{\Theta})$ based on the centers and radii of the two-droplet configuration. It reveals an initial relaxation layer for $D(u)$ of large size $[0, 10^4]$. Therefore, we start

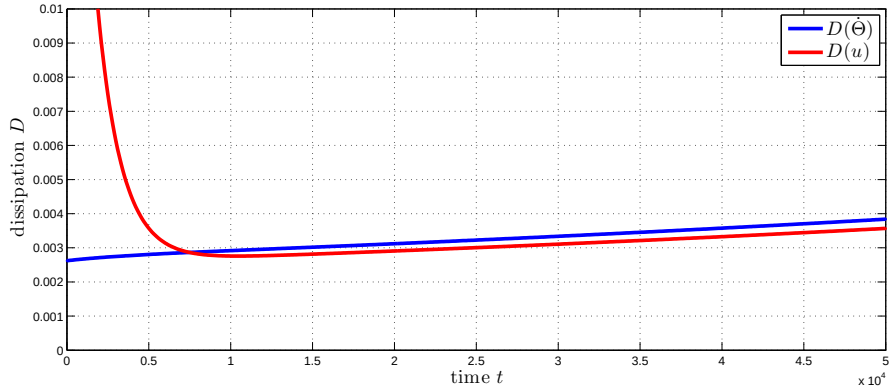

Figure 6.9: Comparison of $D(u)$ and $D(\dot{\Theta})$ evaluated outside the mesoscopic droplets. The large initial layer occurs according to the relatively small mobility in the precursor region.

comparing both models after this initial layer, more precisely at time $T = 20000$.

Comparison. Now let us have a first glance on the comparison of the reduced Rayleigh dynamics with the evolution obtained from the thin-film equation. As initial conditions, we take

$$\begin{aligned} R_1(0) &= 30, & R_2(0) &= 45, \\ X_1(0) &= (190, 150)^T, & X_2(0) &= (310, 150)^T, \end{aligned} \tag{6.9}$$

in the rectangular domain Ω. The size of the droplets (in terms of their radii) is chosen sufficiently large such that the droplet profiles are near the leading-order mesoscopic profiles. Here and in the following, we focus on the mobility exponent $q = 2$ as explained in the introduction of Section 6.2.

As Figure 6.10 reveals, the comparison results are unsatisfactory. However, the large deviations of the reduced dynamics from the results of the thin-film equation are not unexpected, since the reduced dynamics as stated in (5.35) and (5.36) were derived in the asymptotic regime $1 \ll R \ll L$ of well-separated, large droplets on an infinite domain, see Chapter 5. Obviously, the typical droplet size R and the ratio L/R are too small to obtain convincing results.

Furthermore, we should keep in mind that the numerical tests for the thin-film equation are conducted on a finite domain with no-flux boundary conditions. In contrast, for the reduced Rayleigh dynamics both equations for the volume changes (5.35) and migration (5.36) rely on the fundamental solution of the whole space. Therefore, we finally require the length scale separation

$$1 \ll R \ll L \ll \Lambda,$$

where Λ denotes the typical system size, to obtain a good agreement. The results presented in Figure 6.10 display the overall impact of the relative size of these length scales on the accuracy of the approximation.

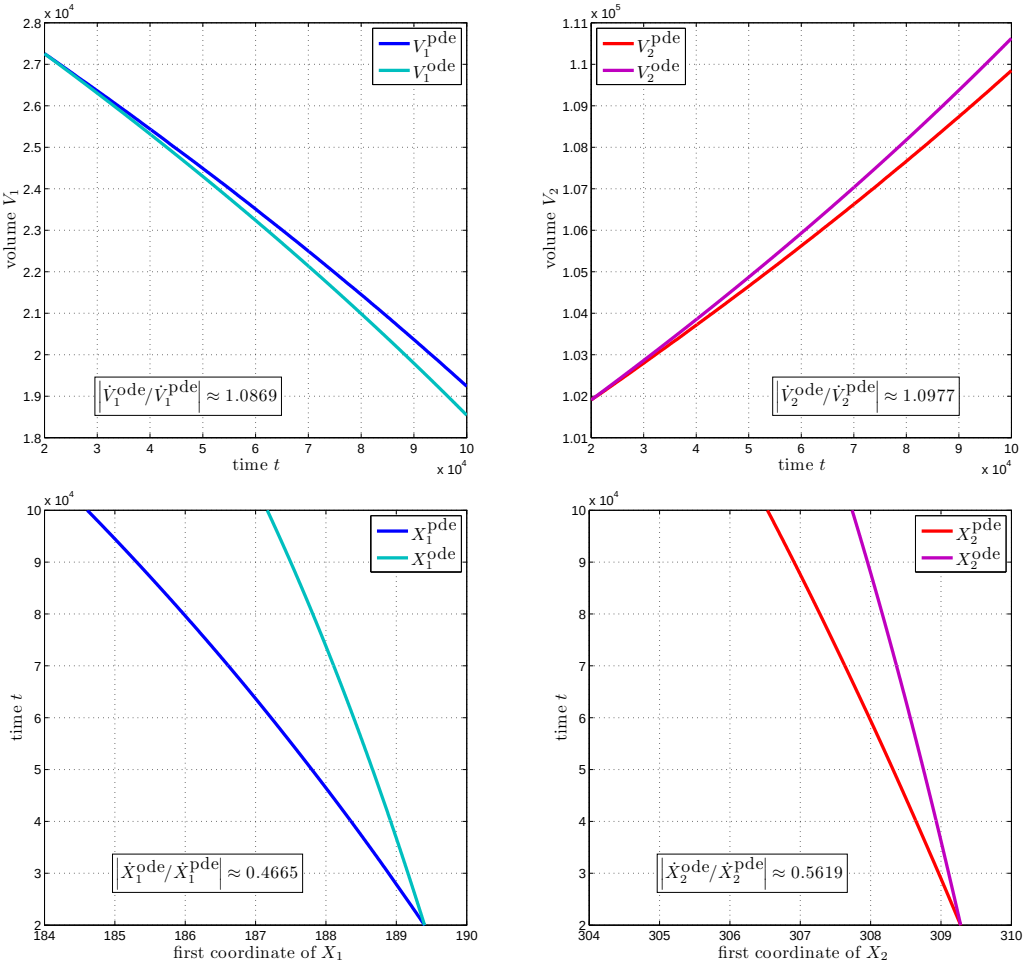

Figure 6.10: Comparison of the reduced Rayleigh dynamics with results from the thin-film equation for mobility exponent $q = 2$: the evolution of the volumes (top) and the centers (bottom).

In the remainder of this section, we will present auxiliary problems, which serve to improve the Rayleigh dynamics in the following way:

- We will introduce an auxiliary problem, by which the volume change of droplets is well-approximated in the regime $R \gg 1$. Therefore, the accuracy does no longer depend on the relative size of L and Λ.
- The approximation of the droplet velocity is more elaborate. First of all, we will derive the migration factor $\mathtt{mig}$ by solving the problems for ψ_0 and ψ_1 numerically based on the mesoscopic droplet profile, which certainly is the most apparent improvement for migration. Furthermore, we will adjust the ambient flux field,

which generates migration, as we will account for the effect from the boundary in particular.

Let us clearly state that we do not address the question how to overcome the requirements on the length scales made in the derivation of the droplet interaction , i.e. the "decoupling regime" (see e.g. equation (5.27) in Section 5.3.1), which is based on the assumption $L \gg R$. However, we will carry out numerical tests for increasing L but fixed R to clarify the impact of this regime.

Finally, let us mention that we include each additional improvement after its introduction for subsequent simulations (as not otherwise stated).

Approximation of the volume change in the regime $R \gg 1$

We present an auxiliary problem, which approximates the volume changes to leading order in the regime of large droplets, i.e. $R \gg 1$. The accuracy of the approximation is independent of the scale separation $R \ll L \ll \Lambda$, and therefore improves the asymptotics of Section 4.1 by numerics. However, it still relies on the asymptotic shape of equilibrium droplets presented in Section 2.1, in particular on the following:

- The precursor has constant height 1 to leading order, which in particular implies $m \equiv 1$ outside the droplets, see (2.24a).
- The pressure has constant boundary values $\frac{2\sqrt{2}}{R_i}$ on ∂B_i, see (2.24b).
- The support of the i-th droplet is the ball B_i with radius R_i centered at X_i, see (2.24c).

Here, we denote $B_i := B_{R_i}(X_i)$. We consider the auxiliary pressure Ψ_0, which solves the problem

$$-\Delta\Psi_0 = 0 \qquad \text{in } \Omega\backslash(B_1 \cup B_2), \tag{6.10a}$$

$$\Psi_0 \equiv \tfrac{2\sqrt{2}}{R_i} \quad \text{on } \partial B_i,\ i = 1,2, \qquad \nabla\Psi_0 \cdot \nu = 0 \quad \text{on } \partial\Omega, \tag{6.10b}$$

It can be understood as the limit problem for the pressure $\frac{\delta E}{\delta h}(h)$ outside large droplets in the case $q = \infty$.

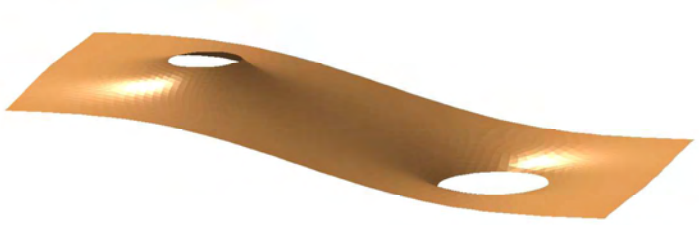

Figure 6.11: Height profile of the auxiliary pressure Ψ_0, a solution of (6.10).

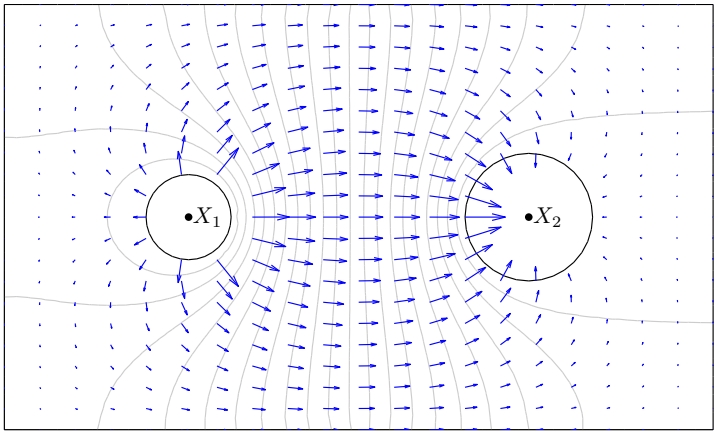

Figure 6.12: The pressure Ψ_0 (grey contour lines) generates the mass transfer flux $J = -\nabla\Psi_0$ (blue arrows) from the smaller droplet at X_1 to the larger one at X_2.

Figure 6.11 shows a solution of (6.10) for a typical two-droplet configuration, which is numerically derived by a finite element method implemented in the PDE toolbox of MATLAB. Then the flux $-\nabla\mu$ (see Figure 6.12) determines the volume change $\dot{V}_i$ of each droplet by

$$\dot{V}_i = \int_{\partial B_i} -\nabla\Psi_0 \cdot \nu \, dx.$$

Now we will demonstrate the increase of accuracy, if we apply this improved approximation. For this purpose, we consider the evolution of the two-droplet configuration with initial data (6.9). Figure 6.13 reveals the absolute improvement.

Furthermore, we study the influence of a varying distance L. A quantitative comparison of the numerical results by means of the relative accuracy $\left|\dot{V}_1^{\text{corr}}/\dot{V}_1^{\text{pde}}\right|$ and $\left|\dot{V}_1^{\text{ode}}/\dot{V}_1^{\text{pde}}\right|$ is given in Table 6.1.

	$L = 120$	$L = 150$	$L = 180$	$L = 210$	$L = 240$
$\left\|\dot{V}_1^{\text{corr}}/\dot{V}_1^{\text{pde}}\right\|$	1.0233	1.0246	1.0246	1.0261	1.0238
$\left\|\dot{V}_1^{\text{ode}}/\dot{V}_1^{\text{pde}}\right\|$	1.0869	1.2179	1.3173	1.4090	1.4937

Table 6.1: Quantitative comparison of the volume changes $\dot{V}_1^{\text{pde}}$, $\dot{V}_1^{\text{corr}}$ and $\dot{V}_1^{\text{ode}}$ for increasing L, but fixed radii and system size.

The comparison reveals the following:

- For the improved approximation ($\dot{V}_1^{\text{corr}}$) the accuracy of the approximation is independent of the distance L. The results deviate from the full PDE dynamics only by $\approx 2.5\%$.

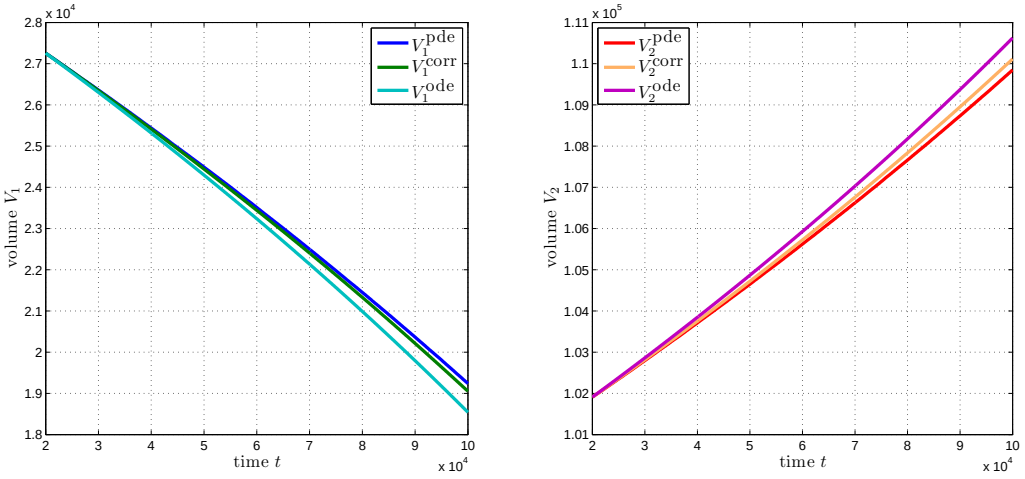

Figure 6.13: Comparison of the volume evolution derived from the full thin-film equation (V_i^{pde}), the intermediate approximation (V_i^{corr}) based on (6.10), and the reduced Rayleigh dynamics (V_i^{ode}).

- The accuracy of the reduced system of ODEs is expected to improve for increasing L. However, for increased distance the droplets approach the boundary of the domain, so that the boundary effect becomes more important. A glance at the relative accuracy reveals that the boundary has the dominant impact, since the accuracy gets even worse as the distance grows.

We expect that the order of accuracy grows for increased droplet sizes. Indeed, if we take as initial droplet sizes $R_1(0) = 45$ and $R_2(0) = 67.5$ with $L(0) = 240$ on the same domain, we obtain the relative accuracy $\left|\dot{V}_1^{\mathrm{corr}}/\dot{V}_1^{\mathrm{pde}}\right| \approx 1.014$.

Numerical evaluation of the migration factor $\mathtt{mig}(R)$

Figures 4.7 and 4.8 reveal the slow convergence of the integrals $\mathcal{I}_{\psi_0}$ and $\mathcal{I}_{\psi_1}$ to the leading order scaling given in (4.40) and (4.41). Therefore, an apparent further way of improving the reduced dynamics ODE is to derive the migration factor

$$\mathtt{mig}(R) \;=\; -\frac{\int \partial_1 h_i\, \psi_0 \, dx}{\int m_i |\nabla \psi_1|^2 \, dx}$$

directly with the help of the auxiliary pressures ψ_0 and ψ_1 instead of appealing to the scaling relations (6.5). We have already solved the problems for the auxiliary pressures in Chapter 4 numerically based on the mesoscopic droplet profile. Thus, we expect a significant impact on the accuracy of the approximations, as we conduct simulations with relatively small droplet radii. Figure 6.14 shows the interpolated values of $\mathtt{mig}(R)$ for $q = 2$ in the parameter regime of interest. So finally, we expect that the accuracy of the migration factor does no longer depend on the regime $R \gg 1$.

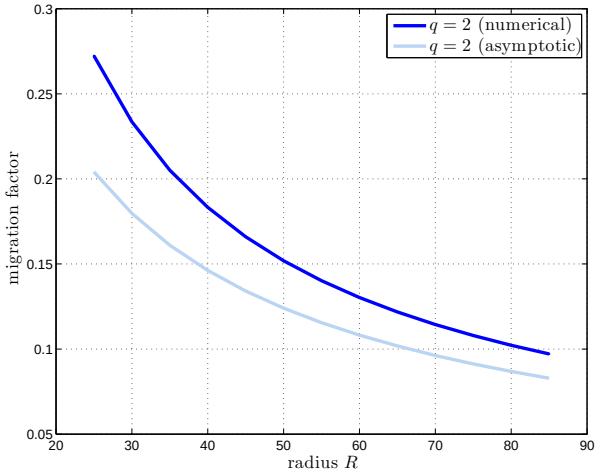

Figure 6.14: The migration factor $\mathfrak{mig}(R)$ numerically derived for the mobility exponent $q = 2$ in comparison with the asymptotic values.

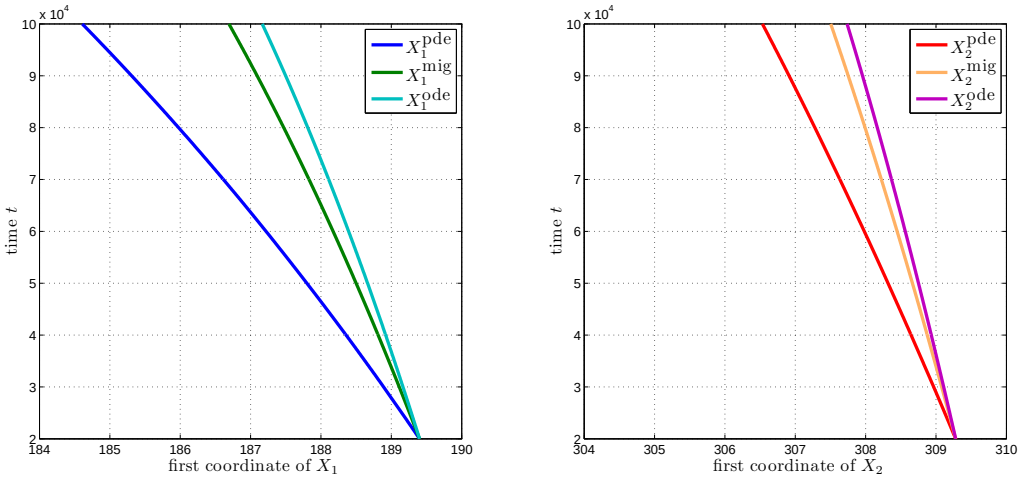

Figure 6.15: Comparison of the center evolution derived from the full thin-film equation (X_i^{pde}), the improved approximation (X_i^{mig}) based on the numerically derived migration factor, and the reduced Rayleigh dynamics (X_i^{ode}).

Figure 6.15 shows the improved dynamics based on the numerical values for $\mathfrak{mig}(R)$. It reveals a speed-up of the droplets of approximately 15–20%, where the improvement for the smaller droplet (left) is more significant than for the larger one (right) as expected.

Let us mention that numerical solutions ψ_0 and ψ_1 based on the equilibrium (instead of the mesoscopic) droplet profile could be used to treat the case $q = 3$ accurately, since they account for the details of the potential $\mathcal{U}$, and therefore yield the right migration

factor. However, in this thesis we do not pursue this idea any further.

Correction of the ambient flux field (Part I: Point sources in a bounded domain)

In the reduced dynamics of a two-droplet configuration, the ambient flux J_1, which generates the migration $\dot{X}_1$ of the first droplet, is identified as the gradient of the mass transfer potential $\dot{V}_2\,\psi_{V_2}$ evaluated at the droplet center X_1 (and J_2 analogously):

$$\begin{aligned} J_1 &:= -\nabla\left(\frac{\dot{V}_2}{2\pi}\log|x-X_2|\right)\Big|_{x=X_1} = \dot{V}_2\nabla\psi_{V_2}(X_1), \\ J_2 &:= -\nabla\left(\frac{\dot{V}_1}{2\pi}\log|x-X_1|\right)\Big|_{x=X_2} = \dot{V}_1\nabla\psi_{V_1}(X_2), \end{aligned}$$

see (5.37), so that the migration of the droplets is given by

$$\dot{X}_i = -\mathfrak{mig}(R)\,J_i \qquad \text{for } i=1,2$$

according to (4.30). However, we expect a correction in a finite domain due to the deviation of $\nabla\psi_{V_i}\cdot\nu$ at the boundary from zero. The flux is "channeled" by the no-flux conditions at the boundary, so that the reduced dynamics presumably underrate the driving ambient flux.

Let us introduce an auxiliary problem, which serves to correct the ambient fluxes J_1 and J_2 by adjusting the boundary conditions. We utilize the solution of

$$-\Delta\Psi_1 = 0 \quad \text{in } \Omega, \tag{6.11a}$$

$$\nabla\Psi_1\cdot\nu = \tfrac{\dot{V}_1}{2\pi}\left(\tfrac{x-X_1}{|x-X_1|^2}-\tfrac{x-X_2}{|x-X_2|^2}\right)\cdot\nu \quad \text{on } \partial\Omega, \tag{6.11b}$$

to refit J_1 and J_2:

$$J_1^{\mathrm{corr}} := J_1 + \nabla\Psi_1(X_1) \quad \text{and} \quad J_2^{\mathrm{corr}} := J_2 + \nabla\Psi_1(X_2).$$

Note that the solution Ψ_1 is constructed such that

$$\Psi_1^{\mathrm{corr}} := \frac{\dot{V}_1}{2\pi}\left(\log|x-X_1| - \log|x-X_2|\right) - \Psi_1$$

solves $-\Delta\Psi_1^{\mathrm{corr}} = \dot{V}_1(-\delta_{X_1}+\delta_{X_2})$ in Ω and $\nabla\Psi_1^{\mathrm{corr}}\cdot\nu = 0$ on $\partial\Omega$. Therefore, Ψ_1 represents the mass transfer potential with no-flux boundary conditions for droplets considered as point sources with mass $\pm\dot{V}_1$. Hence, the modified fluxes J_i^{corr} can be understood as the (in X_i) regularized gradients of Ψ_1^{corr}.

Let us present the impact of the flux correction for our introductory two-droplet configuration with initial conditions (6.9). Figure 6.16 shows the numerical results. Here, the relative improvement $|J_i^{\mathrm{corr}}/J_i|$ varies approximately between 1.473 and 1.482, that is a speed-up of the droplets of nearly 50%. Table 6.2 shows the improvement for different

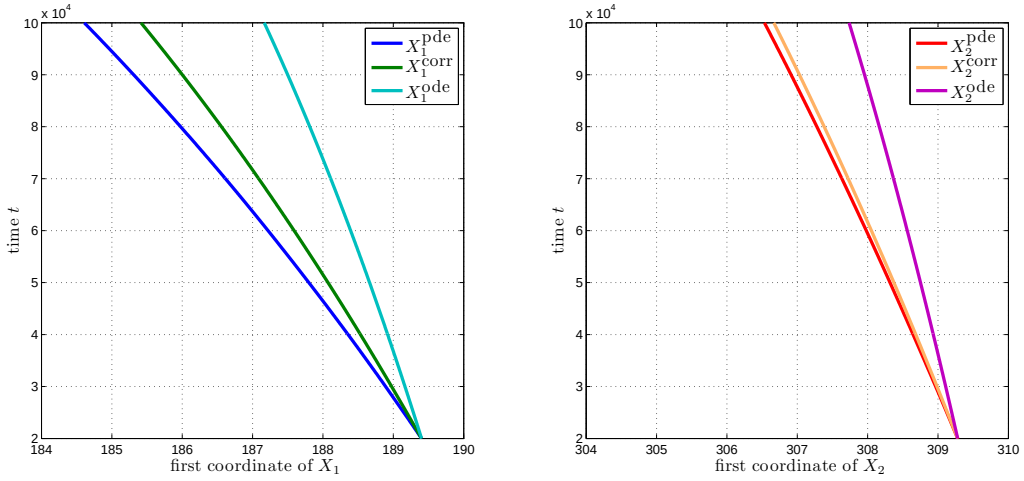

Figure 6.16: Comparison of the center evolution derived from the reduced dynamics (X_i^{ode}), the reduced dynamics with corrected flux (X_i^{corr}) based on (6.11), and the PDE (X_i^{pde}).

	$L = 120$	$L = 150$	$L = 180$	$L = 210$	$L = 240$
$\lvert J_1^{\text{corr}}/J_1\rvert$	1.474	1.711	1.971	2.256	2.559

Table 6.2: Relative improvement of the flux $J_1 = \dot{V}_2 \nabla \psi_{V_2}(X_1)$.

values of L but fixed radii $R_1(0) = 30$ and $R_2(0) = 45$. The speed-up factor increases for larger L, since the nearer the droplets are to the boundary, the larger is the deviation of $\nabla \psi_{V_i} \cdot \nu$ from zero at the boundary. We finally note that the above correction factor does not depend on the mobility coefficient, as we only improve the accuracy of the ambient flux field. The dependence on q emanates from the migration factor.

Correction of the ambient flux field (Part II: Volume sources in a bounded domain)

We can further refine the improvement of the ambient flux field defined by (6.11) as we consider the following problem for the correction of J_1: Let Ψ_2 be a solution of

$$-\Delta \Psi_2 = 0 \quad \text{in } \Omega \backslash B_2, \tag{6.12a}$$

$$\Psi_2 = \frac{\dot{V}_1}{2\pi} \log|x - X_1| - \frac{2\sqrt{2}}{R_2} \text{ on } \partial B_2, \qquad \nabla \Psi_2 \cdot \nu = \frac{\dot{V}_1}{2\pi} \frac{x - X_1}{|x - X_1|^2} \cdot \nu \text{ on } \partial\Omega. \tag{6.12b}$$

Note that the solution Ψ_2 is constructed such that

$$\Psi_2^{\text{corr}} := \frac{\dot{V}_1}{2\pi} \log|x - X_1| - \Psi_2$$

solves $-\Delta\Psi_2^{\text{corr}} = -\dot{V}_1\delta_{X_1}$ in $\Omega\backslash B_2$, $\Psi_2^{\text{corr}} \equiv \frac{2\sqrt{2}}{R_2}$ on ∂B_2, and $\nabla\Psi_2^{\text{corr}} \cdot \nu = 0$ on $\partial\Omega$. Then we define the corrected flux by

$$\widetilde{J}_1^{\text{corr}} := \nabla\Psi_2(X_1).$$

The correction problem for J_2, which yields the flux $\widetilde{J}_2^{\text{corr}}$, is defined analogously. Problem (6.12) is in a sense closer to reality compared to the correction function in the preceding part, because we consider the droplet (that generates the flux field) not as a point source any more. The gradient is expected to be slightly steeper due to the "thickened" droplet, which leads to a speed-up of the droplets. Figure 6.17 shows the improved results for the evolution of the centers.

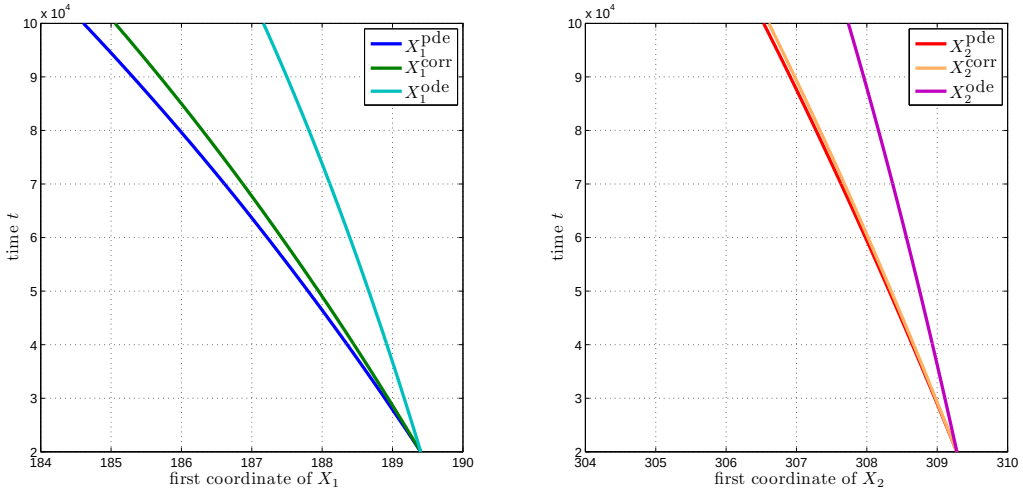

Figure 6.17: Comparison of the center evolution derived from the reduced dynamics (X_i^{ode}), the reduced dynamics with corrected flux (X_i^{corr}) based on (6.12), and the PDE (X_i^{pde}).

Finally, Table 6.3 provides a quantitative overview of the relative improvement compared to $J_1 = \dot{V}_2\nabla\psi_{V_2}(X_1)$. In comparison with Table 6.2, we gain another 3–15% in accuracy, so that in conclusion, we will rely on the auxiliary problem (6.12) instead of (6.11) in the following. Of course, the impact of this refined approximation weakens as the distance

	$L = 120$	$L = 150$	$L = 180$	$L = 210$	$L = 240$
$\lvert\widetilde{J}_1^{\text{corr}}/J_1\rvert$	1.623	1.793	2.028	2.294	2.587

Table 6.3: Relative improvement of the flux J_1 achieved by further approximations based on (6.12).

between the droplets grows.

Summary

Let us now summarize all the improvements of the reduced Rayleigh dynamics presented above. Figure 6.18 displays the results of the overall improvement for the initial configu-

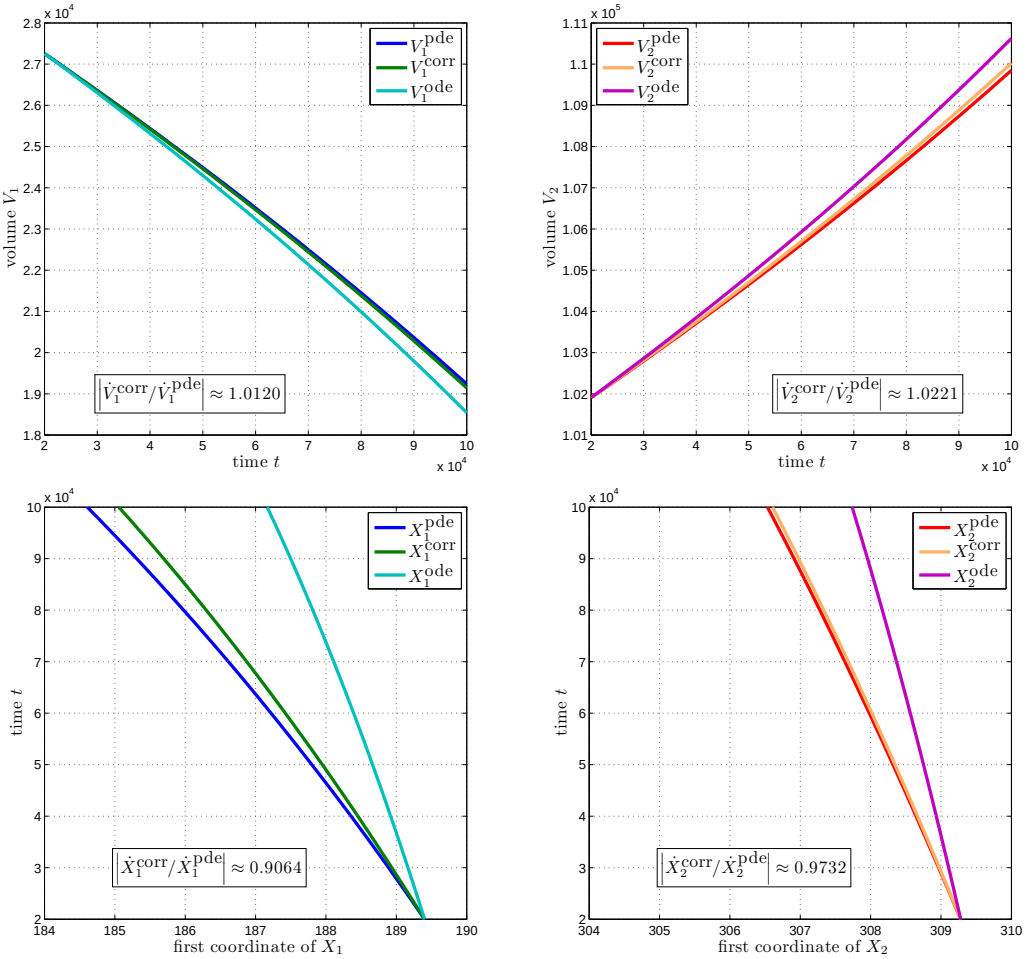

Figure 6.18: The dynamics derived from the intermediate approximations (denoted by the superscript "corr") yields much better results than the original reduced Rayleigh dynamics.

ration (6.9). The impact is huge especially for the droplet migration, where the accuracy measured by $|\dot{X}_i^{\mathrm{corr}}/\dot{X}_i^{\mathrm{pde}}|$ improves from approximately 50% for the reduced dynamics (see Figure 6.10) up to over 90%. The volume change is recovered independently of the droplet distance L as already investigated in Table 6.1. We find a deviation of 1.2–2.2% measured in terms of $|\dot{V}_i^{\mathrm{corr}}/\dot{V}_i^{\mathrm{pde}}|$.

To study the influence of the size of L/R on the accuracy of droplet migration, we additionally conduct numerical tests for increasing L but fixed radii. Since the approximation

of the matrix coefficients derived in Section 5.3.1 depends on the regime $L \gg R$, we expect an enhancement of the accuracy for increasing L. Indeed, the results presented in Figure 6.19 confirm this. In summary, the quality of approximation for $q = 2$ is very

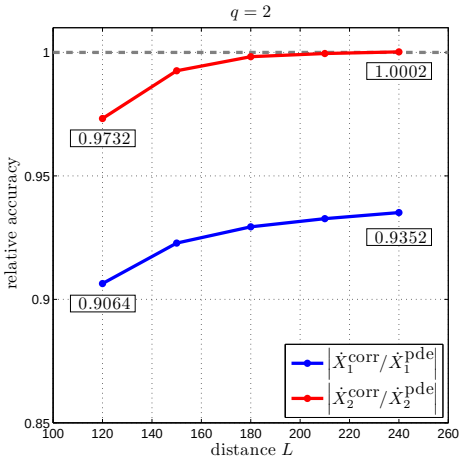

Figure 6.19: The relative accuracy (averaged over time) of the droplet velocities for varying distance L and the mobility exponent $q = 2$.

satisfactory as we achieve for $L = 240$ a deviation of less than 10%, namely $\approx 6.5\%$ for the smaller and $< 1\%$ for the larger droplet.

6.3.3 Collision vs. collapse

In the case of $q = 3$, we infer from the scaling relations (5.40) that the time scales for Ostwald ripening and migration are comparable (up to a logarithm) in the sense that the time scale for a droplet to move over a distance L is the same as the time scale to double its volume. These relations are based on the reduced system of ODEs (5.10) with coefficients derived by asymptotic analysis in the regime $1 \ll R \ll L$.

In the two-dimensional case, the fact that a droplet migrates over a distance L *does not* necessarily imply collision with another droplet, since droplets might miss each other in two dimensions (as opposed to the one-dimensional case) unless there is no "attractive" force between them. However, we argued in the introduction of this thesis that aimed migration of two small droplets towards each other generically occurs in the coarsening dynamics. To support our findings, let us conduct a numerical test. For this purpose, we consider two small droplets submerged into a configuration of relatively large droplets as shown in Figure 6.20 (left). The droplet at X_2 is slightly larger than the droplet at X_1. We learn from (5.37) that a droplet is attracted by another mass-loosing droplet. Both small droplets loose mass to the surrounding larger droplets, see Figure 6.20 (right). Consequently, both droplets move towards each other and eventually collide. Figure 6.21 shows the collision event (top), and for comparison, the dynamics of the same two droplets without a surrounding configuration of larger droplets (bottom).

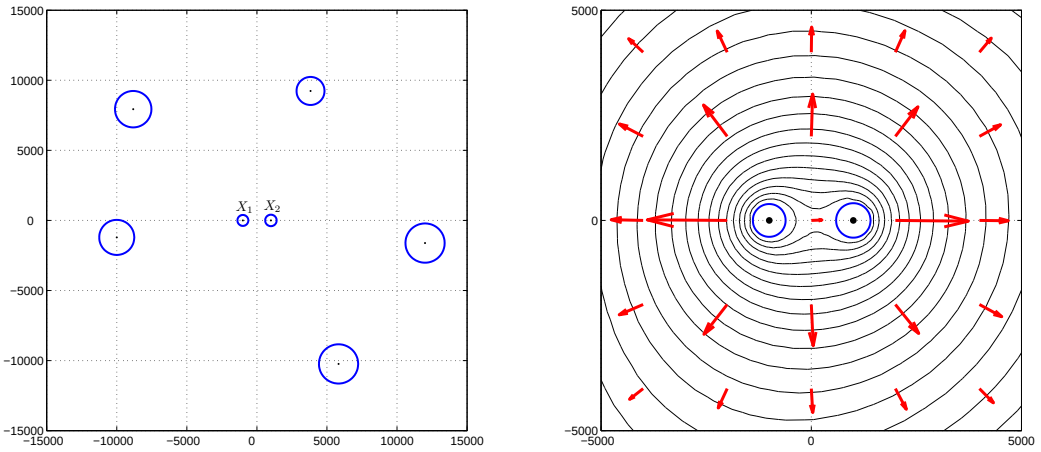

Figure 6.20: Two small droplets at X_1 and X_2 submerged into a configuration of larger droplets (left). The surrounding droplets generate a nearly homogeneous flux field, which transports mass from the two smaller droplets (right).

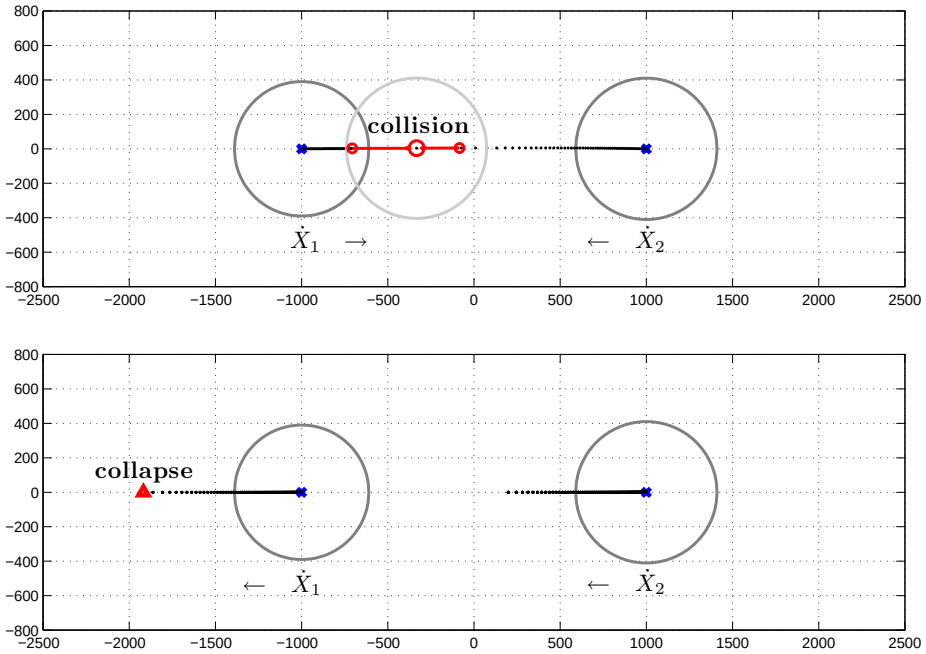

Figure 6.21: The two small droplets (submerged into a configuration of larger droplets) migrate towards each other and eventually collide (top) as opposed to the case of two isolated droplet (bottom), where both droplets move westwards in the direction of the smaller one.

Hence, in conclusion, we expect that collision can play a role for the two-dimensional coarsening process in the case $q = 3$. The impact strongly depends on the average film

height $\overline{H} \sim L^{-2}V$ according to the scaling (5.40). To give an idea of the influence of $\overline{H}$, we conduct numerical tests for an ensemble of 100 droplets based on the reduced Rayleigh dynamics (5.10). For a fixed average distance $L \approx 1000$, the typical radius varies between $R \approx 100$ and $R \approx 300$. Figure 6.22 shows the collision fraction of the coarsening process depending on $\overline{H}$. A similar, but more extensive parameter study was

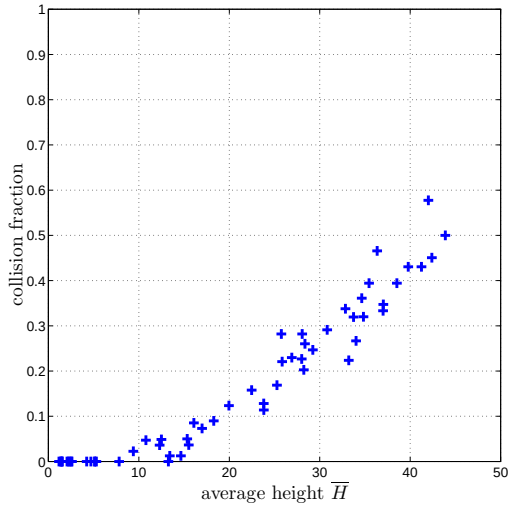

Figure 6.22: The fraction of collision events for the coarsening process. An equal number of both types of coarsening events is reached for $\overline{H} \approx 40$.

conducted by Glasner and Witelski for the one-dimensional problem [16].

A non-generic collision scenario

We conduct numerical tests solving the system (6.6) for a non-generic droplet configuration to give an idea how in detail migration can lead to droplet collisions and how it might influence the coarsening process – depending on the mobility exponent. As an initial configuration, we consider two rings of 8 droplets each and one center droplet, see Figure 6.23. The typical radius of the droplets in the outer ring is ≈ 400 but randomly perturbed in the range of 1%, in the inner ring ≈ 250 (again randomly perturbed); the center droplet has radius 200. The droplet distances vary between 1600 and 2000.

The subsequent figures show the trajectories of the centers over the total time $T = 10^{10}$ derived from the reduced dynamics for mobility exponents $q = 2$ and $q = 3$. Since we are only interested in qualitative behavior, we also conduct tests for $q = 3$, although the exact coefficients also depend on $\mathcal{U}$. We take exactly the same initial configuration for both exponents. Let us first give some explanations:

- The crosses are the initial centers of the droplets. The grey circles indicates the initial size.

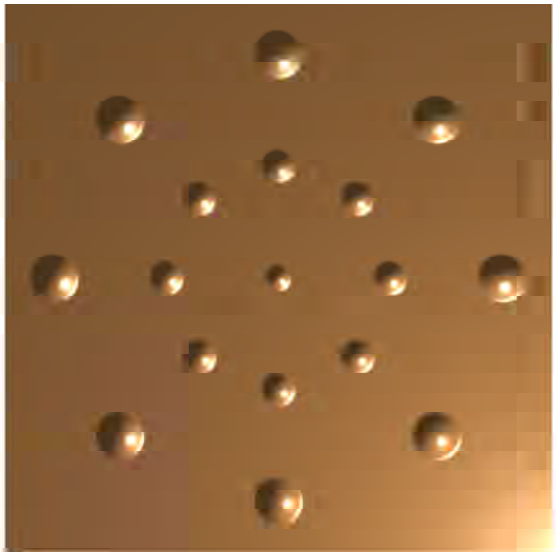

Figure 6.23: Initial configuration of the numerical simulation of the reduced ODE system.

- When a droplet vanishes, its last position is given by a triangle.
- In case of a droplet collision, the centers of the two involved droplets marked by circles are merged along the line to a new one (also depicted by a circle) according to the merging rule (6.8).

First, let us consider the case $q = 3$ in Figure 6.24 and 6.25:

- Since the average radius of a droplet in the outer ring is much larger than in the inner ring, all droplets migrate towards the center droplet positioned at the origin. The center droplet vanishes first.
- Every change in the number of droplets affects the movement of the remaining droplets immediately; the trajectories are non-smooth. So each singularity of a trajectory can be related to a disappearance of a droplet.
- In Figure 6.25 one can inspect two collision events along the red lines. The asymmetric coalescence is due to the different droplet sizes, since the new center is symmetric w.r.t. the outer contact lines of the two collided droplets.
- The varying resolution of the trajectories reveals that the migration speed of each droplet varies: The closer the droplets are, the faster they both move.
- Eventually, all droplets in the inner ring vanish (including the newly merged ones), only the outer ring of larger droplets survives.
- The total balance of the evolution is: 2 collisions and 7 collapses.

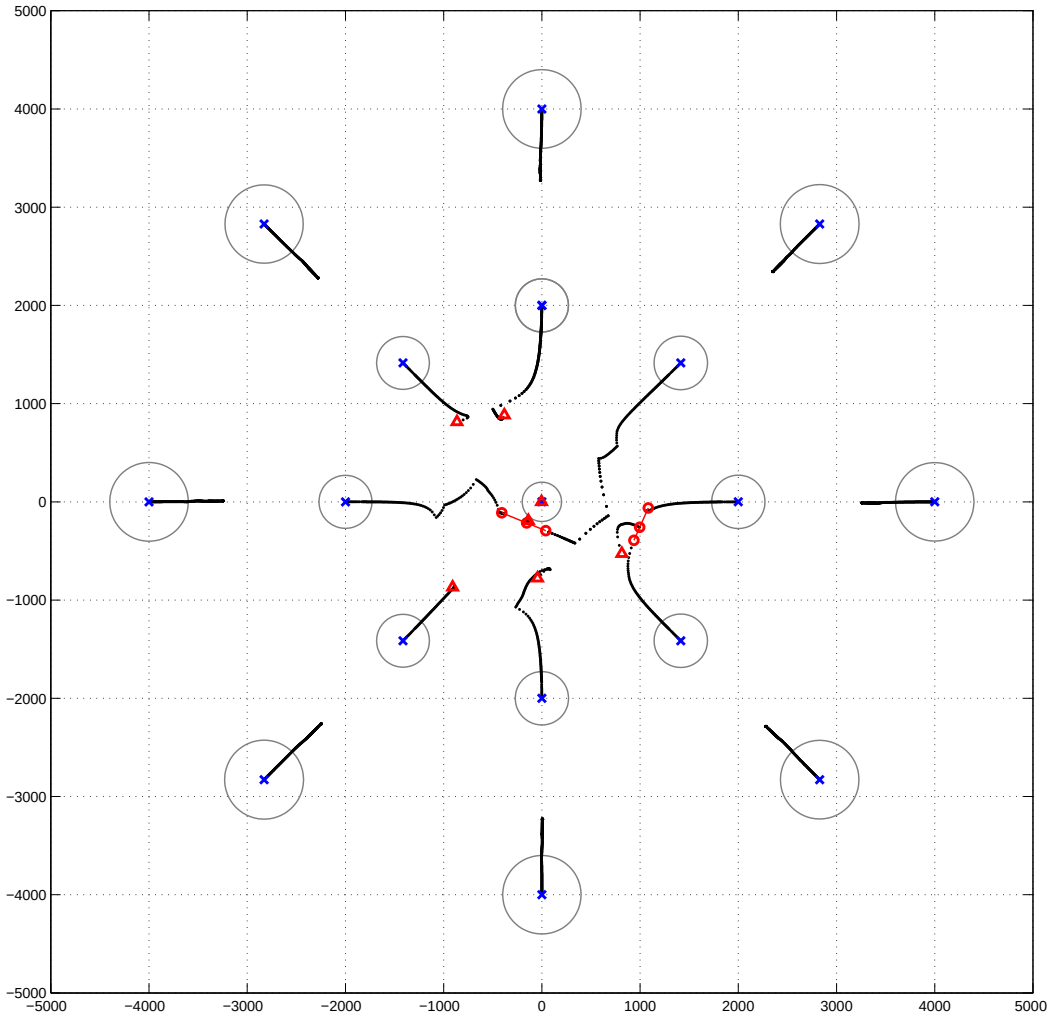

Figure 6.24: Trajectories of the droplet centers $\{X_i(t)\}$ in the case of high mobility $q = 3$, see Figure (6.25) for a zoom into the inner ring.

In the case of $q = 2$ (see Figure 6.26) collisions do not occur; the dominating coarsening process is Ostwald ripening. Furthermore, the droplets migrate much slower as can be seen from the lengths of the trajectories.

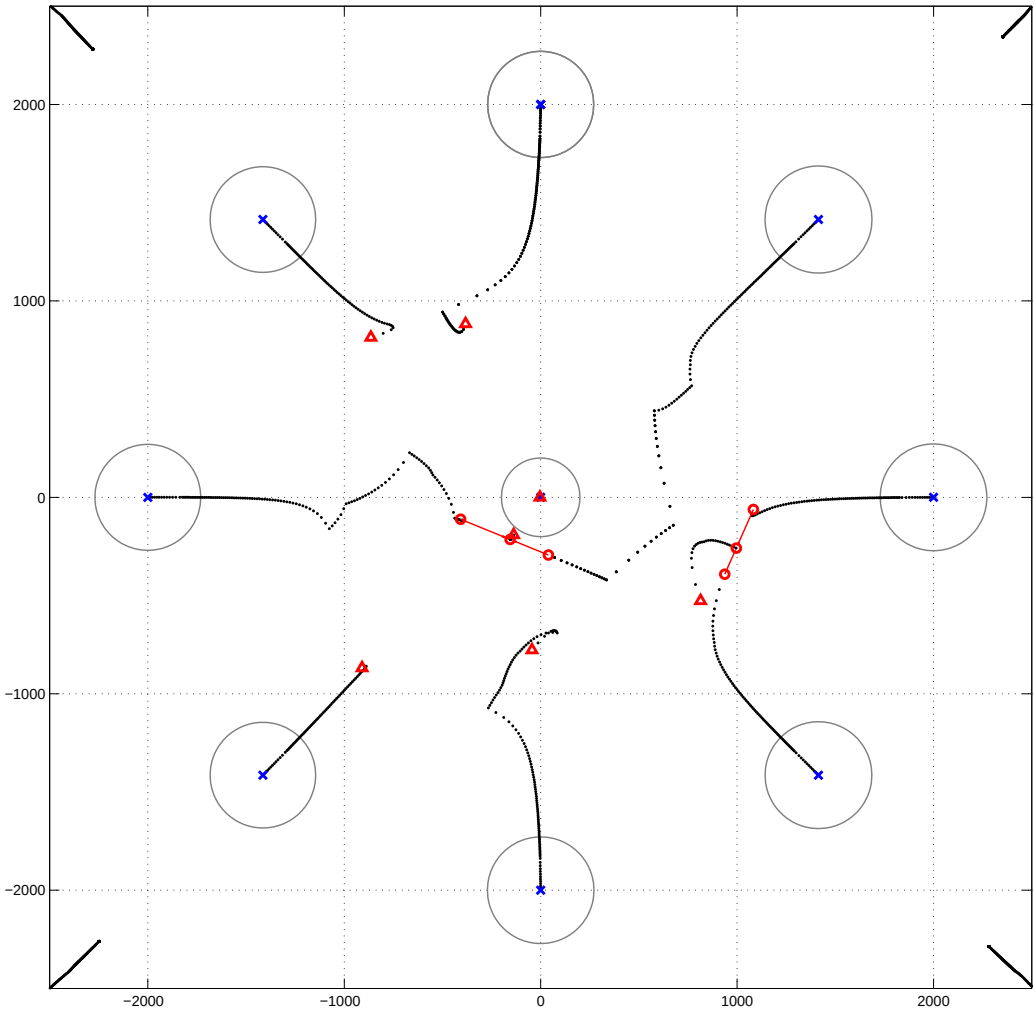

Figure 6.25: A closer look at droplet collisions in the case $q = 3$.

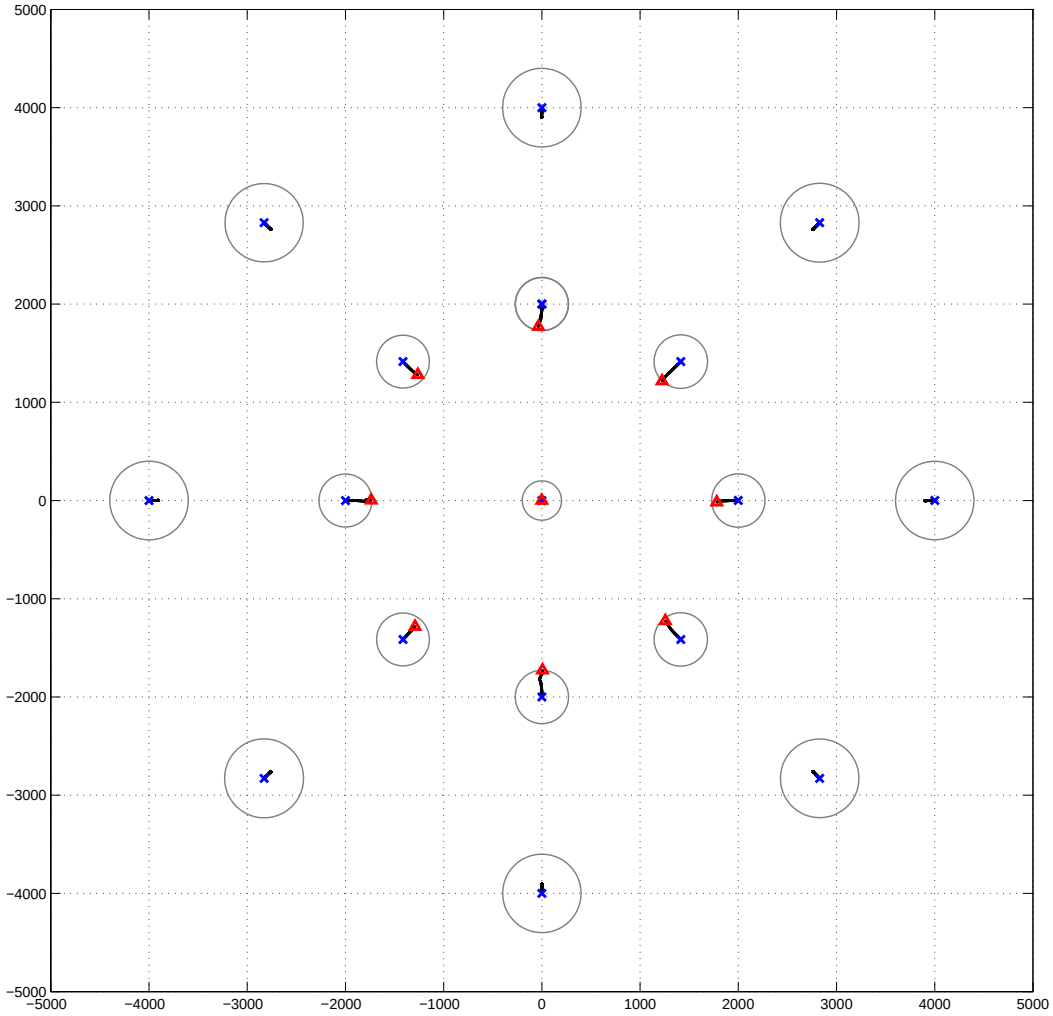

Figure 6.26: Trajectories of the droplet centers $\{X_i(t)\}$ in the case $q = 2$.

List of symbols

α	geometric exponent that characterizes the energy landscape, page 32.
$B_R(X)$	d-dimensional ball with center $X \in \mathbb{R}^d$ and radius $R > 0$, page 26.
C	submatrix of G that encodes the coupling between volume change and migration, page 91.
c_i, c_{ij}	dissipative integral coefficient relevant to coupling, page 92.
D	dissipation by viscous friction, page 17.
d	spatial dimension, page 1.
$\delta h_{\dot{\Theta}}$	infinitesimal change of the height profile of the configuration Θ corresponding to the change vector $\dot{\Theta}$, page 89.
$\triangle x$	grid size of a spatial discretization, page 107.
$\frac{\delta E}{\delta h}$	L^2-gradient of the energy functional E, page 2.
$\mathrm{diff} E_x.v$	differential of $E : \mathcal{M} \to \mathbb{R}$ in $x \in \mathcal{M}$ in direction of $v \in T_x\mathcal{M}$, page 30.
$d(x, y)$	distance between x and y on Riemannian manifold induced by the metric tensor g, page 30.
E	energy of the liquid film, page 1.
$\overline{E}$	mesoscopic energy, page 26.
ψ_V	pressure that transports mass 1 out of a single mesoscopic droplet of volume V, page 54.
$\bar{\psi}$	pressure that generates volume change 1 between two mesoscopic droplets, page 53.
G	symmetric matrix representing the bilinear form D in the case of a reduced finite-dimensional configuration space, page 91.
γ	dynamical exponent that characterizes the energy decay in time, page 29.
g_i	dissipative integral coefficient relevant to droplet migration, page 92.
G^m	submatrix of G subject to migration, page 91.

G^v	submatrix of G subject to volume change, page 91.
g_x	metric tensor in $x \in \mathcal{M}$, page 30.
H	height of an equilibrium (or mesoscopic) droplet, page 26.
h	height of thin liquid film evolving according to the thin-film equation, page 1.
$\widetilde{h}$	equilibrium droplet profile of constant pressure P, page 19.
h^k	numerical solution of the time-discretized thin-film equation at time t_k, page 105.
$h_{V,X}$	mesoscopic droplet profile parametrized by its volume V and center X, page 27.
h_i	mesoscopic droplet profile h_{V_i,X_i} with volume V_i and center X_i, page 51.
$\mathbb{I}\mathrm{d}$	identity map, page 14.
$\mathcal{I}_{\psi_0}$	numerator of the 2-d migration factor (depending on ψ_0), page 66.
$\mathcal{I}_{\psi_1}$	denominator of the 2-d migration factor (depending on ψ_1), page 66.
J	flux in thin liquid film generated by the pressure gradient, page 1.
J_∞	constant ambient flux field that generates migration, page 57.
J^k	numerical solution of the flux J at time t_k, page 105.
Λ	system size for the special choice $\Omega := [0, \Lambda]^d$, page 13.
L, L_{ij}	distance between two droplets (labeled with i and j), page 48.
$\mathcal{M}$	Riemannian manifold, page 30.
m_i	mobility function w.r.t. a single mesoscopic droplet profile h_i, page 89.
m	mobility function h^q, page 3.
N	number of droplets, page 50.
Ω	domain $\subset \mathbb{R}^d$, page 1.
ω	dimension-depending relation factor between the radius R and the volume V of a mesoscopic droplet, page 27.
ω_d	volume of the d-dimensional unit ball, page 26.
P	pressure of an equilibrium (or mesoscopic) droplet, page 19.
p	normal vector of affine space of all volume-preserving configuration changes $\dot{\Theta}$, page 89.

$\varphi_{\dot\Theta}$ pressure generated by configuration change $\dot\Theta$, page 90.

Π projection ($\mathbb{I}\mathrm{d} - pp^T$) to the orthogonal complement of p, page 91.

ψ_0 pressure of an equilibrium droplet that stems from a normalized flux boundary condition, page 61.

ψ_1 pressure of an equilibrium droplet that makes the droplet move with unit speed $(1,0)^T$, page 61.

$\psi_1^{\dot X}$ pressure of an equilibrium droplet, which makes the droplet move with speed $\dot X \in \mathbb{R}^2$, page 90.

q non-negative exponent of mobility function $m(h) = h^q$, page 3.

R radius of an equilibrium (or mesoscopic) droplet, page 22.

$\mathcal{R}$ Rayleigh functional, page 16.

τ, τ_k (uniform) step size $t_{k+1} - t_k$ for a finite partition $\{t_k\}$ of $[0,T]$, page 105.

τ_{mig} typical time scale for migration of interacting droplets, page 103.

τ_{rip} typical time scale for Ostwald ripening of interacting droplets, page 103.

Θ configuration vector $\in \mathbb{R}^{(d+1)N}$ representing an ensemble of N mesoscopic droplets, page 88.

$\dot\Theta$ infinitesimal change of a mesoscopic droplet configuration defined by Θ, page 89.

$T_x\mathcal{M}$ tangent space in $x \in \mathcal{M}$, page 30.

$\mathcal{U}$ intermolecular potential, page 2.

$\mathcal{W}$ quadratic Wasserstein distance, page 37.

X center of symmetry of an equilibrium (or mesoscopic) droplet, page 57.

$\dot X$ infinitesimal change of the center X of a droplet, page 57.

Order symbols

Let f and g be two functions depending on x. We define the Landau symbols:

- $f = \mathcal{O}(g)$ as $x \to x_0$, if the limit $\lim_{x \to x_0} \frac{f(x)}{g(x)}$ exists and is finite.
- $f = o(g)$ as $x \to x_0$, if $\lim_{x \to x_0} \frac{f(x)}{g(x)} = 0$.

Note that we will usually speak of "in the regime $x \gg 1$" or "for large x" instead of using the phrase "as $x \to \infty$".

Based on the above we will frequently use the following notation in the context of asymptotic analysis:

- "f is equal to g to leading order in x", or

  $$f \approx g, \quad \text{as } x \to x_0,$$

  if $f = g + o(g)$ as $x \to x_0$. The symbols $\gtrapprox$ and $\lessapprox$ are defined analogously.
- "f scales like g to leading order in x", or

  $$f \sim g, \quad \text{as } x \to x_0,$$

  if $f \approx C\, g$ for some constant C independent of x. The symbols $\gtrsim$ and $\lesssim$ are defined analogously.
- "f is of lower order in x than g", or

  $$f \ll g, \quad \text{as } x \to x_0,$$

  if $f = o(g)$ as $x \to x_0$.

Bibliography

[1] N. D. Alikakos and G. Fusco. Ostwald ripening for dilute systems under quasistationary dynamics. *Comm. Math. Phys.*, 238(3):429–479, 2003.

[2] N. D. Alikakos, G. Fusco, and G. Karali. The effect of the geometry of the particle distribution in Ostwald ripening. *Comm. Math. Phys.*, 238(3):481–488, 2003.

[3] S. Balay, K. Buschelman, W. D. Gropp, D. Kaushik, M. G. Knepley, L. Curfman McInnes, B. F. Smith, and H. Zhang. PETSc Web page, 2001. http://www.mcs.anl.gov/petsc.

[4] A. L. Bertozzi, G. Grün, and T. P. Witelski. Dewetting films: bifurcations and concentrations. *Nonlinearity*, 14(6):1569–1592, 2001.

[5] S. Conti, B. Niethammer, and F. Otto. Coarsening rates in off-critical mixtures. *SIAM J. Math. Anal.*, 37(6):1732–1741 (electronic), 2006.

[6] S. Dai and R. L. Pego. Universal bounds on coarsening rates for mean-field models of phase transitions. *SIAM J. Math. Anal.*, 37(2):347–371 (electronic), 2005.

[7] S. Dai and R. L. Pego. An upper bound on the coarsening rate for mushy zones in a phase-field model. *Interfaces Free Bound.*, 7(2):187–197, 2005.

[8] P. G. de Gennes. Wetting: statics and dynamics. *Rev. Mod. Phys.*, 57(3):827–863, Jul 1985.

[9] P.-G. de Gennes, F. Brochard-Wyart, and D. Quéré. *Capillarity and wetting phenomena*. Springer-Verlag, New York, 2004.

[10] J. Dohmen, N. Grunewald, F. Otto, and M. Rumpf. Micro structures in thin coating layers: Micro structure evolution and macroscopic contact angle. 2008.

[11] T. Erneux and D. Gallez. Can repulsive forces lead to stable patterns in thin liquid films? *Physics of Fluids*, 9(4):1194–1196, 1997.

[12] S. Esedoglu and J. Greer. Upper bounds on the coarsening rate of discrete, ill-posed nonlinear diffusion equations. accepted for publication in Comm. Pure Appl. Math., 2007.

[13] M. Frigo and S. G. Johnson. The design and implementation of FFTW3. *Proceedings of the IEEE*, 93(2):216–231, 2005.

[14] K. B. Glasner. Spreading of droplets under the influence of intermolecular forces. *Physics of Fluids*, 15(7):1837–1842, 2003.

[15] K. B. Glasner and T. P. Witelski. Coarsening dynamics of dewetting films. *Phys. Rev. E*, 67(1):016302, 2003.

[16] K. B. Glasner and T. P. Witelski. Collision versus collapse of droplets in coarsening of dewetting thin films. *Phys. D*, 209(1-4):80–104, 2005.

[17] H. P. Greenspan. On the motion of a small viscous droplet that wets a surface. *J. Fluid Mech.*, 84(1):125–143, 1978.

[18] G. Grün and M. Rumpf. Nonnegativity preserving convergent schemes for the thin film equation. *Numer. Math.*, 87(1):113–152, 2000.

[19] R. V. Kohn and F. Otto. Upper bounds on coarsening rates. *Comm. Math. Phys.*, 229(3):375–395, 2002.

[20] R. V. Kohn and X. Yan. Upper bound on the coarsening rate for an epitaxial growth model. *Comm. Pure Appl. Math.*, 56(11):1549–1564, 2003.

[21] R. V. Kohn and X. Yan. Coarsening rates for models of multicomponent phase separation. *Interfaces Free Bound.*, 6(1):135–149, 2004.

[22] L. D. Landau and E. M. Lifshitz. *Course of theoretical physics. Vol. 6.* Pergamon Press, Oxford, second edition, 1987. Fluid mechanics, Translated from the third Russian edition by J. B. Sykes and W. H. Reid.

[23] E. H. Lieb and M. Loss. *Analysis*, volume 14 of *Graduate Studies in Mathematics*. American Mathematical Society, Providence, RI, second edition, 2001.

[24] R. Limary and P. F. Green. Late-stage coarsening of an unstable structured liquid film. *Phys. Rev. E*, 66(2):021601, 2002.

[25] R. Limary and P. F. Green. Dynamics of droplets on the surface of a structured fluid film: Late-stage coarsening. *Langmuir*, 19(6):2419–2424, 2003.

[26] L. Onsager. Reciprocal relations in irreversible processes. i. *Phys. Rev.*, 37(4):405–426, Feb 1931.

[27] F. Otto, P. Penzler, and T. Rump. Discretisation and numerical tests of a diffuse–interface model with Ehrlich–Schwoebel barrier. In *Multiscale Modeling in Epitaxial Growth*, volume 149 of *International Series of Numerical Mathematics*, pages 127–158. Birkhaeuser, 2005.

[28] F. Otto, T. Rump, and D. Slepčev. Coarsening rates for a droplet model: Rigorous upper bounds. *SIAM J.Math.Anal.*, 32(2):503–529, 2006.

[29] F. Otto, T. Rump, and D. Slepčev. Ostwald ripening of droplets: The role of migration. SFB Preprint no. 339, accepted for publication in Europ. J. Appl. Math., 2007.

[30] F. Otto and C. Villani. Generalization of an inequality by Talagrand and links with the logarithmic Sobolev inequality. *J. Funct. Anal.*, 173(2):361–400, 2000.

[31] F. Otto and M. Westdickenberg. Eulerian calculus for the contraction in the Wasserstein distance. *SIAM J. Math. Anal.*, 37(4):1227–1255 (electronic), 2005.

[32] P. Penzler. PhD thesis, Institute of Applied Mathematics, University of Bonn, 2008. in preparation.

[33] L. M. Pismen and Y. Pomeau. Mobility and interactions of weakly nonwetting droplets. *Phys. Fluids*, 16(7):2604–2612, 2004.

[34] W. H. Press, S. A. Teukolsky, W. T. Vetterling, and B. P. Flannery. *Numerical recipes in C++*. Cambridge University Press, Cambridge, 2002. The art of scientific computing, Second edition, updated for C++.

[35] M. H. Protter and H. F. Weinberger. *Maximum principles in differential equations*. Prentice-Hall Inc., Englewood Cliffs, N.J., 1967.

[36] O. Reynolds. On the theory of lubrication and its application to Mr. Beauchamp Tower's experiment, including an experimental determination of the viscosity of olive oil. *Philos. Trans. R. Soc. London*, 177:157–234, 1886.

[37] C. Villani. *Topics in optimal transportation*, volume 58 of *Graduate Studies in Mathematics*. American Mathematical Society, Providence, RI, 2003.

[38] S. J. Watson and S. A. Norris. Scaling theory and morphometrics for a coarsening multiscale surface, via a principle of maximal dissipation. *Physical Review Letters*, 96(17):176103, 2006.

[39] Wolfram Research Inc. *Mathematica Edition: Version 6.0*. Wolfram Research Inc., Champaign, Illinois, 2007.